Influence of brass interlayer and cooling media on friction stir welded AA6061 alloy

A thesis submitted in the partial fulfilment of the requirement

for the award of the degree of

DOCTOR OF PHILOSOPHY

by

KORRA NAGU

Roll No: 717021

Under the Supervision of

Dr. ADEPU KUMAR

Professor, MED

Department of Mechanical Engineering

DEPARTMENT OF MECHANICAL ENGINEERING

NATIONAL INSTITUTE OF TECHNOLOGY

WARANGAL-506004, TELANGANA, INDIA.

AUGUST 2022

THESIS APPROVAL FOR Ph.D.

This thesis entitled **"Influence of brass interlayer and cooling media on friction stir welded AA6061 alloy"** by **Mr. Korra Nagu** is approved for the degree of Doctor of Philosophy.

_____

_____

_____

Examiner

Dr. Adepu Kumar
Professor, Department of Mechanical Engineering, NIT Warangal
Supervisor

Dr. V. Suresh Babu
Professor, Department of Mechanical Engineering, NIT Warangal
Chairman

Dr. Adepu Kumar
Head, Department of Mechanical Engineering, NIT Warangal

NATIONAL INSTITUTE OF TECHNOLOGY

WARANGAL – 506 004, Telangana State, INDIA

CERTIFICATE

This is to certify that the work presented in the thesis entitled **"Influence of brass interlayer and cooling media on friction stir welded AA6061 alloy"** which is being submitted by **Mr. Korra Nagu (Roll No. 717021)**, is a bonafide work submitted to National Institute of Technology, Warangal in partial fulfillment of the requirement for the award of the degree of **Doctor of Philosophy in Mechanical Engineering**. To the best of our knowledge, the work incorporated in the thesis has not been submitted to any other university or institute for the award of any degree or diploma.

Dr. V. Suresh Babu
Chairman –DSC
Professor
Department of Mechanical Engineering
National Institute of Technology
Warangal-506 004, Telangana, India

Dr. Adepu Kumar
Thesis supervisor
Professor and Head
Department of Mechanical Engineering
National Institute of Technology
Warangal-506 004, Telangana, India

NATIONAL INSTITUTE OF TECHNOLOGY

WARANGAL – 506 004, Telangana State, INDIA

DECLARATION

This is to certify that the work presented in the thesis entitled **"Influence of brass interlayer and cooling media on friction stir welded AA6061 alloy"**, is a bonafide work done by me under the supervision of **Dr. Adepu Kumar,** Professor, Department of Mechanical Engineering, NIT Warangal, India and has not been submitted for the award of any degree to any other University or Institute.

I declare that this written submission represents my idea in my own words and where other's ideas or words have not been included. I have adequately cited and referenced the original sources. I also declare that I have adhered to all principles of academic honesty and integrity and have not misinterpreted or fabricated or falsified any idea/data/fact/source in my submission. I understand that any violation of the above will be a cause for disciplinary action by the Institute and can also evoke penal action from the sources which have thus not been properly cited or from whom proper permission has not been taken when needed.

Date:

Place: Warangal

Mr. Korra Nagu

Research Scholar

Roll No. 717021

ACKNOWLEDGEMENT

Firstly, I would like to express my sincere gratitude and thanks to my advisor **Prof. Adepu Kumar**, Department of Mechanical Engineering, National Institute of Technology, Warangal for the continuous support of my Ph.D. study, for his patience and motivation. His guidance, support and encouragement helped me in all the time of research and writing of this thesis.

Besides my advisor, I would like to thank the Doctoral scrutiny committee (DSC) members **Prof. Adepu Kumar** (Head, Dept. of Mechanical Engineering), **Prof. V. Suresh Babu** (DSC chairman), **Prof. K.V. Sai Srinadh** (Dept. of Mechanical Engineering), **Asst**. **Prof. G. Raghavendra** (Dept. of Mechanical Engineering), **Prof**. **Asit Kumar Khanra** (Dept. of Metallurgical and Materials Engineering), for their valuable suggestions and comments at each and every stage during my Ph.D. progress.

I would like to thank Dr. shivraman (Dept. of Mechanical Engineering, NIT-Warangal) and Dr. Raja vishwanatham (Department of Humanities & Social Science, NIT-Warangal) for their support. The authors heartily thank the Dr. CH. Raj Mohan (Department of Chemical Engineering, NIT-Warangal, India for providing with research facilities to carry out the electrochemical study. The authors are grateful to Dr. I. Samajdar, Professor (Department of Metallurgical & Materials Science, IIT Bombay) for providing with an OIM and Texture facility. The authors heartily thank Dr. R. Arockia Kumar, Assistant professor (Dept. of Metallurgical and Materials Engineering), for providing damping test facility.

My heartful thanks to my beloved parents, my elder brother Korra Srinivas and family members Lunavath Sharada, Lunavath Kavitha and Korra Upender Nayak for their encouragement, constant support, and motivation. Their role is immeasurable, without which it would have been impossible for me to complete this project work and thesis.

My sincere thanks also goes to my seniors and well-wishers Dr. Kethavath Kranthi Kumar, Dr. MVNV Satyanarayana, Dr. M. Krishna Kishore, Dr. B. Venkatesh, Dr. P. Naresh and Dr. Rajendra Prasad for their valuable suggestions and encouragement. I would be very delighted and happy to express my sincere thanks to my Labmates I Karthikeya sharma and Sarvana Sundar and my friends Dr. K. Benarji, and A. Ramana Reddy for their sharing, caring

and co-operation during my entire Ph.D stay.

Last but not least, I would like to thank the non-teaching staff Mr. Yellaswamy, workshop technicians and many other at NIT Warangal for their help in many occasions during my experimental work.

- Korra Nagu

Dedicated To

My beloved parents

Sri Korra Dasru

Smt Korra Salli

and

Brother Korra Srinivas

ABSTRACT

Lightweight aluminium alloys have been employed in industries and aerospace applications due to their high strength-to-weight ratio. The heat-treatable AA6061-T6 is a low-strength aluminium alloy among all Al series alloys consisting of Mg and Si as major alloying elements. The major concerns in fusion welding of aluminium alloys are melting of base metal, porosity and solidification cracking that occurs due to temperature attained above the melting point of base metal. The solution to overcome the defects obtained with fusion welding is to weld the base metal below its melting point, which can be obtained using a solid-state joining process. Friction stir welding (FSW) is a solid-state joining process used to join aluminium alloys. Even though fine and recrystallized grains were obtained using FSW, the softening at the stir zone (SZ) caused due to weld thermal cycle results in decreased weld joint strength and deterioration of corrosion resistance. One approach to minimize thermal softening during FSW and enhance the joint strength is inserting a suitable interlayer between weld plates.

In this study, FSW was performed on AA6061-T6 with and without brass interlayer. In the first phase, FSW process parameters were selected to ensure defect-free joint and enhanced weld strength with interlayer. The FSW was performed with interlayer for various tool rotational speeds (600-1000 rpm) and at constant travel speed (25 mm/min). The defect-free joint with uniform distribution of brass particles in the SZ and the uniform composite structure formed was observed at an intermediate optimized tool rotational speed of 800 rpm due to the proper material flow. A strong metallurgical bond formed between brass particles with aluminium alloy resulted in the formation of Al_2Cu and Al_4Cu_9 strengthening intermetallic compounds (IMCs). The average grain size obtained for the weld with interlayer is smaller than weld without interlayer. The presence of interlayer enhanced the hardness and tensile strength compared to weld without interlayer. This improvement in mechanical properties with interlayer is attributed to the formation and uniform distribution of strengthening IMCs. The corrosion analysis was carried out in 3.5% NaCl solution using immersion and electrochemical polarization tests. The weld with interlayer showed enhanced corrosion resistance than without interlayer, which is attributed to the formation of significant Al_2Cu IMC, which has less activation energy for the corrosion process.

Even though, the strength was improved with interlayer, the strength recovery is not attainable in a heat-affected zone (HAZ). Moreover, hard and brittle IMCs formed in SZ of weld with interlayer resulted in premature failure. In the second phase, water cooling was employed during FSW with and without interlayer to enhance the hardness in HAZ, which can improve overall joint strength. Very fine grains in SZ with a high fraction of high angle grain boundaries (HABs) were obtained with water cooling FSW with interlayer, while HAZ softening was also reduced. Moreover, the water-cooling FSW with interlayer inhibited the formation of brittle intermetallics and decreased the volume fraction of IMCs, attributed to a faster cooling rate. Thereby the strength of the overall weld joint was enhanced. The corrosion findings stated that the decrease in the number of intermetallics formed low galvanic coupling with aluminium matrix resulted in better corrosion resistance and minimum corrosion rate for water-cooled FSW than natural cooling.

In the third phase, the wear and damping behaviour of base metal (BM) weld joints with and without interlayer under natural and water-cooling were performed. The damping results revealed that weld samples showed better damping capacity than BM, attributed to the grain refinement. Moreover, the damping capacity of weld with the addition of interlayer is enhanced due to more grain refinement, formation of hard intermetallics, and high inherent damping capacity of brass. The reduced intermetallics and formation of smooth interface obtained for water-cooled weld attributed to the faster cooling rate improved the mobility of grain boundaries which enhanced the damping capacity than natural cooling. Due to the increased grain boundary area, the water-cooled weld with interlayer showed better damping at high temperatures than other weld joints. The wear test results revealed that the wear rate of weld samples is higher than BM. The mean coefficient of friction (COF) of the weld without interlayer is the highest, and those of the weld with interlayer is the lowest, which can be due to the lubricant action of reinforcement particles. Moreover, the low wear rate values of weld with interlayer are attributed to grain refinement, formation of IMCs and the corresponding induced surface hardening. The water-cooled weld with interlayer showed a very low wear rate than the remaining welds due to the high hardness. By comparing 30 N and 50 N, the wear rate in 50 N is higher owing to higher friction resistance which causes an increase in temperature and decrease in hardness and wear resistance.

In the final phase of the work, fatigue behaviour of BM, welds with and without interlayer under natural and water-cooling was studied. The results revealed that weld samples sustained a longer fatigue life than BM, which was attributed to the grain refinement mechanism. The weld with interlayer showed better fatigue life than without interlayer due to fine-grained structure, a high fraction of grain boundaries, and formation of strong IMCs etc., act as obstacles for fatigue cracks propagation and stop the crack from further expanding. At the initial stages of crack propagation, the crack growth rate of BM is faster than weld samples at the same ΔK value, and da/dN of weld with interlayer is minimum. Reduction in brittle IMCs formation for water-cooled weld with interlayer resulted in a strong bond between brass and Al which caused more obstacles for fatigue cracks propagation and stopped the crack from further expanding, thereby enhancing the fatigue life.

Finally, the present study identified the significance of interlayer on microstructure, mechanical properties and corrosion behaviour of FSWed AA6061 alloy. Moreover, water cooling and interlayer combined effect enhanced joint efficiency and corrosion resistance. The high wear resistance, damping capacity, and fatigue life are obtained for water-cooled weld with interlayer.

TABLE OF CONTENTS

LIST OF FIGURES

LIST OF TABLES

LIST OF ABBREVIATIONS

FSW	Friction stir welding
TWI	The Welding Institute
SZ	Stir zone
HAZ	Heat affected zone
TMAZ	Thermo-mechanically affected zone
AS	Advancing side
RS	Retreating side
WNZ	Weld nugget zone
BM	Base metal
NCFSW	Natural Cooling FSW
WCFSW	Water Cooling FSW
OM	Optical microscope
SEM	Scanning electron microscope
EDS	Energy dispersion spectroscopy
XRD	X-ray diffraction
EBSD	Electron backscattered diffraction
GS	Grain size
PF	Pole figure
DRX	Dynamic recrystallization
DRZ	Dynamic recrystallized zone
CDRX	Continuous dynamic recrystallization
DRV	Dynamic recovery
SPD	Severe plastic deformation
LABs	Low angle boundaries
HABs	High angle boundaries
IPF	Inverse pole figure
UTM	Universal testing machine
UTS	Ultimate tensile strength
YS	Yield strength

EL	Elongation
NTS	Notch tensile strength
FCG	Fatigue crack growth
COD	Crack opening displacement
CT	Compact tension
OCP	Open circuit potential
EIS	Electrical impedance spectroscopy
PDP	Potentiodynamic polarization
CPE	Constant phase elements
DAQ	Data acquisition system
IMCs	Intermetallic compounds
Rp	Polarization resistance
Rs	Solution resistance
Z_{im}	Imaginary component of impedance
Z_{re}	Real component of impedance

LIST OF SYMBOLS

v	Linear speed or traverse speed
W	Rotational speed
Q	Activation energy
μm	micrometer
mm	millimeter
T	Temperature
T_{MP}	Melting temperature
f_{HABs}	Fraction of high angle boundaries
f_{LABs}	Fraction of low angle boundaries
HV	Vickers hardness
Ɵ	Work hardening rate
E_{cor}	Corrosion potential
I_{cor}	Current density
a	Crack length
K	Stress concentration factor
ΔK	Stress concentration factor range
da/dN	Fatigue crack growth rate

CHAPTER 1

INTRODUCTION

This chapter introduces the subject matter of the thesis, including the history of welding, the principle of friction stir welding, the key features of aluminium alloys, and the welding of aluminium alloys. The scope of present research lies in an increasing demand for aluminium alloys in various engineering sectors. The thesis discusses the influence of brass interlayer and cooling media on friction stir welded AA6061 alloy.

1.1 Background

Welding is a fabrication technique that involves fusing two or more parts using pressure, heat, or both to create a joint as the parts cool. Most frequently, welding is involved with metals and thermoplastics. The finished welded joint is known as a weldment. The history of welding traces back to ancient times. The earliest known examples belong to the Bronze Age. The circular gold boxes were produced by pressure-welding lap joints together. During the Iron Age, Egyptians and other people in the eastern Mediterranean region learned to weld iron together. C.L. Coffin of Detroit was granted the first U.S. patent for an arc welding process with a metal electrode in 1890. In the early 1900s, Strohmenger invented a coated metal electrode in Great Britain. Welding was enlisted to fulfill the tremendous demand for armament production that the First World War generated. Numerous American and European companies sprung up to manufacture the necessary equipment in response to the need for welding machines and electrodes. P.O. Nobel invented automatic welding in 1920. Later Gas tungsten arc welding was invented in 1926. Meredith invented and patented Heliarc welding (helium for shielding) in 1941. Battelle Memorial Institute invented gas shielded metal arc welding in 1948. The same principle was employed in gas tungsten arc welding by replacing tungsten electrodes. Many welding techniques were subsequently developed to increase their uses. In 1940, the French Atomic Energy Commission invented electron beam welding.

1.2 Fusion welding

Fusion welding processes are any welding processes in which the parent metals and filler material faying surfaces melt down during welding to generate weld beads. As a result, heat is always accompanying these activities. The use of filler material is optional. There are several different types of fusion welding techniques, which can be further classified based on the heat source. Metal Inert Gas (MIG), Gas Tungsten Arc Welding (GTAW), Laser Beam Welding

(LBW), and Beam Welding (EBW) are the most prevalent types of fusion welding processes used for aluminium alloys welding. Fusion welding has various disadvantages because all these processes entail melting base metal and solidifying it to form the weld. Welding of two dissimilar metals is challenging, especially if the melting temperatures and coefficients of thermal expansion are different. Porosity, voids in the fusion zone, and solidification cracks on the weld bead are some of the issues that occur in fusion welding processes. Due to extreme heat, a noticeable heat-affected zone exists surrounding the weld. All these defects and factors reduce the mechanical properties such as tensile strength, fatigue, and hardness.

1.3 Solid-state welding

Solid-state welding procedures are those in which no external heat is supplied, and the workpiece is joined in a solid state. There is no usage of filler metal in these welding techniques, and welding does not include molten base or filler material. The formation of welds is the consequence of an intermolecular diffusion process in which the interface molecules of the workpieces diffuse from high concentration to a region of low concentration as a result of the application of pressure. Several techniques are utilized to generate heat, accelerating the diffusion process between surfaces. Because these welding methods do not affect the mechanical or physical properties of the base material, they are frequently used in industrial applications. These are excellent joining methods for heat-sensitive materials. Solid-state welding comprises both the oldest and the most recent welding methods. Since the base metal does not melt and form a nugget, several methods have advantages. The joined metals retain their original properties without many heat-affected zone problems. Solid-state welding has a much smaller impact on thermal expansion and conductivity than arc welding when combining dissimilar metals. Cold welding, forge welding, explosive welding, friction welding, roll welding, ultrasonic welding, and friction stir welding (FSW) are some solid-state welding procedures. FSW is unique among solid-state deformation-based methods since the materials move and combine to form the joint. If FSW is performed correctly, it offers remarkable results, which is why it has been employed successfully in various aerospace, automotive, and shipbuilding applications.

1.4 Friction stir welding

Friction Stir Welding (FSW) is a novel solid-state joining process used to join Al alloys, in which the joints are produced below the solidus temperature of the weld metal. FSW is an advanced variant of solid-state joining processes. FSW was invented by Wayne Thomas et al.

at The Welding Institute (TWI), London, UK, in 1991. Initially, FSW was used for the joining of aluminium and its alloys as an alternative to conventional fusion welding techniques. FSW, a mature solid-state welding process that incorporates mechanics, temperature, metallurgy and interactions, has evolved into a revolutionary welding process due to the high-quality joints, environmental friendliness, and energy efficiency. FSW represents the most recent and significant improvement in metal joining technology in the previous two decades. Since FSW produces no spatter, requires no protective gas or welding wire, and no material melting, it efficiently avoids common fusion welding defects such as porosity and solidification cracks. Hence, FSW was also successfully employed to weld similar Al alloys and dissimilar materials such as Al to Mg, Al to Cu, and Al to steel.

1.4.1 FSW Working principle

FSW uses a rotating non-consumable tool with a shoulder and pin to join the weld plates. During welding, the rotating tool is inserted at the abutting edges of two plates and is enforced to travel along the line of action as represented in **Figure 1.1**.

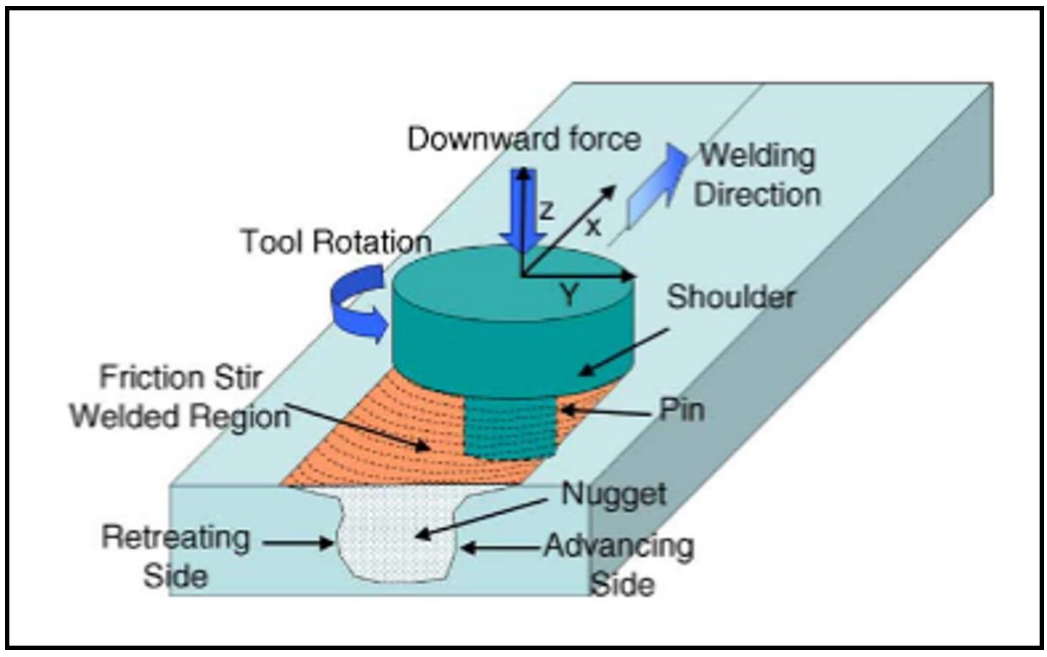

Figure 1.1 Schematic representation of FSW (Mishra and Ma 2005)

The frictional heat generated between the weld plates and the tool interface plasticizes/deforms the weld metal. The tool stirring action forces the deformed materials to flow from the advancing side (AS) to the retreating side (RS) and forges it behind the tool to form a weld joint. The rotation of the tool pin, on the other hand, causes deformation or churning, which generates more heat. Extreme deformation and material flow from the tool's leading edge to its

trailing edge occur in the plasticized material surrounding the pin, which is forged into the joint. Thus, the two plates create a solid-state interface. Due to the tool rotational and traversing speeds, the velocities of two symmetrical locations on the AS and RS sides are not the same. As a result, heat transfer and material flow on both sides of the weld are asymmetric. Generally, the radial tangent of tool rotational and traverse speeds are in the same direction in the AS but not in the RS.

1.4.2 Fundamental terminologies in FSW

Shoulder: It is a part of the FSW tool that deforms the workpiece's top layers and accommodates the material deformed by the pin. The preferable shoulder-to-pin diameter is 2-3.

Pin/probe: The end part of the tool completely penetrates into the base metal to make the weld line.

Tool rotational rate or speed: The rate at which the FSW tool revolute, typically specified in rev/min or rotations per minute (rpm).

Traverse speed: Rate at which the welding operation progresses in the welding direction typically specified in mm/min.

Tool tilt angle: Also called spindle head tilt, it is the angle between the axis of the spindle and the normal axis of the working plates.

Advancing side (AS): The side of the working plate where the tangential direction of tool rotational and tool transverse speed are the same.

Retreating side (RS): Side of the joint where the tangential direction of tool rotational is opposite to the transverse speed.

Leading edge: Un-processed region of tool front along the line of action.

Trailing edge: Processed region of back to the tool along the line of action.

Plunge depth: The depth up to which the FSW tool shoulder penetrates the working metal.

Start dwell time: The time during which the tool rotates at the same location after complete penetration to achieve sufficient plastic deformation for processing. Usually, the start dwell time varies from 30 to 120 sec depending upon the hardness of the working plate.

End dwell time: The time during which the tool rotates at the same location for easy withdrawal after processing. Usually, the start dwell time varies from 30 to 45 sec.

Axial force: Force applied on the working plate during FSW.

Cavity: The discontinuity in the form of void due to improper selection of process parameters.

Exit hole: The common defect formed in FSW due to tool withdrawal at the end of the weld.

Flash: Material expelled along the weld toe during FSW.

1.4.3 Process parameters of FSW

The primary purpose of any welding process is to produce defect-free welds with quality weld joints such as strength and appearance. The bond formation during FSW determines the quality of the weld joint. The tool rotational speed affects a majority contribution of the heat generated during FSW. The temperature induced in the stir zone is determined by the tool size, shape, rotational speed, and traverse speed (Yang et al. 2019). The rotational, traverse speed and axial force influence the amount of heat input within the stir zone. The greater the diameter of the tool, the faster it rotates, and the slower it traverses, the more heat it generates.

The lower heat input within the weld is produced by the faster traverse speed or, the lower rotating speed. This lower temperature may not adequately soften the material, resulting in incorrect material flow, broken pins, and the formation of defects. The quantity of heat generated during welding has a significant impact on the mechanical and corrosion properties of the welded components. Excessive heat causes grain coarsening, which results in inferior mechanical and corrosion properties (Gomathisankar et al. 2018). Reduced heat input may help to overcome grain coarsening. The temperature should not be lowered to the point where the material beneath the probe softens. As a result, proper welding parameters must be selected to ensure that the temperature around the tool is high enough to allow appropriate material flow. During welding, the heat generation affects the microstructure, resulting in unique microstructures in different regions.

1.4.3.1 Tool traverse speed and rotational speed

The weld joint quality mainly depends on tool traverse and rotational speed, which influences the heat generation during FSW. The tool's traverse and rotational speed must be carefully chosen to produce an effective FSW joint. In order to minimize stresses acting on the tool during welding, the base material must be heated to a temperature where significant plastic deformation can occur quickly. Heat input to the workpiece is often increased by increasing rotational speed or decreasing transverse speed. High welding forces can damage the friction stir tool, while insufficient heat generation can lead to holes and defects inside the stir zone (Dialami et al. 2019). On the other hand, the temperature that is too high could melt the material surface layer and result in cavities or have an impact on the microstructure through re-solidification. The FSW process parameters must be chosen within the "processing window," as shown in **Figure 1.2** to produce a high-quality weld since these factors lower the joint

quality. However, the process parameters depend on the alloy, and the processing window changes. As a result, the permitted processing parameters are further constrained when two incompatible materials or alloys are welded.

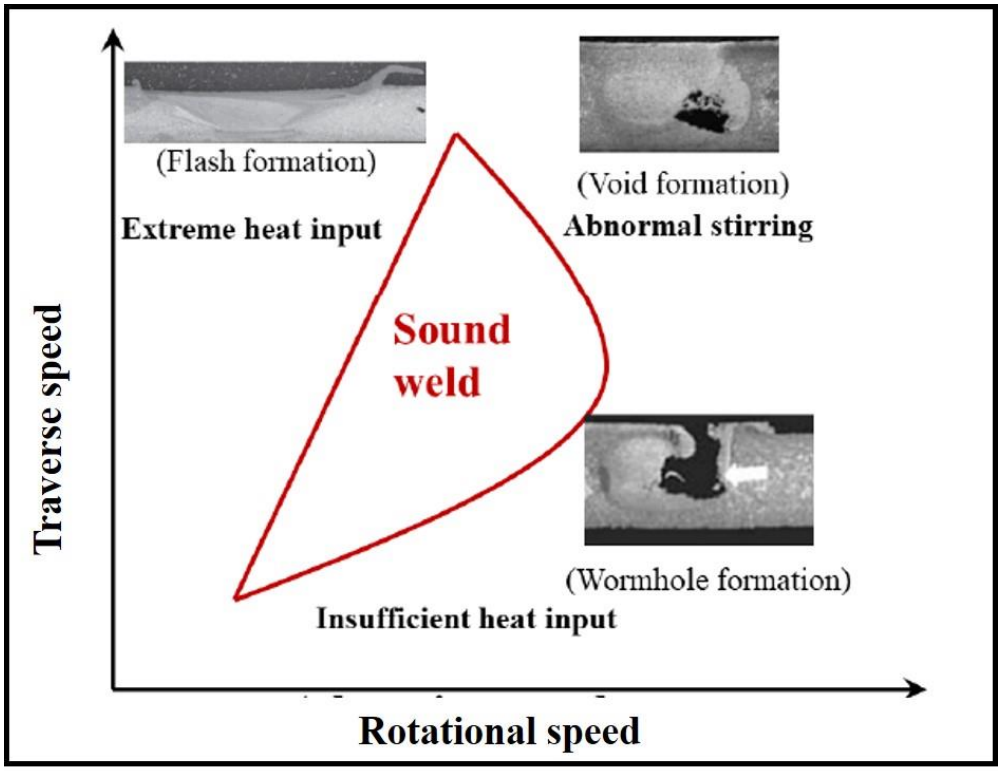

Figure 1.2 FSW process window and associated welding defects (Dialami et al. 2019)

1.4.3.2 Tool tilt angle and plunge depth

The tool tilt angle is one of the important process variables that play a crucial role in material flow during FSW, influencing the size and position of weld flaws. The distance between the lowest surfaces of the shoulder inserted in the base plates is defined as tool plunge depth. This is necessary to generate pressure beneath the tool for the material to be forged adequately at the tool trailing edge. Inadequate plunge depth can result in incorrect welding depths and the creation of material cavities. A high plunge depth can cause the tool to be damaged by rubbing between the backing plate and the pin. Furthermore, suppose the plunge depth is adjusted too high; in that case, a significant quantity of flash will be generated, resulting in a big difference in thickness between the welded zone and the unaffected material. Generally, 2-4^{o} tool tilt can be applied to the tool, pushing the front higher than the back. This is intended to facilitate forging at the tool's trailing edge and increase the quality of the weld. However, due to the tool's inclination, the material's surface contact with the shoulder of the tool is reduced, resulting in a decrease in heat input. As a result, the tilt angle is typically restricted to 4°, and

a plunge depth of 0.2 to 0.3 mm is utilized to increase the contact area. At a tool tilt angle of 2° to 4°, the material can be heated to a fully plasticized state with viscosity and material flow strain rate that meet the requirements for correct stirring and forging of the weld material, resulting in defect-free welds. The tool tilt angle of higher than 4° resulted in void defects (Meshram et al. 2018).

1.4.4 FSW tool design

The tool geometry is important in friction stir welding to achieve suitable microstructures in the weld. The tool comprises a shoulder and a pin, as shown in **Figure 1.3**, both of which are essential in the welding process. The tool improves joint quality by directly influencing characteristics such as grain size, microstructure homogeneity, and material flows throughout the joint. The shoulder is in charge of generating much of the required heat while the pin transfers the plasticized material. The tool pin's primary function is to act as a "small" solid-state extrusion pump to propel material up and down the stir zone and around the pin. In addition, the pin assists in fracturing and dispersing big particles, oxides, and particles within the material. Each design of the pin and shoulder has undergone various upgrades and modifications, and each is believed to have a somewhat different purpose (Zhao et al. 2013).

Various tool features have been created over the years by researchers. In addition to selecting certain geometries, the pin length and diameters must be chosen carefully. The selection of tool design is determined by the individual application, thicknesses, and materials to be welded. Different researchers worked on tool design and proposed a range of shoulder diameter to thickness of weld plates; the suggested range is 3-3.5 (Jaiganesh et al. 2015). The suggested shoulder-to-pin diameter is 2-3 (Mehta et al. 2011).

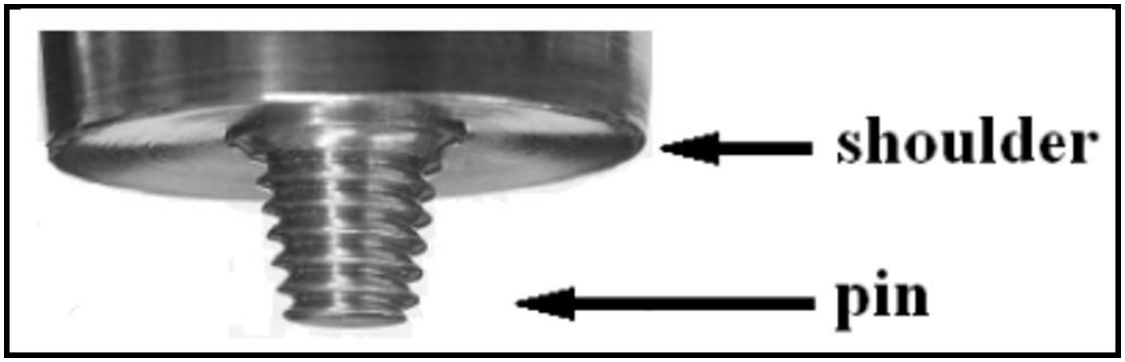

Figure 1.3 Parts of FSW tool (Reads 2021)

Several researchers have investigated different pin configurations, although most have been unsuccessful or unusual. NASA has studied a retractable pin feature that permits the probe

to change length during processing. As a result, plunge depth can be easily modified during welding. The pin can alternatively be gradually retracted at the final exit point to avoid the exit hole. This is especially important during repair welding and when material waste must be reduced. The shoulder design can also be modified to enhance the joining process. Scrolls or grooves are typically employed on the shoulder during the FSW process when the tilt angle is zero. This is expected to enhance the development of a fine grain structure by reducing flash and enhancing material mobility close to the weld surface. But when the tool is tilted, the concave shoulder design is mostly utilized. This arrangement prevents materials from being extruded outside of the shoulder and maintains downward pressure on the base metals to assurance proper forging and the avoidance of defects. As a result, flash formation on the weld bead can be avoided. Cylindrical threaded tool pin profile is most used for proper material flow, allowing scratching and mixing interlayer particles into the Al matrix from top to bottom in welding of dissimilar materials. Moreover, once tool penetrates completely, material at bottom of the pin and adjacent to the pin is forced into threads. Due to the stirring action of the pin, the material is forced to move along the helical-shaped threads. In other words, material is forced into the threads and moves from bottom to the top of the pin. This action causes uniform material flow and gives good material mixing (Mehta et al. 2015).

1.4.5 FSW tool material

Tool material is one factor that plays a major role in weld quality. The primary characteristic is the hardness of the tool should be more than the materials to be welded. Hence tool wear can be reduced, resulting in defect-free joint throughout the length. The coefficient of friction affects how much heat is produced between the tool shoulder and the surface of the base metal. Higher heat generation will result from higher coefficients of friction. Moreover, the tool's hardness influences the coefficient of friction. The chemical composition of material substantially influences the hardness of the tool. A softer tool will generate less heat, resulting in fewer defects and vice versa (Padmanaban et al. 2009). The tool should have enough compressive and shear strength at high temperatures to avoid tool failure during welding.

1.4.6 Selection of tool materials

Generally, Al alloys are welded using tool steels and high-speed steels. Tungsten-based alloys, Tool steels, Ni/Co-based steels, Refractory materials, Carbides, Inconel alloys, metal matrix composites, Mo-based alloys, Titanium-based alloys, and Poly cubic boron nitride (PCBN) are used as tool materials for FSW (Collier et al. 2003). Refractory metals like tungsten-based

alloys and PCBN are used for welding high-strength materials. However, tool steels are used for the joining/processing of aluminium and its alloys.

- **Characteristics of tool material**

Many distinct material characteristics may be considered essential in FSW, but their ranking is determined by weld material, tool life, and other considerations. Besides material physical properties, various practical considerations may impact tool material selection.

- **Elevated temperature strength and stability**

The tool material must withstand compressive loads when it first touches the base material. It should also have enough compressive and shear strength at high temperatures to keep the tool from breaking while welding. In addition to being strong enough at high temperatures, the tool must be strong enough and stay in the same dimensions while welding.

- **Wear resistance**

Excessive tool wear alters the geometry of the tool, decreasing weld quality and increasing the chances of producing flaws. In FSW, tool wear is caused by adhesive, abrasive, or chemical processes. The precise wear mechanism is governed by the interaction between the workpiece and the tool's materials, the selected tool's geometry, and the processing variables.

- **Tool reactivity**

The tool material should not react with the work materials or environment, as this will change the tool surface characteristics.

- **Tool fracture**

The stresses and strains created locally when the tool initially contacts the base metal surface are sufficient to cause the tool fracture, even when mitigation techniques are employed (a pilot hole, low plunging speed, and preheating of the work material). It is widely accepted that the tool penetration and dwell time produce the most harm to the tool.

- **Coefficient of thermal expansion**

Large variations in thermal expansion coefficients between the shoulder and pin materials cause either the shoulder or the pin to expand relative to the shoulder. These factors increase the stress between the shoulder and the pin, which causes the tool to fracture.

1.4.7 Microstructure evolution of FSWed joints

As previously stated, the base metal (BM) flows without melting due to the generated heat and

deformation, allowing the tool to be moved along the weld line. The deformed material is transmitted from the AS to RS of the tool pin, which is subsequently forged by the tool shoulder, producing a solid-state bond between two plates. Significant plastic deformation in the stir zone leads to extensive microstructural and mechanical property modifications. FSW splits joint microstructure into discrete zones. **Figure 1.4** depicts the typical macrostructure of an FSWed joint. As illustrated in **Figure 1.5**, the zones can be classified as stir zone (SZ), thermo-mechanically affected zone (TMAZ), heat-affected zone (HAZ), and base metal (BM). Each zone is subjected to distinct thermal cycles and temperature combinations during FSW and has a unique microstructural evolution.

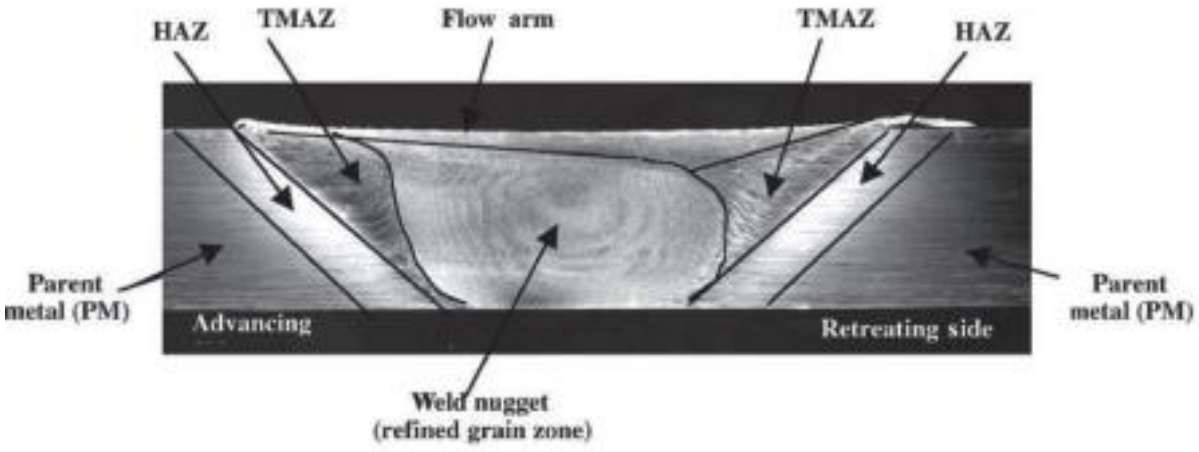

Figure 1.4 Optical micrograph showing SZ, TMAZ, and HAZ (Mishra et al. 2005)

Stir Zone

This region contains equiaxed fine grains and is situated in the center of the weld (the location of pin during welding), as displayed in **Figure 1.4**. The combination of heat and substantial plastic deformation during FSW generates dynamic recrystallization (DRX) in the weld center. Welding parameters such as rotational speed, traverse speed, and axial force affect the region's geometry. The grains in the SZ (**Figure 1.5(b))** are typically smaller than those in the BM (**Figure 1.5(a))**. Multiple concentric circles, compared to onion rings, are characteristic of SZ. Furthermore, the volume of the SZ is governed by tool geometry. Typically, the shoulder width controls the SZ breadth, while the pin length determines the SZ depth. In addition, it is noted that the grain size distribution in the volume of the SZ is not uniform. Not only the surface but also the cross-section of the SZ exhibit variation. Typically, this results from the strain intensity and temperature gradients present during the complex material deformation. Although variations in grain size, particle number density, and texture have been proposed as potential causes, the precise cause of these rings has yet to be determined.

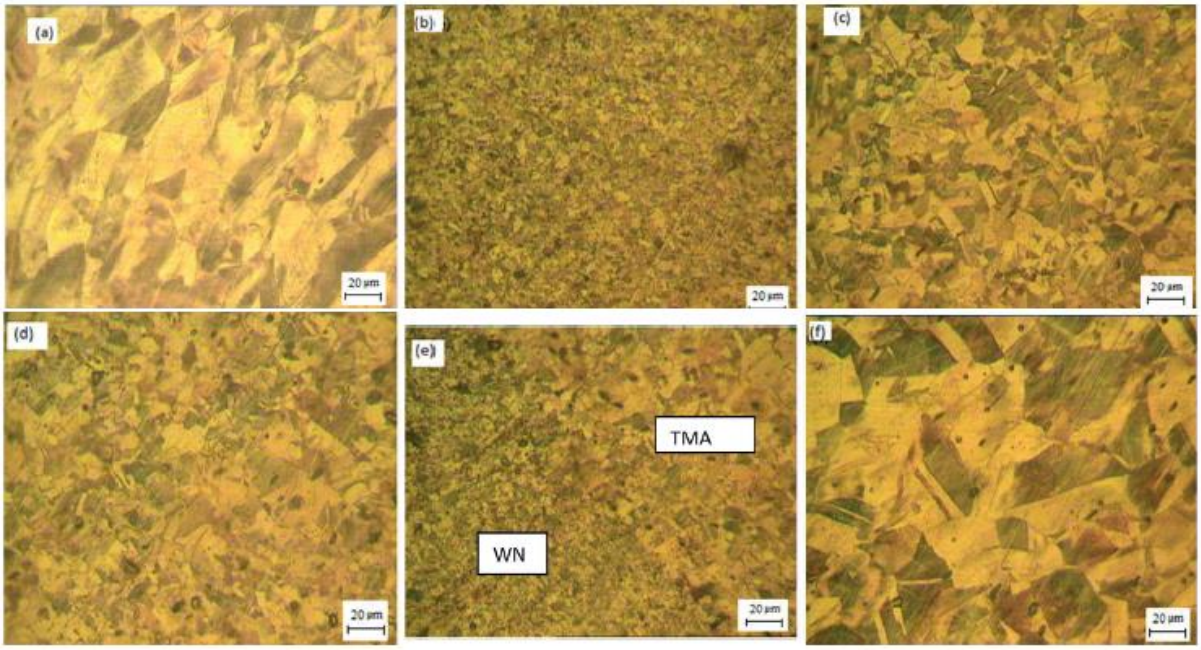

Figure 1.5 Microstructure of various zones (a) Base metal, (b) SZ, (c) TMAZ- AS, (d) TMAZ- RS (e) SZ-TMAZ interface and (f) HAZ (Srirangarajalu et al. 2016)

Thermo-mechanically affected zone

The thermo-mechanically affected zone (TMAZ) size varies from a few microns to millimeters and appears on both sides of the SZ, as shown in **Figure 1.4**. In this region, the FSW tool has plastically distorted the material, and the resulting heat has influenced the base metal. Due to insufficient heat and plastic deformation, this region frequently possesses elongated or twisted grains (**Figure 1.5(c))**, and recrystallization does not occur.

Heat-affected zone

This zone is formed adjacent to both sides of the TMAZ, as shown in **Figure 1.4**. This zone, which is closer to the center of the weld, has experienced a heat cycle, which has altered the microstructure or mechanical properties. At this stage, however, no plastic deformation has developed. This region's most common metallurgical phenomena are grain coarsening (**Figure 1.5(f))**, dissolution, and coarsening of strengthening precipitates. Large grains similar to the base metal can be observed in this region.

Base metal

This zone is next to the HAZ on both sides, and during FSW, there are no plastic deformation or temperature effects in this area. So, after FSW, neither the microstructure nor the mechanical properties are changed. This area is also called the "unaffected region." The base metal has very long pancake-shaped grains that make up its microscopic structure.

1.4.8 Defects formed in FSWed joints

The inappropriate selection of process parameters and tool geometry produces defects in the stir zone. Various kinds of defects observed during FSW are shown in **Figure 1.6**, and the reason for forming those defects is summarized in **Table 1.1**.

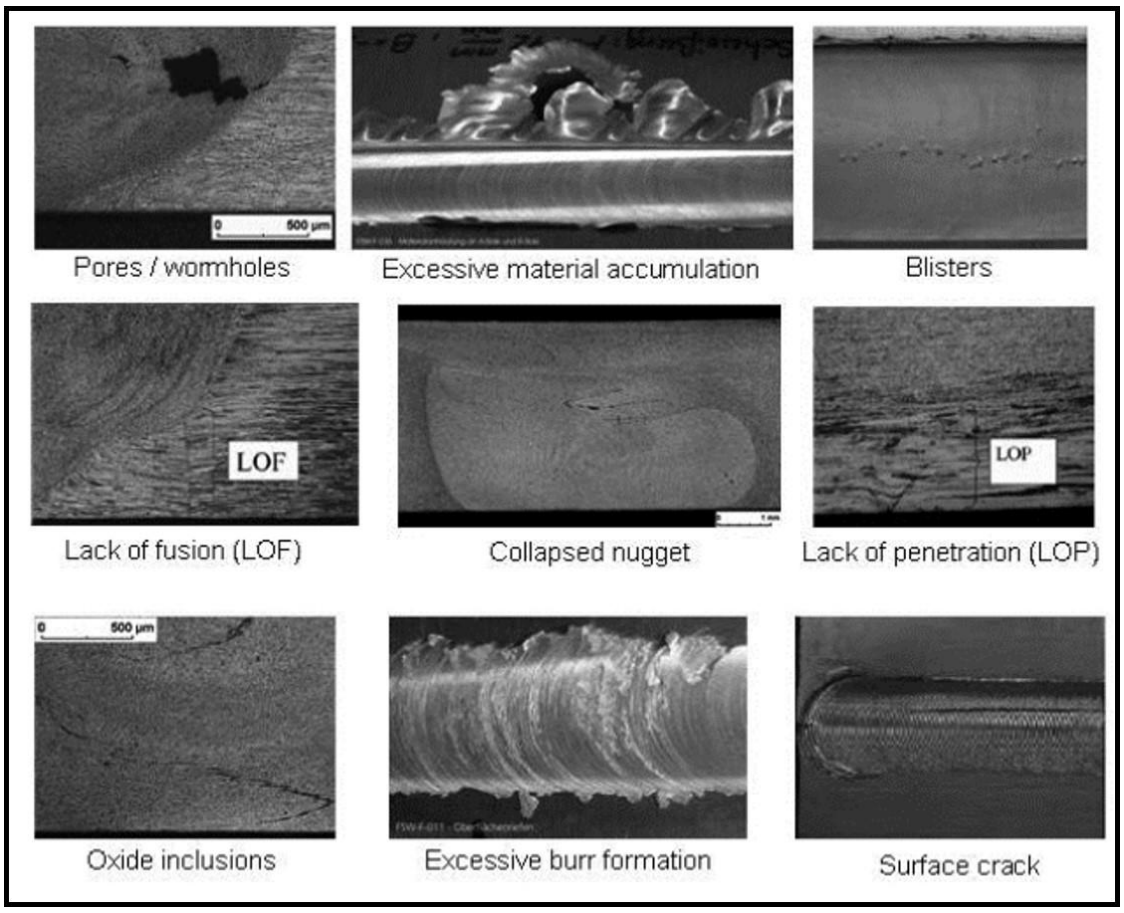

Figure 1.6 Defects formed in FSW (Strass et al. 2014)

1.4.9 Advantages of FSW

FSW has significant advantages over fusion welding processes due to its solid-state nature, which eliminates any potential problems in cooling from the liquid phase. During FSW, issues like porosity, solute redistribution, and solidification cracking do not arise. It has been discovered that FSW produces low defect concentrations and is remarkably resistant to fluctuations in parameters and materials. FSW, a relatively new welding technology, has various advantages over fusion welding, including energy efficiency.

- As the process is solid-state, it is referred to as "green" technology because it produces no fumes or gases.
- With grain refinement, the mechanical qualities of the finished welds surpass those of

fusion welding processes.

Table 1.1 Reasons for the formation of defects in FSW (Strass et al. 2014)

S. No:	Defects	Reason
1	Wormhole/pores	Generally observed on advancing side • Very high weld speed • Inadequate forging force • Inappropriate work clamping
2	Excessive material accumulation/burr formation	More material released from the surface in the form of a flash. • High tool traverse speed • More plunge depth • High forging pressure
3	Lack of fusion/penetration	It is a geometric defects • Inappropriate tool geometry selection • Too high rate of tool traverse • Thickness differences in work materials to be joined and the gap between the work materials
4	Nugget collapse	Improper development of nugget shape towards advancing and retreating side. • High rotational speed • Very high weld pitch
5	Surface crack	The crack on surface of weld • Insufficient forge pressure • Less plunge depth • Improper work clamping
6	Blisters	Tearing of material on the surface of the stir zone behind the tool pin. • Too hot weld • Very high weld pitch • Sticking processed metal to tool pin

- FSW is the most promising technology for joining non-weldable aluminium alloys, as it eliminates many issues that emerge with fusion welding.

- Reduced energy consumption since the frictional heat generated at the work-tool interface is sufficient to achieve plastic deformation.
- Plate or sheet distortion (residual stresses) is less with improved fatigue life due to fine grain size.
- Many dissimilar material combinations can be joined (for example, different grades of aluminium alloys, aluminium to steel, aluminium to titanium etc.)

1.4.10 Limitations of FSW

- When the tool is withdrawn at the end of the process, an exit hole is left behind.
- Generally, tool forces are high, and heavy-duty clamping is necessary. A skilled operator is required.
- The maximum thickness of the material to be joined is limited to 50 mm with conventional tools (in single side welds) and 100 mm with bobbin tools (in double side welds).
- Tool wear is a common phenomenon during FSW while welding hard materials.

1.4.11 Applications of FSW

FSW has been used in several commercial applications, as listed below

Marine Industry:

- Aluminum Super structures of cruise ships (Seven Seas Navigator)
- Japanese Fast Ferry (Ogasawara) in 2004

Automobiles:

- Long low distortion (25 m welds) double skin extrusions for railways
- Suspension parts, Crash boxes, and wheels
- Engine cradles

Aerospace Industry:

- Fuel tanks for un-manned Delta II and Delta IV rockets
- Eclipse 500 business jet frame

1.5 Aluminium alloys

Aluminium is the most common metal on earth and the third most common element. It makes up 8% of the crust of the earth. Aluminium is the most used metal after steel because it can be used in many aspects. Due to its unique combination of qualities, such as its low density (2.7

g/cm^3), softness, high ductility, etc., the demand for aluminium has increased over the past four decades. The unique combination of these features made aluminium one of the most desirable, adaptable, and cost-effective metals for various applications. In addition, aluminium's low melting point temperature (TMP ≈ 660^o C) allows its components to be made more quickly than other lightweight metals. Generally, automobile components can have a significant effect on the environment. Using lightweight materials can assist in reducing vehicle weight and enhancing fuel economy, reducing the impact on the environment. The demand to reduce vehicle weight has led to a gradual decline in the amount of steel and cast iron used in vehicles and a rise in the number of alternative materials, particularly aluminium and plastics, as shown in **Figure 1.7**. Pure aluminium can be alloyed with many other metals to produce a wide range of physical and mechanical characteristics with the following designations (Davis et al. 2001). The alloys are separated into two categories: wrought alloys and cast alloys.

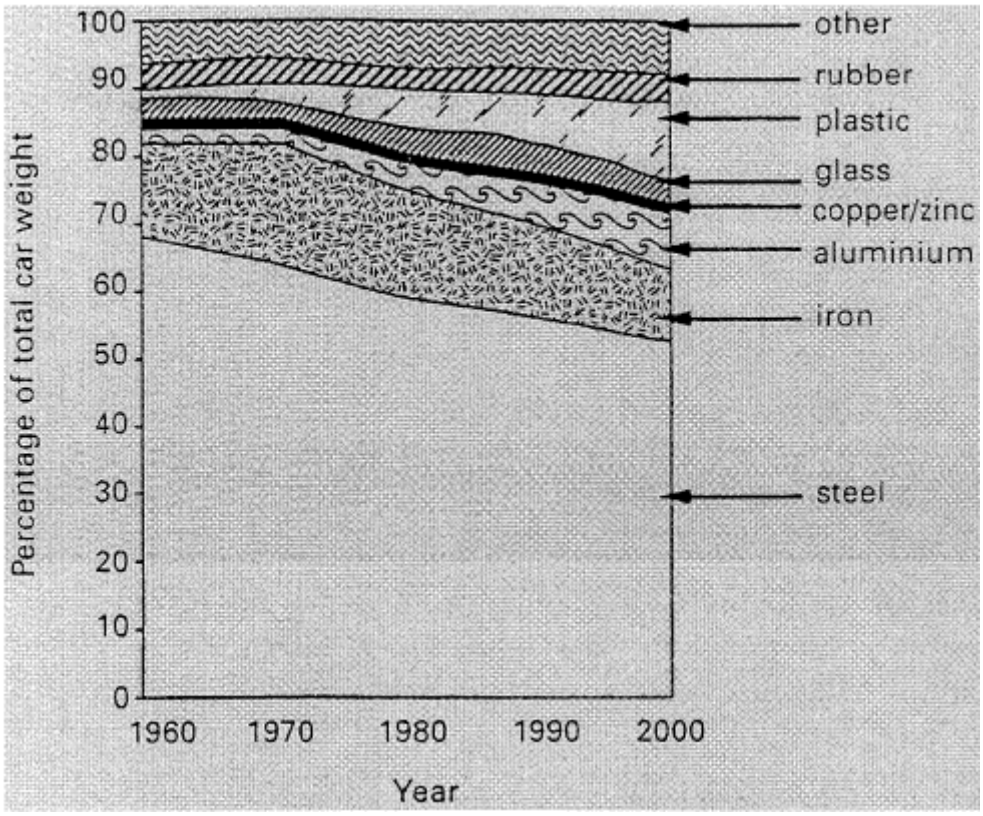

Figure 1.7 The change in material consumption in the average car (Miller et al. 2000)

1.5.1 Wrought Aluminium Alloys

Even though some alloys are often used as castings, most Aluminium alloys are made as wrought plates or sheets, which are widely used in aerospace and structural applications. Several wrought alloys depend on work hardening by mechanical reduction and a combination

of heat treatment procedures to improve their properties; these are known as work hardening alloys. Due to precipitation, heat-treatable alloys have greater strength than non-heat-treatable alloys. Precipitates contained in heat-treatable alloys can effectively act as barriers to dislocation movement and increase the strength of the material. However, the welding procedures involving elevated temperatures, these precipitates are dissolved and coarsened, resulting in a change in microstructure and mechanical properties.

An international identification system proposed by the American aluminium association to further define wrought aluminium alloys has been authorized. Each wrought Al alloy is identified by a four-digit code, letters, and numbers indicating the tempering condition. The essential digit is the first one, which classifies the major alloying element. The second single digit, if different from 0, signifies a modification of the specific alloy, whereas the third and fourth digits are arbitrary numbers used to identify a particular alloy in the series. (Polmear et al. 1995). Example: In alloy 5183, the number indicates that it is of the magnesium alloy series, the 1 indicates that it is the 1st modification to the original alloy 5083, and the 83 identifies it in the 5xxx series. The designation system of wrought Al alloys is listed in **Table 1.2**.

Table 1.2 International designation system for Al wrought alloys (Callister et al. 2003)

Series	Major Alloying Elements	Heat treatable
1xxx	Pure	-
2xxx	Cu	Yes
3xxx	Mn	No
4xxx	Si	No
5xxx	Mg	No
6xxx	Si & Mg	Yes
7xxx	Zn	Yes
8xxx	Other	-

A suffix indicates the tempering condition of heat-treatable wrought Al alloys following the four-digit number. The state of an alloy is typically designated by a letter and a number, as shown in **Table 1.3**.

Table 1.3 Tempering conditions of wrought aluminium alloys (Polmear et al. 1995)

Temper condition	Description
T3	Solution annealing, cold working followed by natural ageing
T4	Solution annealing followed by natural ageing
T5	Cooled from high-temperature shaping followed by artificial ageing
T6	Solution annealing followed by artificial ageing
T7	Solution annealing followed by artificial over-ageing
T8	Solution annealing and cold working followed by artificial ageing

In **Table 1.4**, the temper condition for non-heat-treatable alloys is represented individually.

Table 1.4 Temper conditions of non-heat-treatable wrought Al alloys (Polmear et al. 1995)

Temper condition	Description
F	As-fabricated
O	Annealed
H	Work hardened (wrought components)
H1	Work hardened only
H2	Work hardened and partially annealed
H3	Work hardened and stabilized

1.5.2 Cast Aluminium alloys

Components of aluminium alloy with complicated geometries are typically net-shaped castings. The vehicle industry extensively uses cast aluminium goods, such as engine blocks, connecting rods, piston-cylinder assemblies, gearboxes, steering knuckles, etc. In contrast to wrought aluminium alloys, cast aluminium alloys are identified using a three-digit system followed by a decimal value. Similar to wrought aluminium alloys, the first and second digits represent the major alloying elements and alloy purity or concentration of secondary alloying elements. In all alloys, the decimal value specifies the casting alloy limits.

Table 1.5 International designation system for cast aluminium alloys (Callister et al. 2003)

Series	Major alloying elements	Heat treatable
1xx	Pure	-
2xx	Cu	Yes
3xx	Si with Cu and/or Mg	Yes
4xx	Si	No
5xx	Mg	No
6xx	Unused	-
7xx	Zn	Yes
8xx	Ti	No
9xx	Other	-

Table 1.5 displays the international designation method adopted by the American Association System for classifying cast aluminium alloys. However, there is no universally approved classification system for tempered conditions for cast aluminium alloys. Following the alloy identification is a suffix denoting the tempering condition of the cast alloy, as detailed in **Table 1.6.**

Table 1.6 Tempering conditions of cast aluminium alloys (Polmear et al. 1995)

Temper condition	Description
M	As-cast
TB	Solution annealing and natural ageing
TB7	Solution annealing and stabilizing
TE	Casting followed by artificial ageing
TF	Solution annealing and artificial ageing
TF7	Solution annealing, artificial ageing, and stabilizing
TS	Thermal stress relieving

1.6 6xxx aluminium alloys

Silicon and magnesium are the major alloying elements in the 6xxx series alloys in the quantities required to produce strengthening precipitate such as magnesium silicide (Mg_2Si), interpreting them as susceptible to heat treatment. These alloys are naturally susceptible to

solidification cracking. Hence they should not be welded using fusion welding techniques autogenously (without filler material). Generally, 6xxx series alloys have better corrosion resistance, formability, machinability, and weldability but are not as good as 7xxx series alloys. Furthermore, 6xxx alloys are stronger than most of the 2xxx and 7xxx alloys. This group of heat-treatable alloys can be produced in the T4 state (solution annealed but not precipitation heat-treated) and then strengthened by precipitation strengthening. After forming, the T6 material undergoes a precipitation heat treatment to achieve its complete characteristics. 6xxx series alloys are good for the components and structures that require good formability and are mostly employed in the automotive industry parts, hospitals, medical equipment, vehicle components, railroad cars, culinary equipment, etc. The relations between some of the most often utilized alloys in the 6xxx class are illustrated in **Figure 1.8** (Davis et al. 2001).

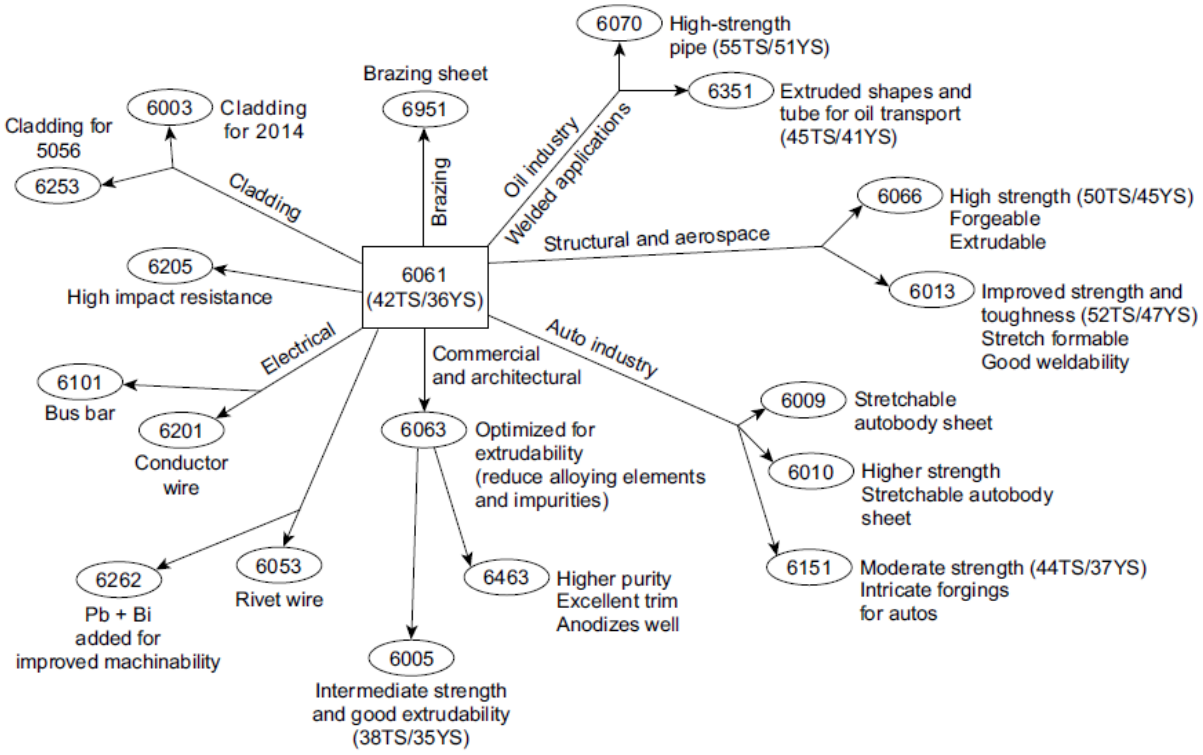

Figure 1.8 The relationships between some of the more widely used alloys in the 6xxx series alloys (Davis et al. 2001)

1.7 Definition of the problem

Literature review revealed that aluminium alloys are low in weight, have a high strength-to-weight ratio, and are fully recyclable, making them in high demand as steel substitutes. Usually, industrial and aerospace sectors focus on high strength joining of aluminium alloys. Even though fine and recrystallized grains were obtained using FSW, the softening at the SZ caused

due to weld thermal cycle results in decreased weld joint strength and deterioration of corrosion resistance. Weld strength can be restored by post-processing, such as post-weld heat treatment (PWHT), but PWHT is time-consuming, cost-effective, and is not possible to perform on non-heat-treatable Al alloys. One approach to overcome the thermal softening and improve weld strength is inserting a suitable interlayer between weld plates. During FSW, the interlayer mixes with base metal and forms a new phase, i.e., Intermetallic Compound (IMC). The formation of IMC in the stir zone can improve the mechanical properties of the weld joint. Even though better joint properties are obtained with the use of interlayer compared to without interlayer, the formation of the brittle and high density of IMCs in the SZ is a major problem. Generally, IMCs rich-zone tends to crack easily, while tensile deformation is the primary cause of premature failure of dissimilar joints. The formation and growth of IMCs are influenced by peak temperature and cooling rate. Therefore, water-cooling is employed to suppress the formation of brittle IMCs and reduce the grain growth in HAZ, enhancing the strength of the overall weld joint. As per the author's knowledge, the effect of brass interlayer on corrosion behaviour, damping behaviour, wear characteristics, fatigue crack growth behaviour and mechanical properties were not analyzed till now. Hence, the present study aimed at the influence of brass interlayer and water-cooling on microstructure, mechanical properties, corrosion resistance, wear characteristics, damping behaviour, and fatigue crack growth behaviour.

1.8 Research objectives and scope of research work

The present investigation focus on using brass interlayer and cooling media to improve the mechanical properties of friction stir welded AA6061-T6 alloy. The main objectives of the present investigation are as follows:

- To study the effect of brass interlayer on microstructure and mechanical properties of friction stir welded AA6061-T6 alloy.
- To study the combined effect of cooling media and interlayer on microstructure and mechanical properties of the welded joint.
- To study the corrosion resistance, wear rate, and damping capacity of welds joined with and without interlayer of natural cooling and water cooling.
- To study the fatigue behaviour of welds joined with and without interlayer of natural cooling and water cooling.

1.9 Methodology

1. Initially, the trial experiments were carried out to select optimum process parameters of FSW with interlayer (NCFSW) to get defect-free joint.

2. Conduct the experiments on FSW without interlayer using the optimum parameters and compare the results with interlayer such as tensile strength and hardness.

3. Conduct the water-cooled FSW (WCFSW) experiment with and without interlayer and compare the results with NCFSW.

4. Determine corrosion resistance, damping behaviour and wear characteristics of welds with and without interlayer under both cooling media (NCFSW and WCFSW).

5. Determine fatigue life and fatigue crack growth (FCG) rate of welds with and without interlayer under both cooling media (NCFSW and WCFSW).

1.10 Organization of thesis

The whole thesis was organized into five chapters: introduction, literature review, experimental procedure, results and discussion, and conclusions.

Chapter-1: This chapter provides a brief introduction to traditional joining techniques, solid-state welding, the working principle of friction stir welding, aluminium alloys, and applications.

Chapter-2: This chapter provides a complete assessment of the available literature on various friction stir welding process aspects pertinent to the current research challenge.

Chapter-3: This chapter describes the experimental approach used to conduct friction stir welding and several characterization procedures to fulfil the research aim.

Chapter-4: This chapter contains the explanation of results and discussion of each objective under separate headings.

Chapter-5: This chapter contains the summary of conclusions of the present work with possible remarks and future scope.

References

Publications

CHAPTER 2

LITERATURE SURVEY

This chapter briefly outlines the literature review on various aspects of friction stir welding (FSW), such as FSW of aluminium alloys, optimization of process parameters of FSW, use of different interlayers during FSW, combined effect of interlayer and cooling media during FSW, corrosion, wear and fatigue behaviour of FSWed joints. The summary of the literature work was presented at the end of the chapter.

2.1 FSW of aluminium alloys

The FSW technology was invented and patented by Thomas et al. (1991) at The Welding Institute (TWI) in the United Kingdom. They defined FSW as a continuous solid-state joining method that uses a non-consumable rotating tool with a stronger material shoulder and probe than the material to be welded. The FSW technique yields final plates with little distortion, a good appearance, and a reasonable cost. FSW is the most popular and promising joining technique for welding aluminium and aluminium alloys. FSW has also demonstrated its capacity to weld copper, copper alloys, steels, titanium, magnesium, polymers, and other dissimilar materials.

In addition, they summarised the application of friction stir welding in the transportation industry. The authors mentioned various uses for friction stir welding, including cryogenic fuel tanks, airframes, sheet bodywork, thin alloy skins in aerospace, automotive engine support frames, hull frame in ship building, coachwork and railway wagons for railways, etc. Thomas et al. (1991).

Friction stir welding generates a complicated thermo-mechanical interaction of factors, which affects the temperature cycles, severe plastic deformation of the material, dynamic recrystallization, and, ultimately, the structural weld integrity. FSW permits joining a wide variety of metals, including magnesium, copper, steel, titanium, and different dissimilar metal combinations (Nandan et al. 2008).

2.2 FSW of AA6061 alloy

After FSW, the stir zone (SZ) of the weld joint formed consists of equiaxed, fine grains due to severe plastic deformation (SPD) and dynamic recrystallization (DRX). Even though fine and recrystallized grains were obtained using FSW, the softening at the SZ caused due to weld

thermal cycle results in the decrease of weld joint strength and deterioration of corrosion resistance (Gharavi et al. 2015). Various researchers attempted to improve the weld strength of FSW joint by optimizing the process parameters, tool design, and post-weld heat treatment (PWHT). (Rajakumar et al. 2011) carried out multi-objective optimization methodology to enhance the mechanical and corrosion properties of FSWed AA6061 alloy. They performed multi-objective optimization using Response surface methodology (RSM). The optimized results are validated with experimental data. They observed that tool rotational and traverse speed are the two essential parameters affecting material flow and defect formation. The corrosion rate was estimated using the weight loss test. They concluded that multi-objective optimization utilising RSM is a valuable technique for optimising FSW process parameters to attain the optimum tensile strength without compromising the corrosion resistance of FSW joints. They suggested the optimum parameters to attain maximum weld strength. (Gomathisankar et al. 2018) Optimized FSW process parameters to improve the mechanical properties of AA6061-T6 using the Taguchi-based COPRAS decision model. They designed a Taguchi L9 orthogonal array design of experiments. ANOVA is used to predict the proportional contribution of the provided process parameters. They have concluded that welding speed is the most substantial parameter, followed by tool rotational speed and dwell time. Moreover, PWHT is the most used method for restoring mechanical properties. Different heat treatment procedures are followed to get the required strength, such as artificial ageing, followed by solution treatment (T6 condition), and solution treatment.

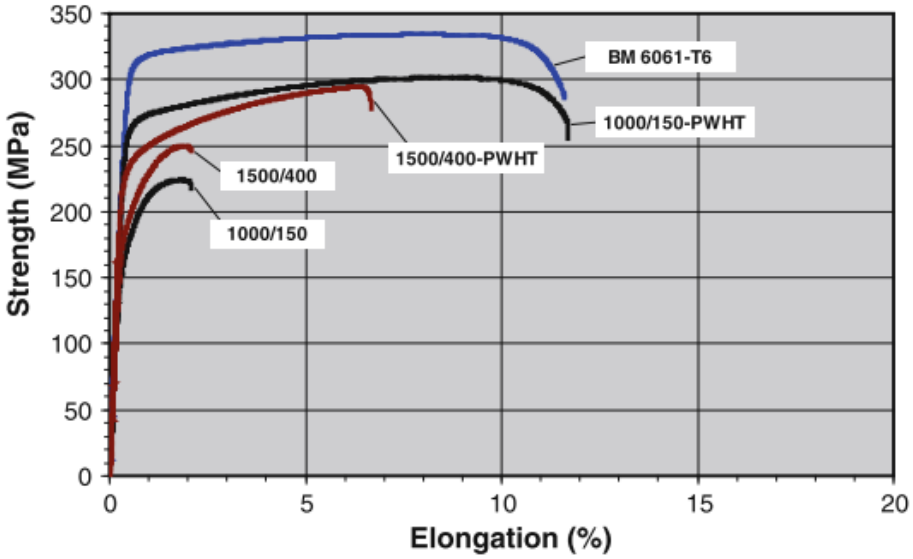

Figure 2.1 Representation of stress-strain curves of the T6-joints both in the as-weld and PWHT conditions (Ipekog et al. 2013)

Malopheyev et al. (2016) optimized the FSW parameters by varying the tool traverse speed, and they concluded that optimized tool traversed speed enhanced the mechanical properties due to the uniform distribution of precipitates. PWHT was performed on an optimized weld joint which increased the strength and ductility of the weld joint compared to the weld joint. Ipekog et al. (2013) investigated the effect of PWHT on microstructure and mechanical properties of FSWed 6061 alloy. Two different temper conditions (O and T6) were performed, and the improvement in mechanical properties was observed compared to the as-welded (AW) condition. They observed the grain refinement in all weld joints, and small grains were obtained for heat-treated samples. PWHT led to precipitation of uniformly distributed strengthening particles in the DXZs (Dynamically recrystallization) of joints formed in T6-temper conditions. **Figure 2.1** shows that heat-treated samples' tensile strength is higher than welded conditions at different process parameters.

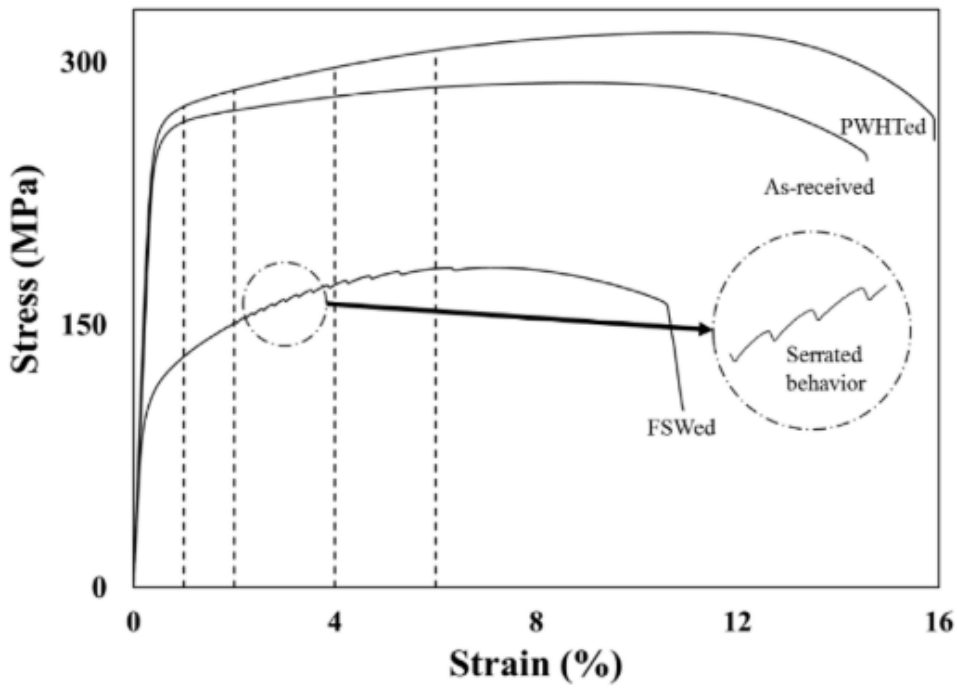

Figure 2.2 Stress-strain curves of weld joints (Baghdadi et al. 2019)

Baghdadi et al. (2019) investigated the effect of PWHT (T6) on the precipitation behaviour of FSWed AA6061 alloy. They observed that in as-welded conditions, the Portevin–Le Chatelier (PLC) effect caused the non-uniform distribution of strengthening Mg_2Si precipitates in the SZ, coarsening these precipitates in TMAZ and over ageing in HAZ. The above factors led to a decrease in weld joint efficiency of 65 %. Moreover, adding T6 PWHT following FSW decreased the PLC impact and restored the Al6061 mechanical characteristics to their previous

state, as represented in **Figure 2.2**. The PWHT also enhanced precipitation hardening via a more uniform distribution of Mg_2Si particles, which inhibited grain growth and increased dislocation density in response to the applied strain, hence enhancing the mechanical characteristics of the FSWed AA6061 alloy.

From the literature survey, it was observed that optimization of FSW process parameters and PWHT are time-consuming, and PWHT is not feasible in some practical applications (Krishna et al. 2011). To overcome the above-mentioned difficulties and enhance the joint strength and corrosion resistance, a few researchers suggested an approach to insert a suitable interlayer between weld plates.

2.3 Effect of interlayers on mechanical properties of FSWed Al alloys

Some researchers attempted to enhance the tensile strength and corrosion behaviour of FSWed Al alloys using various interlayers. The schematic representation of FSW with interlayer is shown in **Figure 2.3**. During FSW, the interlayer mixes with base metal and forms a new phase, i.e., Intermetallic Compound (IMC). The formation of IMC in the stir zone can improve the mechanical properties of the weld joint. The appropriate dispersion and distribution of interlayer particles in the Al matrix lead to forming a strong metallurgical bond at the interface of interlayer particles and base metal.

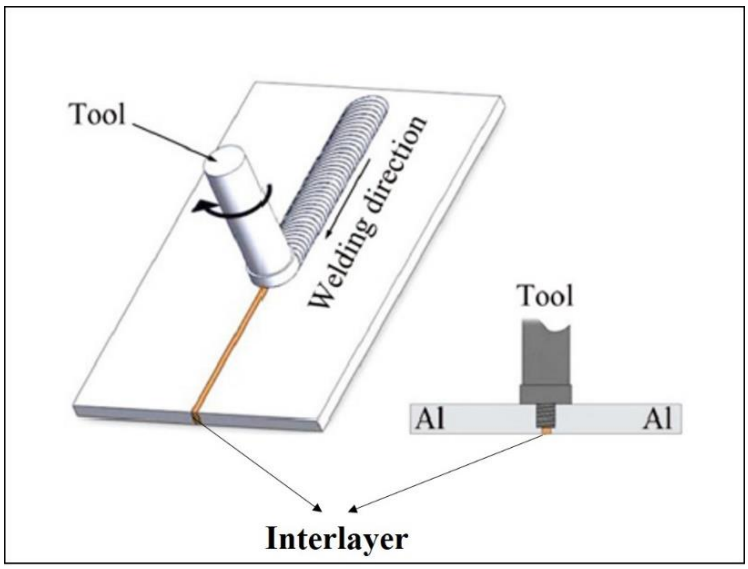

Figure 2.3 Schematic of FSW with interlayer. (Khojastehnezhad et al. 2018)

Wilson et al. (2016) studied the effect of Zn interlayer of varying thicknesses (5 µm, 10 µm, 20 µm, 50 µm, and 100 µm) on FSW of AA7020 alloy. They studied the distribution of interlayer particles in weld with scanning electron microscope (SEM) images and observed that

10 μm interlayer particles dispersed uniformly in the SZ, as displayed in **Figure 2.4.** The uniform distribution of interlayer reduced thermal softening and attained enhanced strength and hardness. In addition, the respective microstructures exhibited fine grains. This will increase joint strength and stop the growth of cracks.

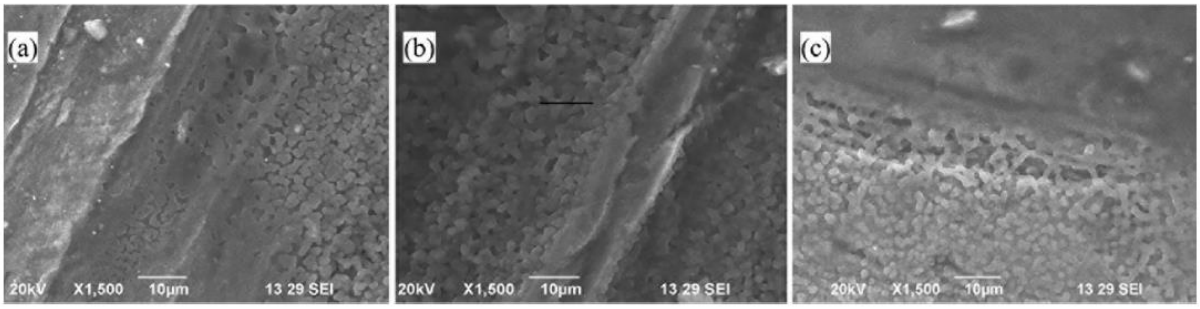

Figure 2.4 SEM images of (a) AS, (b) SZ, and (c) RS of the weld joint with 10 μm Zn interlayer (Wilson et al. 2016)

Khojastehnezhad et al. (2018) Conducted FSW on AA6061 alloy with copper as interlayer and observed the improvement in mechanical properties with the insertion of Cu interlayer between the weld plates. The refined Cu particles and fragments were dispersed throughout the Al matrix, forming a composite-like structure. The diffusion of Cu particles into the Al matrix serves as a precipitation-based strengthening process. Interfacial diffusion and interaction between the two materials resulted in the formation of Al/Cu IMCs in this zone, as shown in **Figure 2.5**. In the stir zone of joint, results indicate the existence of Al and Cu elements and development of IMCs or reaction layers such as Al_4Cu_9 and Al_2Cu.

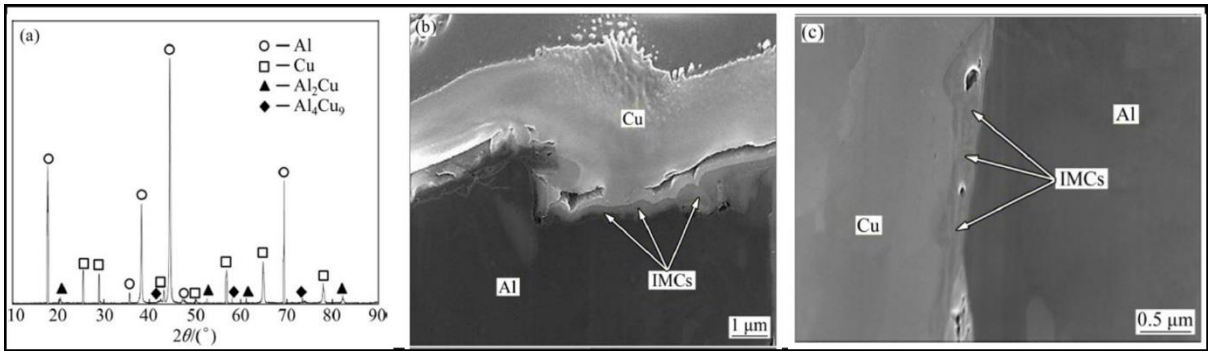

Figure 2.5 (a) XRD pattern of weld with Cu interlayer, (b) and (c) SEM images of IMCs formed at the interface (Khojastehnezhad et al. 2018)

The lower and middle regions of the stir zone have higher hardness values than the top region due to the creation of IMCs and the intensive stirring action of the tool pin, which led to the recrystallization of grains **(Figure 2.6)**. In addition, the ultimate tensile strength of the joint

with copper plate was 285 MPa, showing that 89.1 % of the Al base metal was utilized. In contrast, the tensile strength of the joint welded without Cu insert was 218 MPa with 73.5 % joint efficiency.

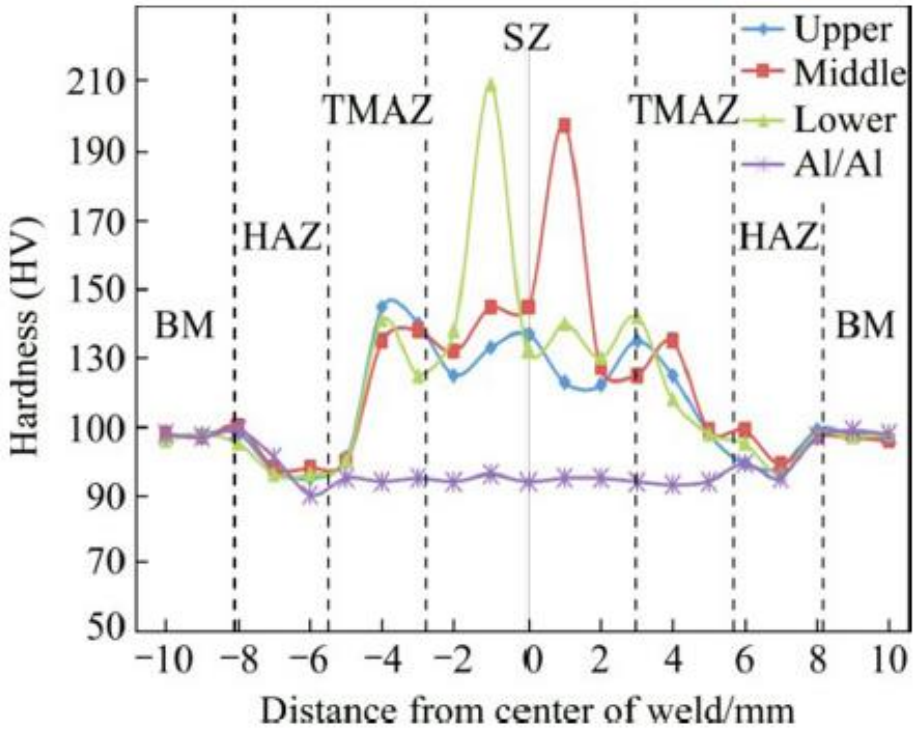

Figure 2.6 Hardness profiles of weld with and without Cu interlayer (Khojastehnezhad et al. 2018)

Mokabberi et al. (2018) studied the effect of different interlayers (Cu, Zn and brass) on the FSW of pure Al alloy. The Zn interlayer was shattered into small fragments and some of them were dissolved and diffused to form an Al-Zn solid solution within the weld. The major difference was the presence of large unreacted Cu particles broken from the Cu interlayer and distributed throughout the aluminium matrix. Compared to the Cu interlayer, the superior dispersion of the brass interlayer inside the stir zone and the comparatively complete reaction of brass particles with aluminium result in a strengthening IMCs. The greater the volume fraction of IMCs, the greater the weld joint hardness. While Zn and Cu interlayers had no noticeable influence on joint efficiency (60 % and 50 %, respectively), brass interlayer application improved joint efficiency to 90 % **(Figure 2.7)**. The researchers suggested that using Zn and Cu interlayer was ineffective for reducing the weld metal softening. In the case of the zinc interlayer, Zn atoms were dissolved in the aluminium matrix to create a solid solution, and no intermetallic compound was found within the stir zone. As indicated

previously, the brass interlayer was better fractured and disseminated throughout the stir zone than the copper interlayer, and Al_2Cu and Al_4Cu_9 intermetallic compounds were produced. These factors resulted in the formation of a composite structure with enhanced strength.

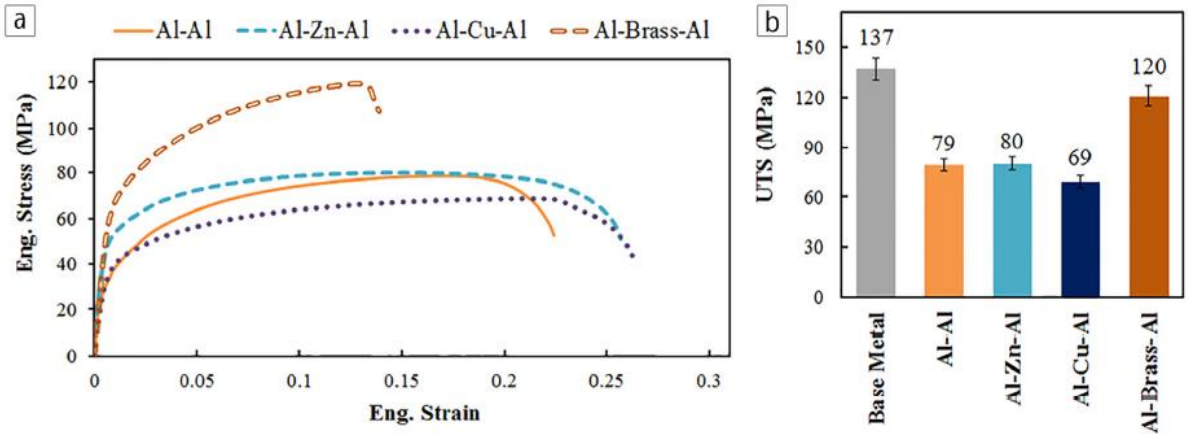

Figure 2.7 (a) Stress-strain curves and (b) UTS obtained from the longitudinal tensile tests. (Mokabberi et al. 2018)

2.4 Effect of cooling media and interlayer on mechanical properties of FSWed Al alloys.

Eventhough better joint properties are obtained with the use of interlayer compared to without interlayer, the formation of a brittle and high density of IMCs in the SZ is a major problem. The strength of FSWed joints with interlayers predominantly depends on the defects, microstructure, density, and thickness of IMCs (Mahto et al. 2021). The thin layered IMCs strengthen, while the thick IMCs generate cracks in the weld. Generally, IMCs rich-zone tends to crack easily, while tensile deformation is the primary cause of premature failure of dissimilar joints. The formation and growth of IMCs are influenced by peak temperature and cooling rate. In addition, the formation and growth of IMCs are determined by the constitutional liquation coupled with the mutual affinity of metals during the FSW process. Therefore, it is necessary to control the liquation and growth of IMCs during the welding process. Lowering the weld temperature and rapid cooling rate may help to reduce the amount of IMCs. This requires lowering the peak temperature to achieve an SZ temperature lower than the eutectic temperature (Mehta et al. 2019). Moreover, the different microstructural regions that evolved after FSW are SZ, Heat-Affected Zone (HAZ), and Thermo-Mechanically Affected Zone (TMAZ), in which more softening occurs in HAZ. Also, it is evident that HAZ is the weakest

region of the weld joint attributed to precipitates dissolution and grain coarsening. Improving the hardness of HAZ can enhance the strength of the overall joint.

Çam et al. (2014) The combined effect of interlayer and external cooling (chloraethyl cooling spray) was studied to improve the weld joint strength. From **Figure 2.8**, it is evident from the hardness profiles that the external cooling (i.e., cooling spray) applied did not appreciably increase the weld region's hardness. Although the strength of the nugget could be enhanced by using a stronger interlayer, a strength recovery was not possible in the HAZ due to insufficient external cooling. As evidenced by the hardness profiles of the joints, all specimens failed within the HAZ due to the occurrence of a minimum hardness in this region. Hence, the researchers suggested using proper external cooling to improve joint performance.

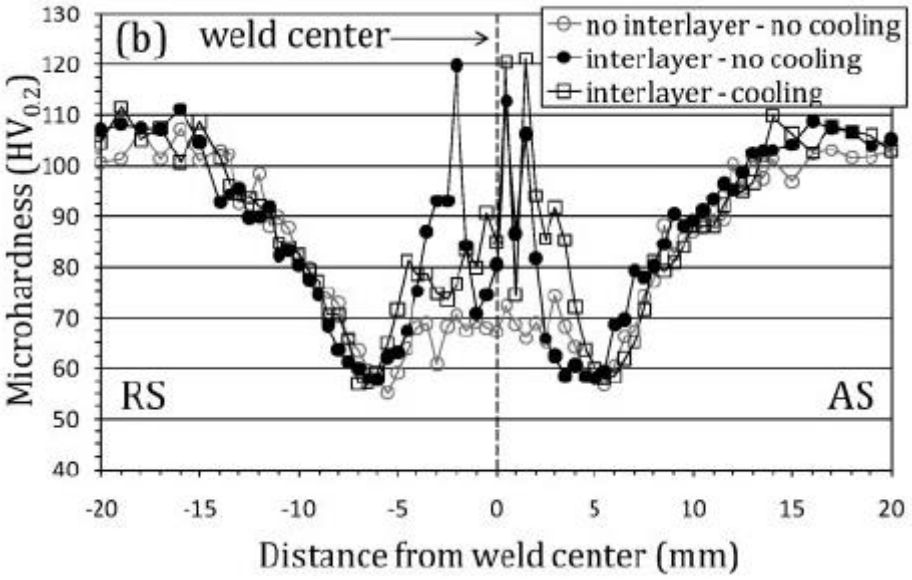

Figure 2.8 Hardness profile across the cross-section of the joint. (Çam et al. 2014)

However, the main objective was to prevent the formation of brittle IMCs and minimize the volume fraction of IMCs, dissolution of precipitate, and grain coarsening in HAZ to get the overall joint quality. The factors mentioned above can be controlled by changing the thermal cycles and rapid cooling during FSW, which can be achieved when FSW is carried out in a water environment. The variation to the existing FSW process is named underwater FSW. However, the heat supply should not be inadequate, as insufficient heat input may result in an improper weld joint. Essentially, welding is performed underwater, either in a bath or in a condition where fluid continuously flows across the weld surface. This process is well suited for alloys susceptible to thermal heat during welding. The FSW performed in underwater

cooling accelerates the heat dissipation and acts as a barrier against precipitates dissolution and grain growth, yielding more refined grains to improve the weld strength (Mofid et al. 2012).

Zhang et al. (2012) studied the effect of underwater FSW on Al-Cu dissimilar weld to improve the hardness in HAZ. During the ageing process of precipitate-hardened aluminium alloys, it is known that a precipitate-free zone (PFZ) tends to develop along the grain boundaries **(Figure 2.9(a)**. During FSW, the HAZ precipitates are coarsened relative to the BM **(Figure 2.9(b))**. The expansion of PFZ is due to the depletion of a large number of solute atoms caused by coarsening of precipitates near the grain boundaries. The narrower PFZ of the underwater HAZ (UHAZ), compared to the normal HAZ (NHAZ), can be attributable to the lower amount of precipitate coarsening. They observed that precipitate coarsening was lowered using water cooling. The PFZ had become narrow **(Figure 2.9(c))** due to a faster cooling rate, resulting in improved hardness in the HAZ region.

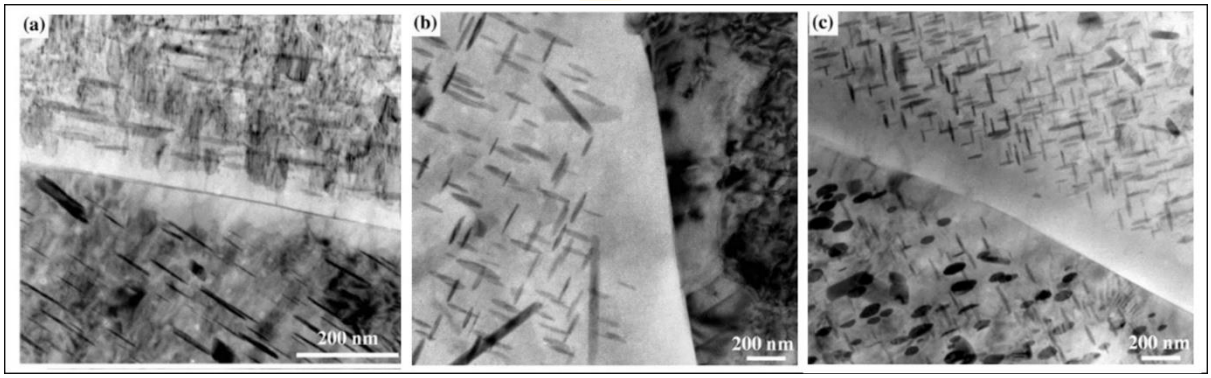

Figure 2.9 The precipitate-free zones of (a) BM, (b) NHAZ, and (c) UHAZ. (Zhang et al. 2012)

The hybrid approach of cooling and heating assisted FSW of Al-Cu joints was carried out by (Mehta et al. 2017). They observed that preheating the base plates before FSW increased the formation of a high density of IMCs in SZ, deteriorating the mechanical properties. However, in the case of cooling-assisted FSW, the IMCs formation was inhibited and improved tensile strength and hardness of the weld. Abdollahzadeh et al. (2021) studied the effect of underwater FSW on AA6061-T6 alloy to enhance the mechanical properties of the weld. They concluded that underwater FSW improved the hardness of HAZ, enhancing the strength and impact toughness. The enhancement in mechanical properties was attributed to more grain refinement and lower dissolution of secondary precipitates in the SZ. Therefore, due to control of the thermal cycle and faster cooling rate using water as cooling media in FSWed dissimilar

materials, the researchers observed suppression in the formation of IMCs. Consequently, the mechanical properties were enhanced compared to air cooling.

2.5 Effect of interlayer on corrosion behaviour

Generally, the life of the weld joint depends on corrosion resistance and these joints are corroded when exposed to the corrosive environment or chemical solution. Although AA6061-T6 has good corrosion resistance in an open environment, it is necessary to study the corrosion behaviour of the weld joints with and without interlayer in a corrosive environment.

Shamsipur et al. (2018) studied the effect of Zn foil on corrosion behaviour of FSWed Al-Mg alloy using various tool rotational and traverse speeds. The effect of Zn foil addition on the corrosion behaviour of welds was investigated using a cyclic polarization test. The potential value of weld with Zn foil (F1) is less than without foil (S2), indicating that better corrosion resistance was obtained using Zn foil, as shown in **Figure 2.10**. It has been reported that FSW has a localized heterogeneous microstructure, making welded materials prone to corrosion. Moreover, apart from adding Zn foil, welding conditions such as traveling and rotational speeds significantly define corrosion properties. They reported that defect-free joints were obtained at optimized process parameters due to the proper distribution of Zn particles in the stir zone, resulting in improved corrosion resistance.

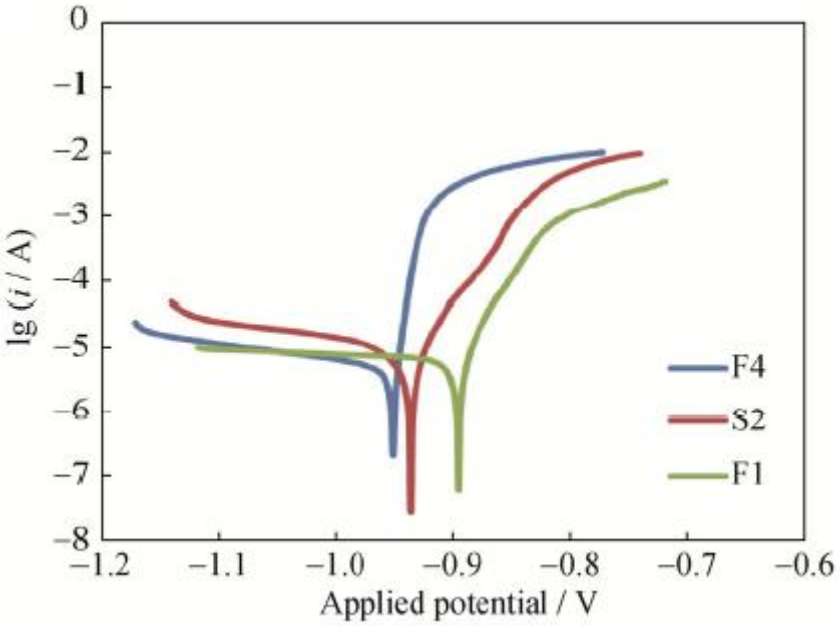

Figure 2.10 Polarization curves of stir zone in three different joints (Shamsipur et al. 2018)

Generally, the corrosion behaviour of FSWed dissimilar alloys depends on the distribution and size of IMCs and the number of second phase particles. The formation of many IMCs increases structural inhomogeneity, making the structure susceptible to corrosion, mainly in chlorine environments. The size and distribution of precipitates/IMCs can be controlled using external cooling to enhance the corrosion resistance of the weld.

Few researchers studied the water-cooling effect on precipitates and their effect on corrosion behaviour. Wang et al. (2015) investigated the effect of underwater FSW on corrosion behaviour of AA7055 alloy. They found that the formation of $MgCu_2$ precipitates was inhibited with water cooling, which improved the corrosion resistance of the weld. Sinhmar et al. (2017) studied the effect of water cooling on mechanical properties and corrosion behaviour of FSWed AA2014 alloy and stated that the width of HAZ was reduced and HAZ hardness was improved due to a faster cooling rate. They also stated that water cooling reduced the discontinuity and size of strengthening precipitates, thereby improving the corrosion resistance of the weld.

2.6 Effect of reinforcement on damping behaviour of FSWed Al alloys

A material's damping is its capacity to absorb energy when subjected to cyclic loads. Cyclic loading creates vibrations and sounds, which materials can suppress with a high damping capacity. Given the growing requirement for vibration and noise reduction in contemporary industries, damping capacity is attracting much attention. The well-known aluminium alloys have many applications in the aerospace and automobile industries, but the damping capacity is very low. However, composite fabricated by incorporating reinforcement particles that possess high damping properties in the Al matrix makes it possible to enhance the damping capacity (Singh et al. 2017). The undesirable IMCs can be prevented, when metal matrix composites (MMCs) synthesized near room temperature or at least in the solid state. Solid-state fabrication of MMC is achievable with the help of FSW, an appropriate and effective approach (Siva Prasad et al. 2015). Few researchers attempted to improve the Al alloys damping using friction stir processing (FSP) and reinforcement particles such as graphite, SiC, and MgO and observed the enhancement of damping capacity.

Venkateswara Reddy et al. (2020) Studied the damping behaviour of composite fabricated through FSP of AA6061 using graphite as reinforcement particles. As per frequency-dependent damping studies (**Figure 2.11(a)**), the damping capacity of the base metal was 1.1×10^{-3} at 1 Hz, indicating poor damping. After FSP and adding up to 10 vol % graphite, the damping has increased marginally. The addition of 15 % graphite, however, greatly enhanced the damping.

Moreover, 15 vol % graphite-containing composites exhibited the highest temperature-dependent damping capacity at 250° C, which is 3.25 times the as-received alloy (**Figure 2.11(b)**). The increased damping after FSP is attributed to the grain size decrease or grain boundary area increase. Graphite has a simple hexagonal structure with basal planes that are weakly bonded along [0001]. The free movement of basal planes under vibrations greatly improves damping, enhancing the inherent damping of composites. As a result, the addition of graphite has improved the inherent damping capability of composites while also increasing grain boundary area. At high temperatures, the grain boundaries have viscous characteristics. Moving grain boundaries dissipates energy caused by dynamic or cyclic stress. The observed trends, such as increased damping capacity and damping slope change with temperature, can be attributed to microstructure refinement during FSP.

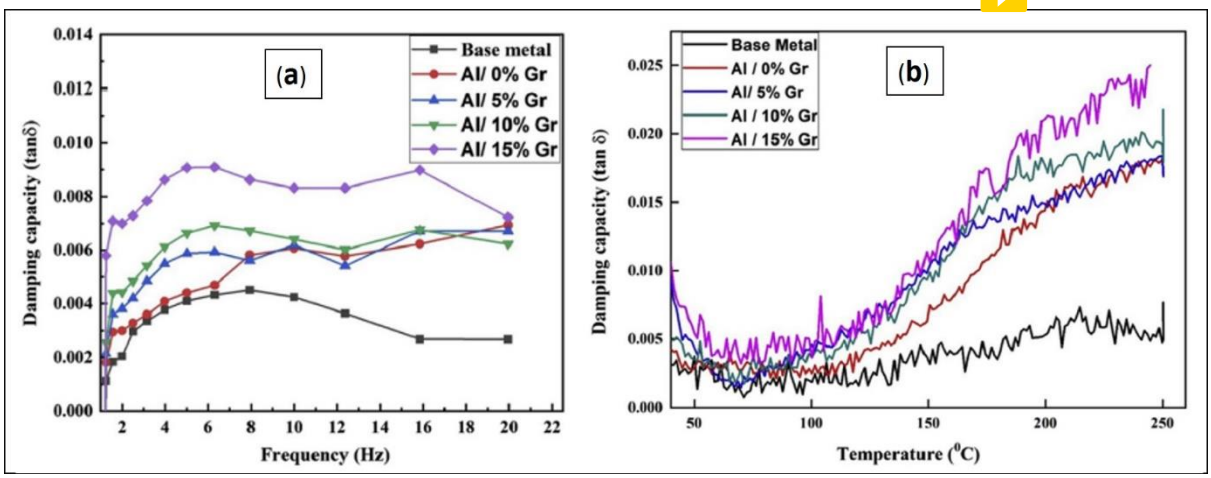

Figure 2.11 (a) Frequency-dependent and (b) Temperature-dependent damping capacity. (Venkateswara Reddy et al. 2020)

Reddy et al. (2022) investigated the effect of SiC size on microstructure and damping behaviour of FSPed AA6061 alloy. They observed the grain refinement with increased grain boundary area and dislocation density with the addition of carbide particles. The 9 µm size SiC particles showed less grain size. In this study, the damping capability of the FSPed sample was lower than that of the base alloy, as shown in **Figure 2.12**. The reduced damping is due to a decrease in dislocation density following FSP. The damping capacity of FSPed alloy and composites was much better than that of the base metal. The high-temperature damping increased with SiC particle size once more attributed to the inherent damping capacity of carbide particles.

Jiang et al. (2017) investigated improving damping capacity while enhancing mechanical properties of FSPed Al-Mg-Si alloy. They observed that employing FSP resulted in

recrystallized fine grains with enhanced high angle grain boundaries with moderate strength and an undissolved meta-stable phase. They concluded that grain refinement is the significant factor that improved the damping capacity of FSPed alloy without sacrificing the mechanical properties (**Figure 2.13(a)**). During damping testing at high strain amplitudes, FSP samples developed a greater number of dislocations, resulting in an increase in damping capacity (**Figure 2.13(b)**).

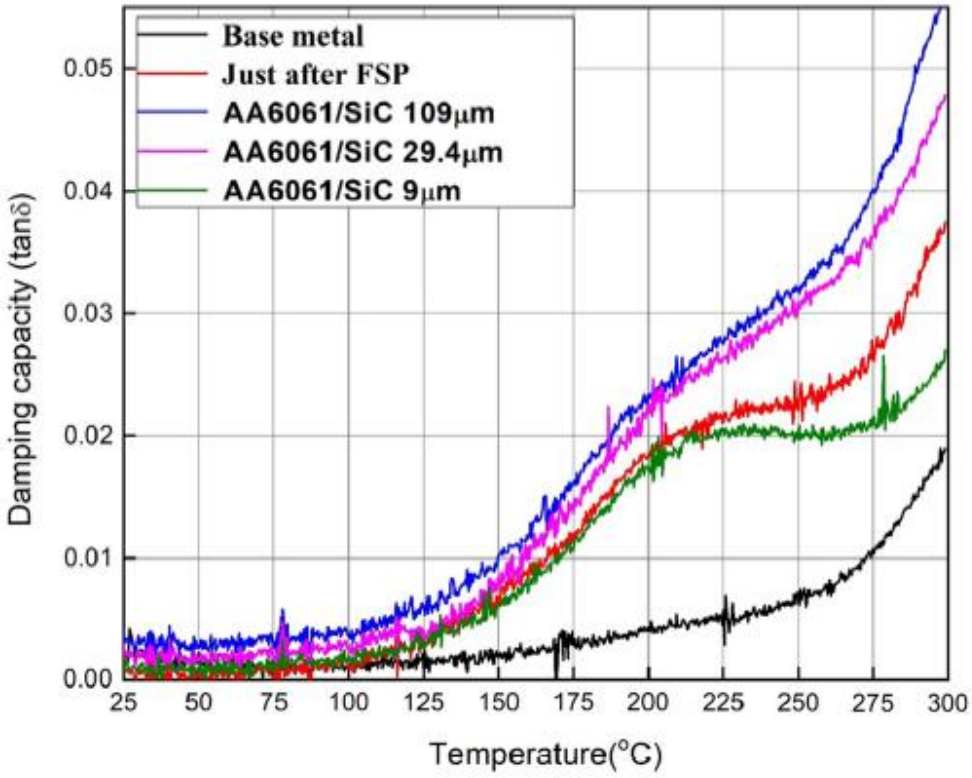

Figure 2.12 Damping capacity of BM and surface composites (Reddy et al. 2022)

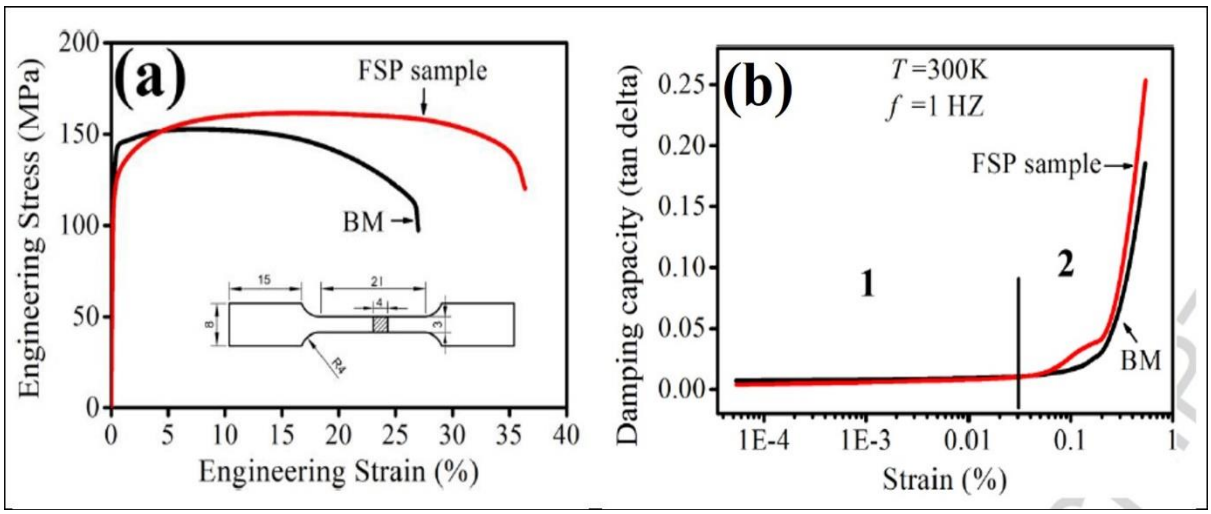

Figure 2.13 (a) Stress-strain curve (b) Damping behaviour (Jiang et al. 2017)

2.7 Effect of reinforcement on wear characteristics of FSWed Al alloys

The exceptional qualities of aluminium and its alloys, such as high specific strength, strong stiffness, and excellent formability, support their widespread use in aircraft, petrochemical, maritime, and automotive application etc. However, both pure aluminium and aluminium alloys have low hardness and poor abrasion resistance, limiting their possible applications. Therefore, enhancing Al-alloys hardness and wear resistance is a crucial step toward expanding their applications. The decrease in hardness due to thermal softening after FSW result in a reduction of wear resistance. Since hardness and wear resistance are surface properties that depend on the microstructure and composition of the near-surface region of a material, it will change the composition and microstructure of the surface without changing the bulk properties of Al alloys. This can help to preserve the ductility of the inner Al matrix while simultaneously enhancing the surface wear resistance (Miller et al. 2000). FSP can be used to include ceramic reinforcing particles into an aluminium matrix to provide exceptional wear resistance. The primary benefit of this approach is the preservation of bulk characteristics (Hanzaki et al. 2011).

Recently, Alishavandi et al. (2020) studied the surface nanocomposite wear characteristics of AA1050/mixed metal oxides (MMO) produced by FSP. The 6 pass FSP with the addition of particles (6PPA) and without particles (6PA) was performed. The weight loss in BM samples is much higher than in FSPed samples, and the resistance in both 6PA and 6PPA samples is the same at first. But the 6PA sample loses more weight than the 6PPA sample when it slides farther **(Figure 2.14(b))**.

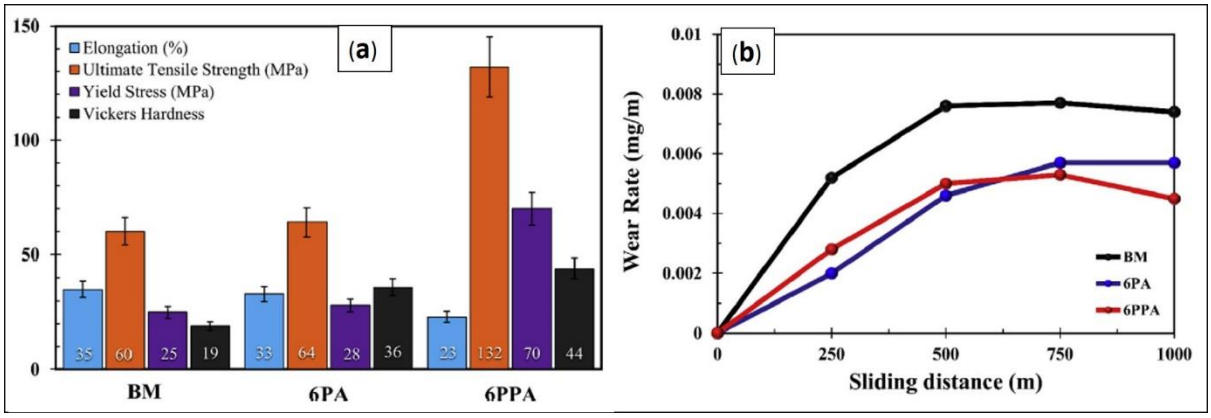

Figure 2.14 (a) Mechanical properties of FSWed joints and (b) Wear rate vs sliding distance (Alishavandi et al. 2020)

The grain structure of the 6PPA sample has become more refined, and this has caused the surface to become harder. The results also showed that adding MMO nanoparticles strongly affects lowering aluminum alloy's wear rate. The uniform distribution of particles throughout the stir zone resulted in increased tensile strength and wear resistance **(Figure 2.14(a))**.

Huang et al. (2018) investigated the influence of Cu powder addition on microstructure, mechanical, and wear behaviour of FSPed pure Al alloy. FSP achieved a more uniform particle distribution (**Figure 2.15(a)**) with virtually no particle clustering. This is mostly owing to the repetitive stirring action, temperature exposure, and plastic deformation, which shattered particle clusters into finer particles and dispersed them more equally throughout the Al matrix.

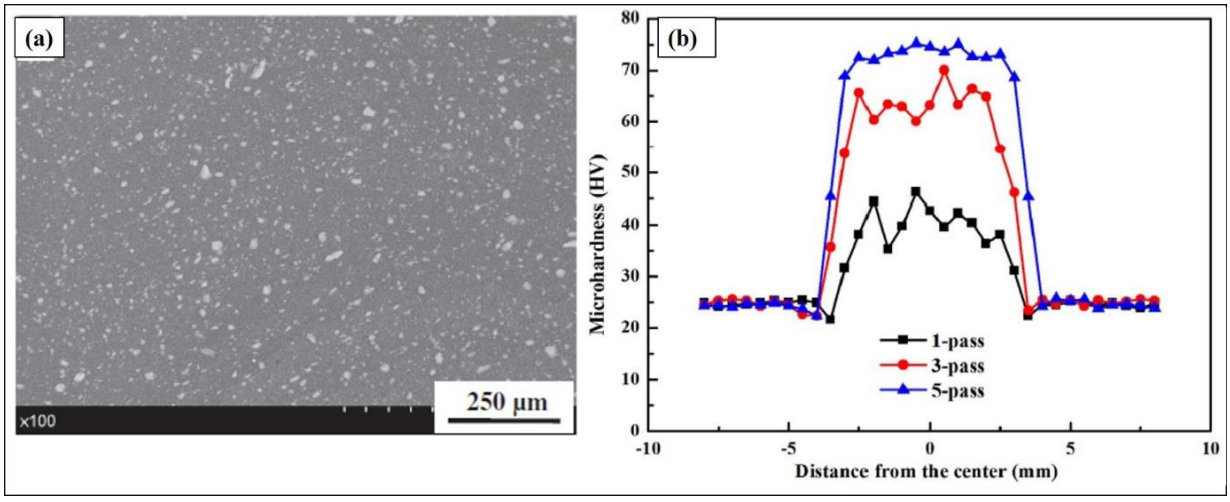

Figure 2.15 (a) BSE micrographs demonstrating the dispersion of reinforcing particles within FSPed AMC layers after 5 passes and (b) Microhardness profile.

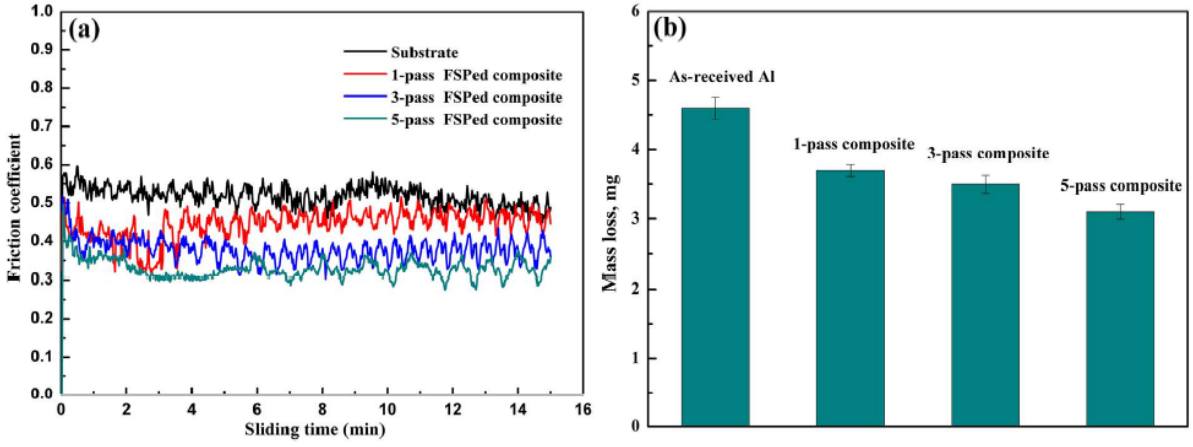

Figure 2.16 (a) Variation of coefficient of friction and (b) Weight loss of weld samples. (Huang et al. 2018)

According to **(Figure 2.15(b))**, as the number of FSP passes increases, the hardness values in FSPed AMC layers decrease, and the hardness values increase. This results from forming finer Al_2Cu particles and their better distribution in higher FSP pass. The 5-pass FSPed composite layer has the lowest friction coefficient and weight loss **(Figure 2.16(a))**, demonstrating its superior resistance to friction and wear, as shown in **Figure 2.16(b)**. The friction test results are consistent with the microhardness test results, and their causes may be identical.

Mehta et al. (2019) studied the effect of B_4C particle addition on the wear behaviour of FSPed AA6061 alloy. They observed that the homogenous distribution of ceramic particles improved the wear resistance compared to the base metal. They concluded that reversing the direction of processing passes increases the homogeneity of the reinforcement particle distribution. In terms of fabrication, reversing the direction of processing passes is incredibly straightforward and economical.

Narimani et al. (2016) investigated on mono and hybrid composite fabricated through FSP using B_4C and TiB_2. They observed incorporating B_4C and TiB_2 reinforcing particles into the surface-enhanced composite layers' hardness and wear resistance compared to FSPed AA6063 alloy without reinforcement. The researchers concluded that the surface composite layer of 100 % TiB_2 displayed the highest hardness and wear resistance compared to other fractions.

2.8 Effect of interlayer on fatigue behaviour

The weldments utilized in transportation are susceptible to failure under impact and cyclic loading situations. Thus, it is essential to analyze the impact property and fatigue crack growth (FCG) behaviour of the weldment to prevent mishaps. The fatigue life is assumed to be primarily determined by welding flaws, microstructure, and residual stress (Threadgill et al. 2013). Without thoroughly examining these three aspects and their relationships, it is difficult to conclude fatigue behaviour. It is common knowledge that fine-grain microstructures have superior mechanical characteristics.

Hassanifard et al. (2021) investigated on effect of Cu foil on fatigue response of FSWed AA6061 alloy. The weld was carried out using two different thicknesses of interlayer F1 (100 µm) and F2 (200 µm) and without foil (WF). Copper foils utilized in welded joints enhanced both tensile strengths and elongations. The weld joint with F1 foil has shown higher strength than the remaining weld joints (**Figure 2.17(a)**). Even though joint sample F2 comprised a 200 µm-thick copper sheet, its tensile strength did not increase significantly. This is due to the copper substance's limited solubility in aluminium. Copper produces layers above this limit,

resulting in decreased strength when loaded. In both high-cycle and low-cycle fatigue regimes, the presence of Cu foils in the stir zone enhanced fatigue lives. Joint samples of F1 foil had a slightly higher fatigue strength than joint samples of F2 foil (**Figure 2.17(b)**). They suggested that microscopic analysis should be carried out to analyze the improvement in fatigue life with interlayer.

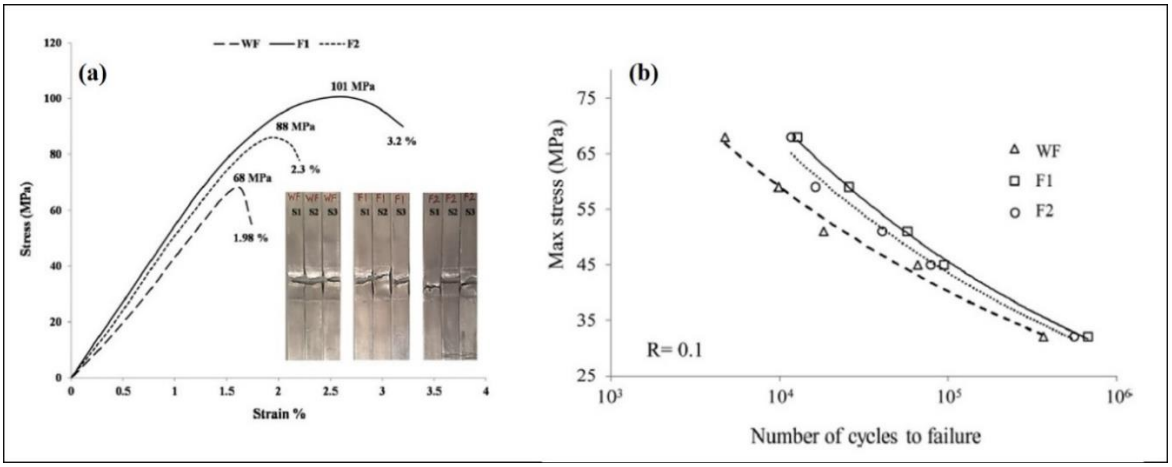

Figure 2.17 (a) Stress-strain curves and (b) S-N curves of weld samples (Hassanifard et al. 2021)

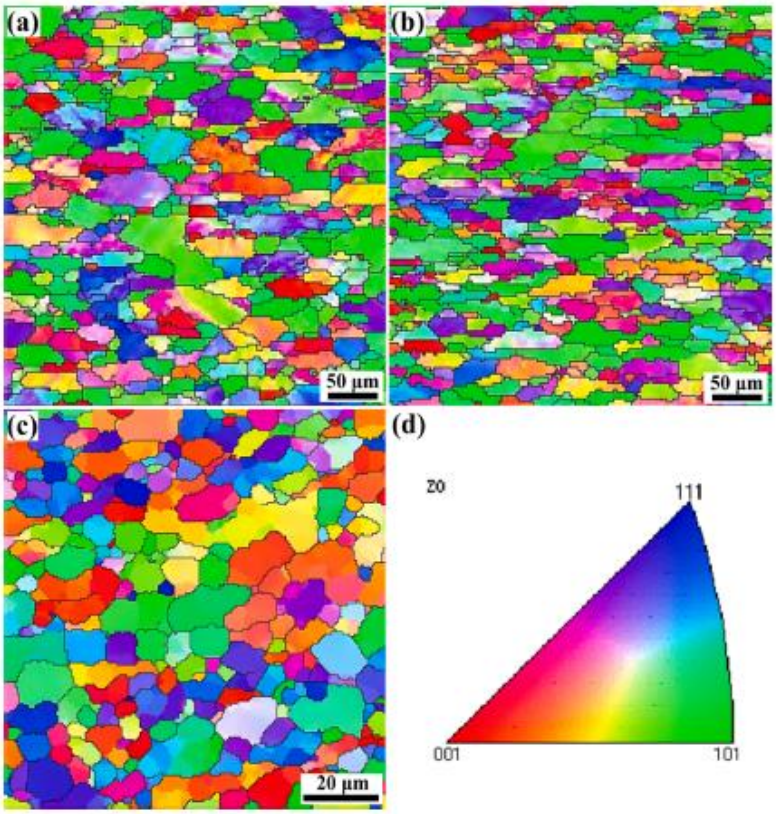

Figure 2.18 The inverse pole figure in the Z direction of (a) BM, (b) HAZ and (c) WNZ, and (d) key for the IPF map (Zhang et al. 2020)

Zhang et al. (2020) conducted FSW on 6061 Al alloy to study the influence of microstructure and precipitates behaviour on fatigue crack growth behaviour. Generally, fine grains with high grain boundaries (HABs) obstruct crack propagation, enhancing fatigue life. The stir zone has shown equiaxed, fine grains than the remaining zones (BM and HAZ), as shown in **Figure 2.18**. However, the proportion of low angle grain boundaries (LABs) in the three zones displayed an inverse relationship; the proportion of LABs rapidly declined from BM to HAZ and weld nugget zone (WNZ).

As shown in **Figure 2.19**, the FCG rate increased as number of ccycles (N) increased, and the fatigue life of compact tensile (CT)-BM was less than that of CT-HAZ and CT-WNZ, showing that the weld joint stopped the fatigue crack from growing attributed to the grain refinement factor. In addition, the a-N curves of CT-BM and CT-HAZ were smooth and continuous, whereas the crack size (a)-N curve of CT-WNZ displayed an evident fluctuation.

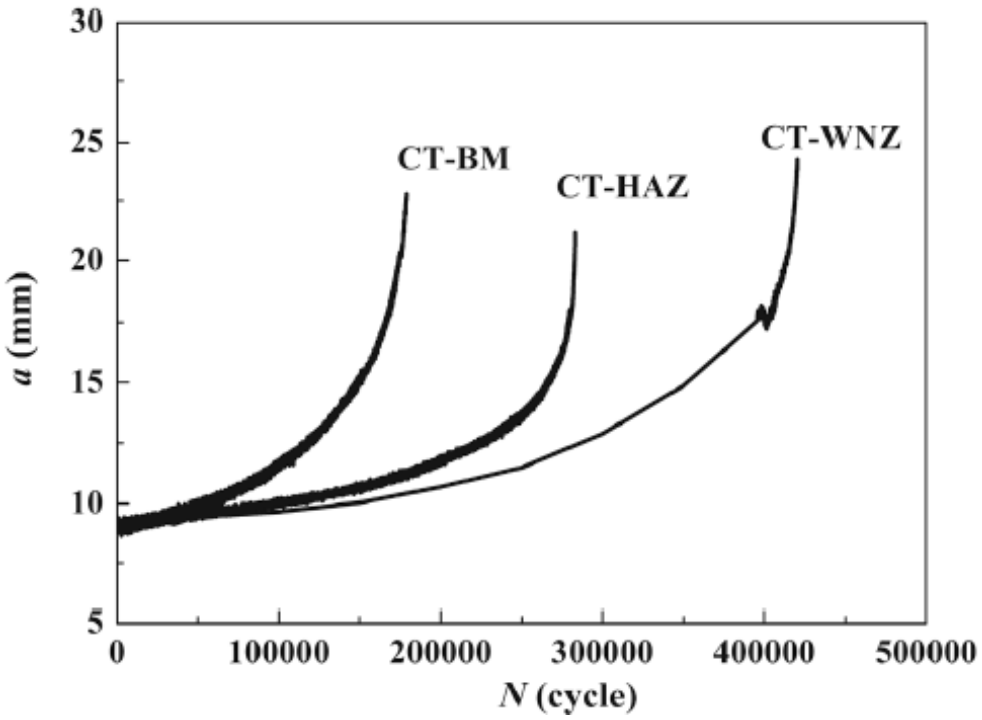

Figure 2.19 The relationship between fatigue crack length a and cycle index N (Zhang et al. 2020)

Vysotskiy et al. (2019) investigated on fatigue behaviour of FSWed AA6061 alloy. They optimized the process parameters to get optimum fatigue life. The better fatigue performance of the improved welds was comparable or even superior to that of the base material. This result was attributable to substantial grain refinement in the stir zone, a slight material softening in the heat-affected zone, and substantial residual stress generated during FSW.

2.9 Summary and Literature gaps

From the literature review, it was observed that a considerable amount of work was carried out to enhance the mechanical properties of FSWed Al alloy using different interlayers. The combined effect of interlayer and cooling media on microstructure and mechanical properties is very scary. Moreover, the influence of a high damping interlayer on damping capacity was not yet studied. In addition, the following literature gaps have been observed across the overall literature:

1. Very few research has been carried out on the FSW of AA6061-T6 using interlayers to improve the weld strength.

2. Few works of literature are available on the combined effect of cooling media and interlayer on the FSW of aluminium alloys.

3. Few kinds of literature are available on the effect of interlayer on corrosion, wear and damping behaviour of weld joints.

4. Limited research has been carried out on the effect of interlayer on Fatigue behaviour of weld joints.

CHAPTER 3

EXPERIMENTAL PROCEDURES

3.1 Introduction

This chapter describes the experimental methodologies used to join and characterize the microstructure, mechanical, and corrosion parameters stated in the study's results section. Since most of the strategies are well-known, they will be explained briefly.

The friction stir welding (FSW) machine was used in the present work to join AA6061 alloy with interlayer. Three different tools were used with varying rotational speeds, and the tool transverse speed was kept constant. After obtaining optimum process parameters conditions, the weld was performed underwater. Microstructure, mechanical properties, corrosion behaviour, damping characteristics, wear analysis, and fatigue behaviour were studied for both natural and water cooling weld joints welded with and without interlayer.

3.2 Experimental procedure

The overall work plan is outlined in **Figure 3.1**. Initially, FSW is carried out on weld with brass interlayer by optimizing the FSW process parameters such as tool rotational speed and traverse speed to get a defect-free joint. All these processes are performed in natural cooling (NCFSW). Water-cooling FSW (WCFSW) is performed to get a better metallurgical bond between brass particles and Al matrix and investigate welds' microstructure, mechanical properties, and corrosion behaviour with and without interlayer. A damping test was performed for natural cooled and water-cooled welds with and without interlayer to determine composites' damping capacity. A wear test is carried out on all samples to study interlayer particles' influence on friction coefficient and wear rate. Finally, the fatigue behaviour was studied for all the samples to determine the impact of intermetallic formation on fatigue life.

3.3 Selection of base material and interlayer material

A cold-rolled 6 mm thick AA6061-T6 plates were considered as base material (BM) for the present study. Base metal was sectioned into 280 mm x 70 mm x 6 mm plates for FSW and was butt joined along the rolling direction using a numerically controlled FSW machine. The chemical composition of base metal (BM) is presented in **Table 3.1**.

The brass interlayer (58% Cu and 36% Zn) of thickness 200 µm was selected in this study to obtain the proper dispersion and diffusion of interlayer particles in the aluminium matrix and achieve a defect-free joint that plays a vital role in the weld joint strength. The insertion of a low melting point interlayer melts at FSW process temperature and dissolves in the SZ efficiently. The insertion of a high melting point interlayer cannot react and form the adverse IMCs with the Al matrix. Various researchers (Wilson et al. 2016), (Shamsipur et al. 2018) also investigated interlayer thicknesses to get the proper dispersion and improved mechanical properties. They have suggested that optimum thickness (~200µm) of interlayer forms a good metallurgical bond with Al matrix, which enhances mechanical properties.

Table 3.1 AA6061-T6 alloy chemical composition (wt %)

Mg	Si	Cr	Mn	Fe	Cu	Ti	Zn	Al
0.79	0.83	0.06	0.04	0.21	0.22	0.03	0.02	Bal.

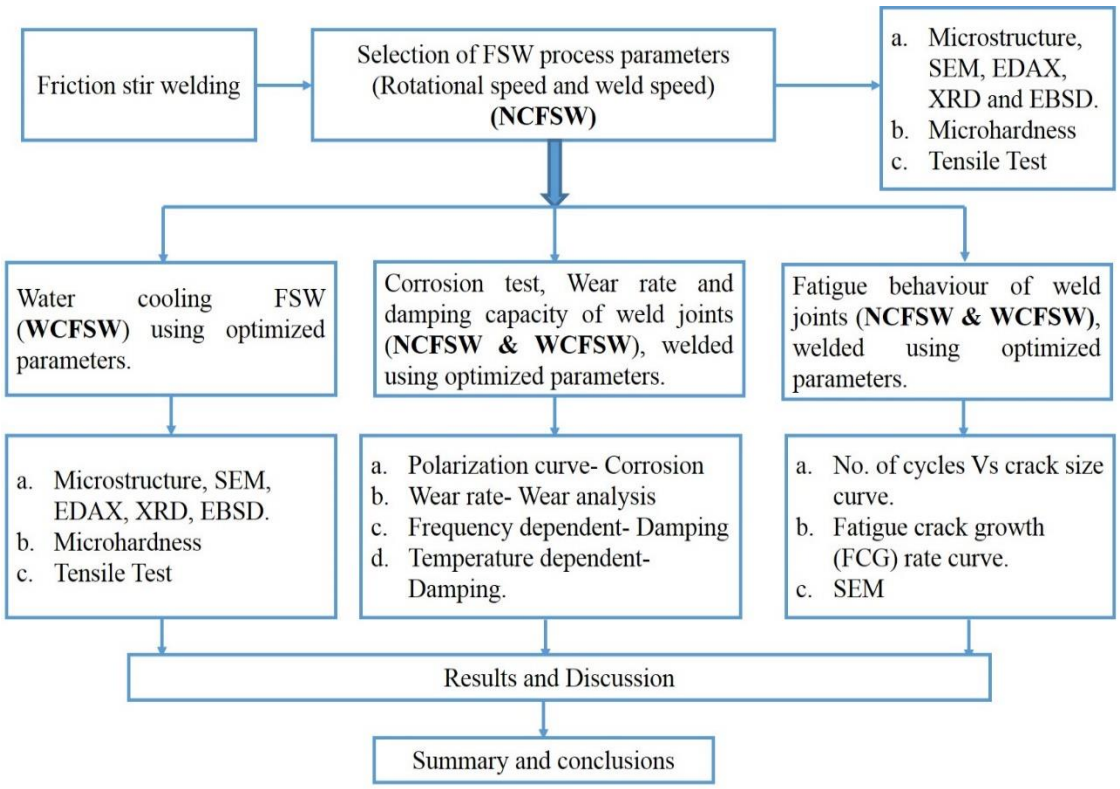

Figure 3.1 Work plan outline

3.4 Selection of tool material and tool design

FSW is a thermomechanical deformation process in which the tool temperature approaches the solidus temperature of the workpiece. The appropriate tool material must be selected for the intended application to produce a high-quality friction stir zone. In this study, tool steel AISI

H13 was employed for the experiments. This is due to tool steel's high-temperature strength and stability, its wear resistance, thermal fatigue strength, ease of friction stirring, machinability, and low cost. The chemical composition of the H13 tool material is listed in **Table 3.2**.

Table 3.2 Chemical composition (wt %) of AISI H13 tool steel

P	S	C	Mn	Si	V	Mo	Cr
0.02	0.021	0.4	0.46	1.06	1.10	1.31	5.3

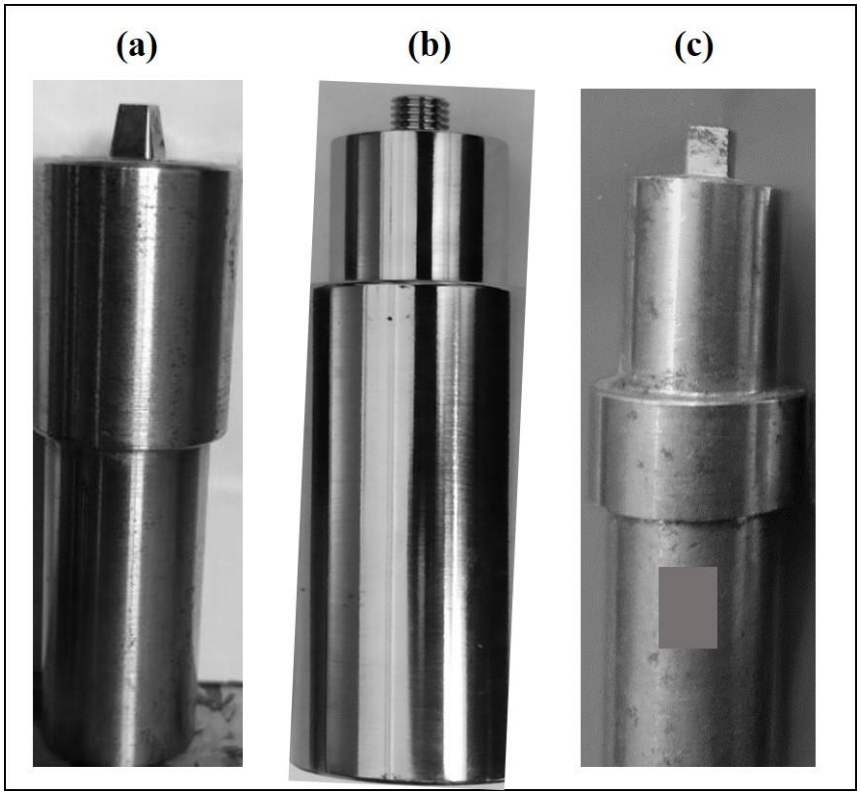

Figure 3.2 Tools used in this study (a) Square tapered tool, (b) Cylindrical threaded tool, and (c) Triangular tool.

Initially, trial experiments were carried out using a square tapered tool **(Figure 3.2(a))**, and the results were analyzed. The distribution of large brass particles is observed in the SZ. Therefore, a cylindrical threaded tool is used to optimize the FSW process parameters. The cylindrical threaded tool pin profile **(Figure 3.2(b))** allows scratching and mixing brass particles into the Al matrix from top to bottom during FSW with interlayer. Once tool penetrates completely, the material at the bottom of pin and adjacent to the pin is forced into threads. Due to the stirring action of the pin, the material is forced to move along the helical-shaped threads. In other words, material is forced into the threads and moves from bottom to the top of the pin. This

action causes uniform material flow and gives good material mixing. Moreover, the weld was carried out with a triangular tool to find a better tool **(Figure 3.2(c))**.

3.5 Friction stir welding machine

The FSW experiments were conducted on a numerically controlled 3-Ton capacity FSW machine developed by R.V Machine Tools, Coimbatore, India, as shown in **Figure 3.3.** The essential components of the FSW machine include a spindle motor, servo motor, table with fixture, force and position controller, lubrication system, and data acquisition (DAQ) system. The specifications of the FSW machine are shown in **Table 3.3**.

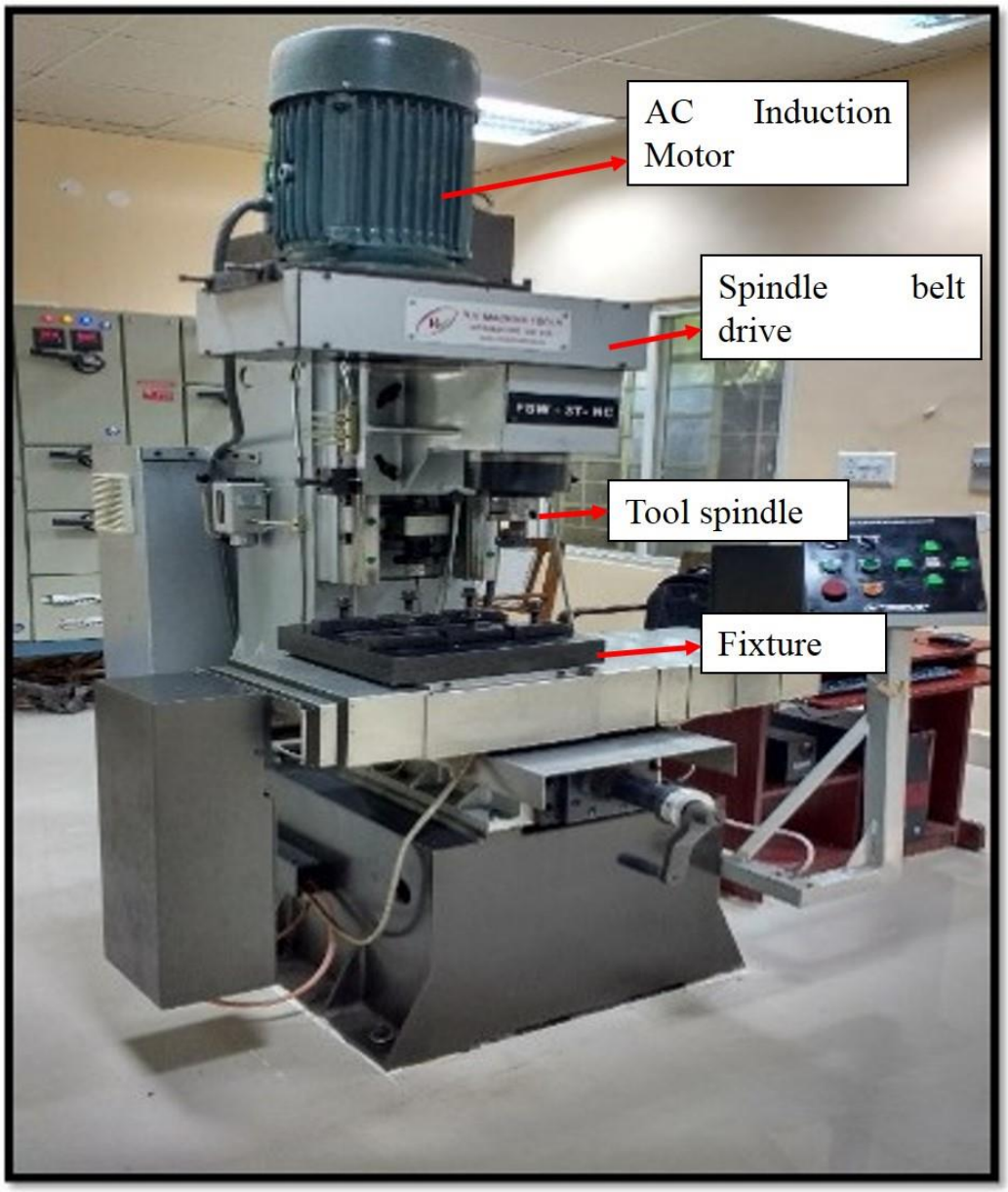

Figure 3.3 Friction stir welding machine

Table 3.3 Specifications of 3-Ton capacity FSW machine

S. No:	Details	Specifications	S. No:	Details	Specifications
1	Z-axis load	50 kN	11	Spindle motor	AC Induction motor 11kW/3-phase/1400rev/min/440V
2	Z-axis stroke length	300 mm	12	Tool holder	ISO 40 Arbor
3	Z-axis rate of movement	0-1000 mm/min	13	Mode of control	Position and force control
4	X-axis load	25 kN	14	Spindle head tilt	$\pm 5^{o}$ (Manual)
5	X-axis stroke length	400 mm	15	Machine size	1350x1750x2290 mm
6	X-axis rate of movement	0-1000 mm/min	16	Table size with thread holes	500x400 mm
7	Y-axis load	Manual	17	Load cell	X and Z-axis
8	Y-axis stroke length	200 mm	18	X-axis drive	Servo with gearbox
9	Lubricating system	Centralized and manual	19	DAQ & Analysis Software	Spindle speed, axis velocity against time, and force
10	Spindle speed	3000 rpm (Max)	20	Spindle torque	75 N-m @ 1400 rpm

H13 tool steel with cylindrical threaded pin profile is used as tool material, as shown in **Figure 3.4(a).** The brass interlayer was kept between the two weld plates, as shown in **Figure 3.4(b)** shows the schematic representation of FSW in **Figure 3.4(c)**. Before welding, the abutting edges of base plates were machined to produce a flat and smooth surface. The base plates and brass interlayer were cleaned with acetone to remove the contaminants and dirt.

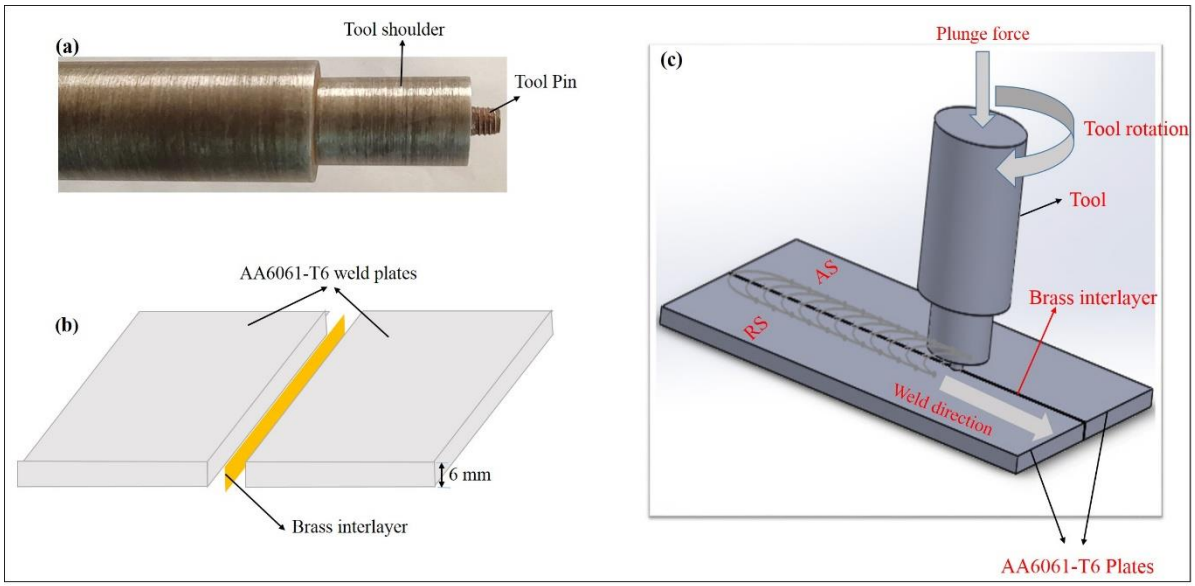

Figure 3.4 (a) Tool used, (b) and (c) Schematic representation of FSW with interlayer

3.5.1 Cooling environment condition

In order to study the heat effect on the formation of IMCs and precipitates and for comparison purposes, the weld was carried out in four phases. Weld without interlayer: natural and water cooling, Weld with interlayer: natural and water cooling. The natural and water-cooling FSW FSW with interlayer are shown in **Figures 3.5(a)** and **(b)**, respectively. The representation of the welding processes is followed as Natural Cooling FSW (NCFSW) and Water Cooling FSW (WCFSW). For NCFSW, no external cooling was used. However, for WCFSW, the weld plates are submerged in water, and welding was carried out with inflow and outflow to maintain the water at ambient conditions.

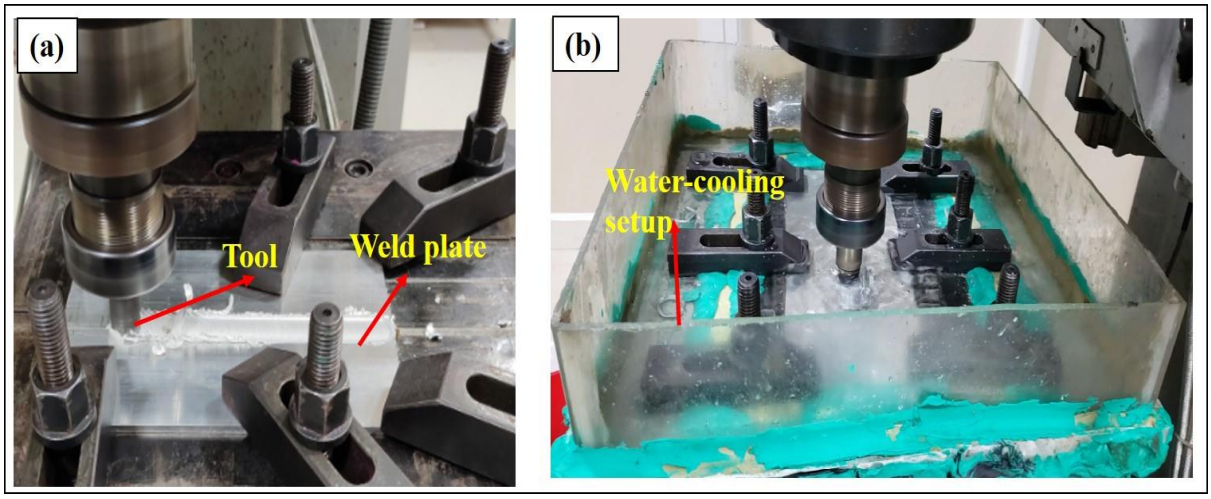

Figure 3.5 (a) Natural cooling FSW (NCFSW) and (b) Water-cooling FSW (WCFSW) setup.

3.6 Metallurgical analysis

3.6.1 Sample preparation

Samples for microstructure analysis were sectioned transversely to the welding direction with an abrasive diamond saw to the required dimensions. The samples were mounted in a hydraulic mounting press using bakelite powder for easy handling. The mounted samples were then polished with different grades of silicon carbide papers of 80, 120, 220, 400, 600, 800, 1000, 1200, 1500, and 2000 grit sizes, followed by disc polishing on velvet cloth using alumina suspension and diamond paste to get the mirror-like surface. After polishing, the samples were washed thoroughly with a water jet to remove the contaminants and dirt on the polished surface and then dried. The dried samples were then etched in a Keller's solution (190 ml distilled water, 5 ml HCL, 3 ml HNO3, and 2 ml HF) to reveal the grain morphology. The etching time of 150 s for AA6061 was optimized after a series of trials. After etching, the samples were kept under fully opened tap water to wash out the etchant present on the aluminium matrix. The etched samples were examined under different advanced metallurgical microscopes, including Optical Microscope (OM), Scanning Electron Microscope (SEM), and Electron Backscattered Diffraction (EBSD) along with X-ray diffraction (XRD) to reveal the various metallurgical features of friction welded samples.

3.6.2 3D Optical microscope

Figure 3.6 3D Optical microscope

The polished and etched weld cross-section samples were subjected to optical microscopy (OM) for macro-and microstructural characterization (Huvitz co Ltd, HRM300, South Korea). The study on the corroded surface was also conducted using OM. The optical microscope is depicted in **Figure 3.6**; its characteristics are listed in **Table 3.4**.

Table 3.4 Specifications of 3D Optical microscopy

S. No	Detail	Specification
1	Eye piece	10x Wide Field, Diapter Adjustable
2	Observation Tube	Trinocular Erect
3	Mountable Objective Lens	Plan Flour EPI 5X, 10X, 20X, 50X and 100X
4	Accuracy and repeatability	Accuracy of Magnification ± 15 - ±20 μm, Repeatability of magnification ± 10 - ± 15 μm
5	Lump Halogen	12 V, 100 W halogen Lamp
6	camera	Image Sensor, ½ inch, 3 megapixels
7	Illumination	Reflected bright field/dark filed/polarized
8	Filter	Neutral Density Filter Differential Interference contrast filter
9	Focussing unit	Stroke 30-45 mm, Resolution 0.01-0.05 μm, maximum sample height 15—25 mm.
10	3D Imaging and measurement	Panasis professional software

3.6.3 Scanning Electron Microscope

The VEGA 3 LMU model (developed by Tescon, Czech Republic) high-resolution scanning electron microscope with energy dispersive spectroscopy (EDS) feature was used to examine the intermetallics, precipitation phenomenon, fracture morphology, and corroded surface morphology of friction stir welded samples to propose the precipitate phases and intermetallics behaviour based on their chemical composition. **Figure 3.7** illustrates an image of SEM.

3.6.4 X-ray diffraction

The precipitate phases revealed by SEM investigation were confirmed using 'CuKα' radiation-assisted XRD. The stir zone of friction stir welded materials were analyzed using XPERT PRO model (Make: PANalytical, Netherlands) XRD equipment. **Figure 3.8** illustrates the image of X-ray diffraction. Utilizing X'Pert High Score software, the XRD results were analyzed.

Figure 3.7 Scanning Electron Microscope (SEM).

Figure 3.8 X-ray Diffraction (XRD) equipment.

3.6.5 Electron Backscattered Diffraction

For EBSD analysis, the samples were electro-polished in the electrolyte (a mixture of perchlorate with acetic anhydride and methanolic solutions of sulfuric acid) for 30 s at -10 ºC. EBSD was conducted using FEI Quanta 200 HV scanning electron microscope equipped with TSL-OIM software with a step size of 1 μm for base metal and 200-250 mm for stir zone of FSWed samples. The microstructural features such as grain size distribution, the fraction of high angle grain boundaries (HABs) and low angle boundaries (LABs), the fraction of

recrystallized boundaries, pole figures, and orientation distribution functions (ODF) were extracted using TSL-OIM software.

3.7 Mechanical characterization

3.7.1 Microhardness tester

The microhardness was measured using a Vickers microhardness tester (Model – ECONOMET VH-1, Make – Chennai Metco, Chennai) with 100 gf load and 15 s dwell time. The hardness measurement was carried out at the midsection of samples along the transverse direction at a 0.5 mm gap between two successive indentations. The image of the hardness tester is shown in **Figure 3.9**.

Figure 3.9 Vickers Microhardness tester

3.7.2 Tensile test

Figure 3.10(a) illustrates that transverse tensile tests of gauge length 25 mm, radius 6 mm, and web 10 mm were sectioned according to ASTM E8 using a wire-cut electrical discharge machine (W-EDM). V-notch is made at the center of the stir zone to measure the actual strength of SZ, as shown in **Figure 3.10(b)**.

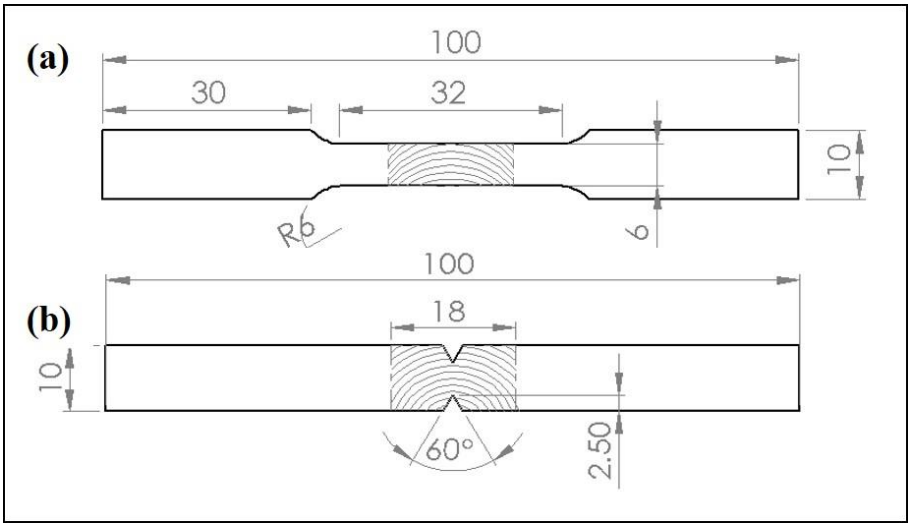

Figure 3.10 Dimensions of (a) Transverse tensile sample and (b) V-notch tensile

Figure 3.11 Universal testing machine

The tensile test was carried out on a Universal Testing Machine (UTM) (**Figure 3.11)** (M50, S.M.Engineers, Pune, India) of 100 KN capacity, and the test was performed at a crosshead speed of 0.5 mm/min. Three samples were prepared for each weld condition, and values were

recorded for the average of three samples. The fracture features of tested tensile samples are analyzed using SEM.

3.8 Corrosion

The corrosion behaviour of BM and weld samples was studied in a 3.5 % sodium chloride (NaCl) electrolytic solution using weight-loss, Tafel polarization and electrochemical impedance spectroscopy (EIS) test. The corrosion tests were conducted according to ASTM G3 standards.

3.8.1 Weight-loss test

Corrosion behaviour was analyzed using weight-loss method in 3.5 % NaCl solution at room temperature. The samples were polished and cleaned with acetone for the weight-loss method to remove the dirt. The samples were then immersed in NaCl solution for 60 days. Before immersion, the initial weight of the samples was recorded. After 60 days, the samples were removed, and pickling was performed in a 10 vol% nitric acid solution at 60ºC. The final weight of the samples was measured, and the corrosion rate was calculated using the following Equation (1) (Satyanarayana et al. 2021). Later, the corroded samples were examined using the optical microscope.

$$(\mathrm{CR}) = (534 \times \mathrm{W})/(\mathrm{D} \times \mathrm{A} \times \mathrm{T}) \qquad (1)$$

Where CR- Corrosion rate (mpy), W- Weight loss (mg/inch^2), D- Density of the samples (2.7 g/cm^3), A- Exposed area (mm^2), T- immersion time (hrs).

3.8.2 Potentiodynamic Polarization test

The Open-circuit potential (OCP) test and Tafel polarization test were conducted using a 3-electrode cell potentiostat (Make: CH Instruments, USA, Model: 604e), as shown in **Figure 3.12**. The PDP method was performed using CHI604E electrochemical workstation. The test was performed on the top surface of the samples using a three-electrode system which includes a saturated calomel electrode (SCE) as the reference electrode, weld sample as the working electrode, and platinum mesh as the counter electrode. The samples were exposed to the solution through a hole of cross-section area of 0.28 cm^2, and remaining area was masked. Before the PDP test, an open circuit potential (OCP) test was performed for 600 sec to get the equilibrium potential. The voltage values for the PDP test were kept between -0.25 V to 0.25 V and with a scan rate of 0.167×10^{-3} mV/s. The corroded samples after the PDP test were examined using SEM.

Figure 3.12 Electrochemical workstation

3.8.3 Electrical impedance spectroscopy test

EIS is the most effective and precise nondestructive electrochemical technique for evaluating corrosion behaviour. EIS information is more exhaustive and detailed than Tafel polarization information. EIS test was also performed on the same electrochemical workstation (**Figure 3.12**). The EIS test was carried out at frequencies fluctuating between 0.01 Hz to 100 kHz with an amplitude of 0.005 V. To reduce error, three samples were used in each test. The corroded samples were examined under SEM to study the corrosion attack.

3.9 Damping behaviour

The X-ray method is used to analyze the density of dislocations in the stir zone. The damping was measured at ambient temperature by varying frequency (1-20 Hz) and at 1 Hz frequency by varying temperature (ambient to 250 ^{o}C). The test was performed under 3-point bending mode using Metravib dynamic mechanical analyzer (DMA-25), as shown in **Figure 3.13**. The damping test was carried out with a constant strain amplitude of 260 $\times 10^{-6}$ and a dynamic load of 10 N.

3.10 Wear characteristics

A dry sliding pin-on-disk wear test was performed using a TRM 500 pin on the disc machine with a tribometer, as illustrated in **Figure 3.14**. The ASTM standard G99-04 was used to conduct the wear test. The corresponding discs of GCr15 produced a hardness of about 50 HRC and a 0.3 mm surface roughness (Ra). According to a conventional metallographic procedure, the pins were polished using grit SiC papers. The samples are dried in acetone and weighted to calculate the wear rate before and after the test. The dry sliding wear test was carried out for a

distance of 1000 meters under a constant load of 30 N, 50 N and a sliding velocity of 0.2 m/s.

Figure 3.13 Damping testing equipment

Figure 3.14 Pin on disc wear testing equipment.

3.11 Fatigue crack growth behaviour

The fatigue test was carried out to determine weld samples' fatigue crack growth (FCG) rate following the ASTM-E647 standard. Since surface asperities such as weld flash, tool marks, and other surface irregularities formed during the FSW could influence fatigue crack development at the notch, the CT specimen's surface was polished with SiC emery sheets to provide a smooth and flat surface. **Figure 3.15(b)** depicts the dimensions of compact tension (CT) specimens. The CT specimens were prepared using wire-cut EDM as per the dimensions

shown in **Figure 3.15(b)**. **Figure 3.15(a)** depicts a snapshot of the prepared CT sample. A fatigue testing machine (Model: UT-04-0100 MEDIAN 100, Make: BISS, Bangalore, India, frequency range – 15 Hz, capacity-100 kN) was used for the test with a stress ratio (R) of 0.10 and a frequency of 15 Hz. The FCG rate test was performed under constant force amplitude at ambient temperature. **Figure 3.16** depicts a photocopy of the fatigue testing machine. The concept aims continuously measure fracture propagation using a crack opening displacement (COD) gauge. The fractured CT specimens were then examined using SEM.

The maximum and minimum load was calculated using the following formula.

$$\Delta K = \left[\frac{\Delta P}{B\sqrt{W}}\right]\left[\frac{2+\alpha}{(1-\alpha)^{\frac{3}{2}}}\right](0.886 + 4.64\alpha - 13.32\alpha^2 + 14.72\alpha^3 - 5.64\alpha^4)$$

Where, $\alpha = a/W$,

a- Initial crack opening size (mm).

W- Distance from edge of the sample to sharp knife edge (mm).

B- Thickness of the sample (mm).

ΔK- Stress intensity range (MPa $\sqrt{m}$).

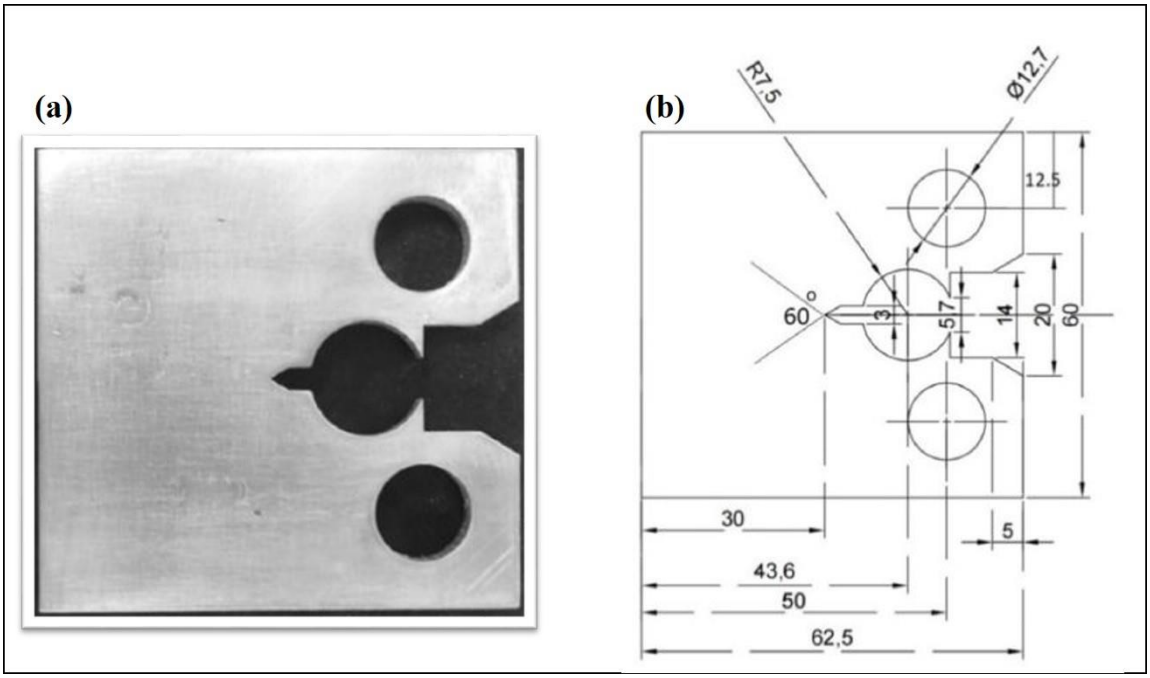

Figure 3.15 (a) Photograph of fatigue testing specimen and (b) Dimensions of fatigue sample.

Figure 3.16 Fatigue testing machine.

CHAPTER 4

RESULTS AND DISCUSSION

4.1 Introduction

The rotational and traverse speeds are two essential parameters for FSW. The reduction of mechanical properties in the stir zone can be avoided by controlling heat input during FSW. One of the effective methods that have been proposed to control and minimize the heat input is the reduction of the ratio of rotational speed to travel speed (*w/v*). In the FSW process, higher rotational speeds or low travel speeds result in increased heat input, which produces favourable circumstances for Al and brass particles diffusion reactions and results in a fine-grained zone. Moreover, the size and distribution of interlayer particles mainly depend on tool rotational speed**.** Hence, in this study, the tool rotational speed is varied, and the low travel speed is kept constant to observe the heat input effect on diffusion-reaction between brass particles and aluminium matrix. Other processing parameters, such as plunge depth and tool tilt angle, have a negligible effect on the development of the stir zone, but they were held constant in most investigations.

4.2 Selection of FSW process parameters to get defect-free joint and enhanced mechanical properties using brass interlayer

In order to find better tool design and optimum process parameters such as rotational speed and tool travel speed, initially, the trial experiment weld was carried out with interlayer by varying tool rotational speed (800-1000 rpm), keeping traverse speed constant (25 mm/min) using square tapered tool. Further, the weld was carried out using a cylindrical threaded tool with interlayer by varying rotational speed (600-1000 rpm) at constant tool traverse speed (25 mm/min). A triangular tool was also used for welding with interlayer to achieve better results.

4.2.1 Microscopic analysis

Initially, the trial experiments were carried out using a square tapered tool. The brass particles distributed non-uniformly in the SZ and formed a non-uniform composite structure, as displayed in **Figure 4.1**. **Figure 4.1** shows the macrostructure of Stir Zone (SZ) using brass interlayer at different rotational. **Figure 4.1(a)-(c)** shows that brass particles are distributed in SZ in a similar mode at all rotational speeds. Small brass particles were observed on the advancing side (AS) and large particles on the retreating side (RS). This is due to higher

temperature developed towards AS in comparison to RS during welding. The heat generation in AS is higher than in RS since material flow and deformation begins from AS. Hence the material generates more heat of plastic deformation. Further, as the direction of the tangential component of tool rotation and its traverse are the same towards AS, this causes more friction.

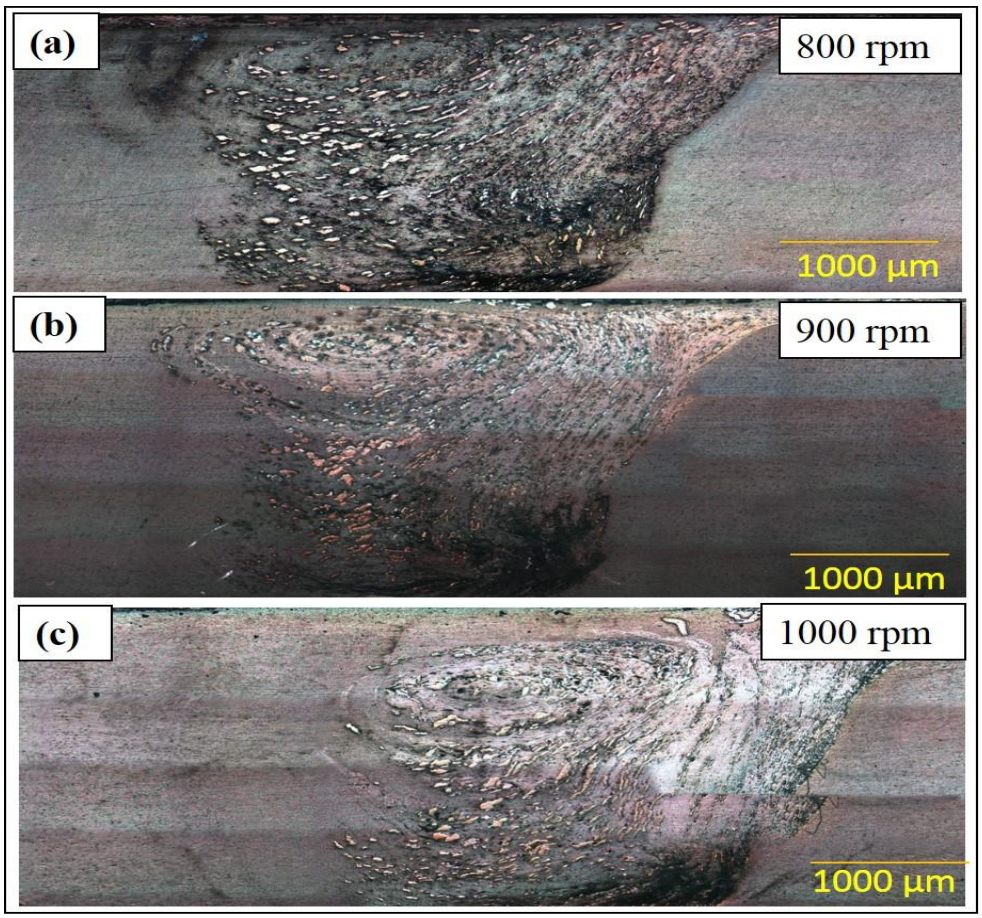

Figure 4.1 Macrostructure of weld with interlayer at different rotational speeds

From **Figure 4.2**. It was observed that large brass layers had seen dark colour as copper, while the Zinc (Zn) has dissolved due to the high diffusion rate of Zn in aluminium and formed like an Al-Zn solid solution (Mokabberi et al. 2018). However, the same bulk layers have been formed at all specified parameters. From **Figure 4.3** it was observed that aluminium and brass interlayer formed a strong metallurgical bond at the interface of Al and brass due to the stirring action of the tool. A similar metallurgical bond was observed at SZ for all selected tool rotational speeds. From **Table 4.1,** it was observed that at point 3, aluminium, copper, and zinc were found with Energy-dispersive X-ray spectroscopy (EDAX) analysis. Intermetallic compounds (IMCs) formation in SZ of welded joints such as Al_2Cu and Al_4Cu_9 are identical and confirmed in XRD analysis, as shown in **Figure 4.4**. During welding, the small brass particles and fragments were dispersed into base metal that yielded the ability to form a

composite-like structure. In other words, the interfacial diffusion and reaction between the materials result in the formation of IMCs.

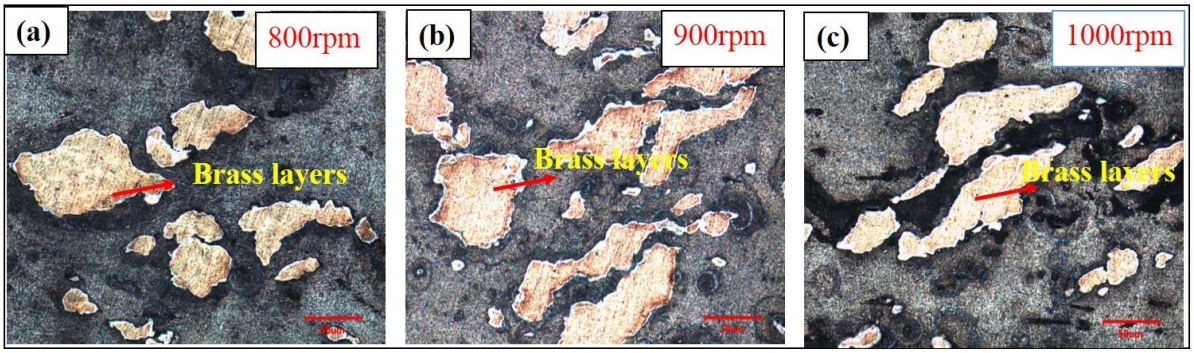

Figure 4.2 Macrostructure of weld with interlayer at different rotational speeds.

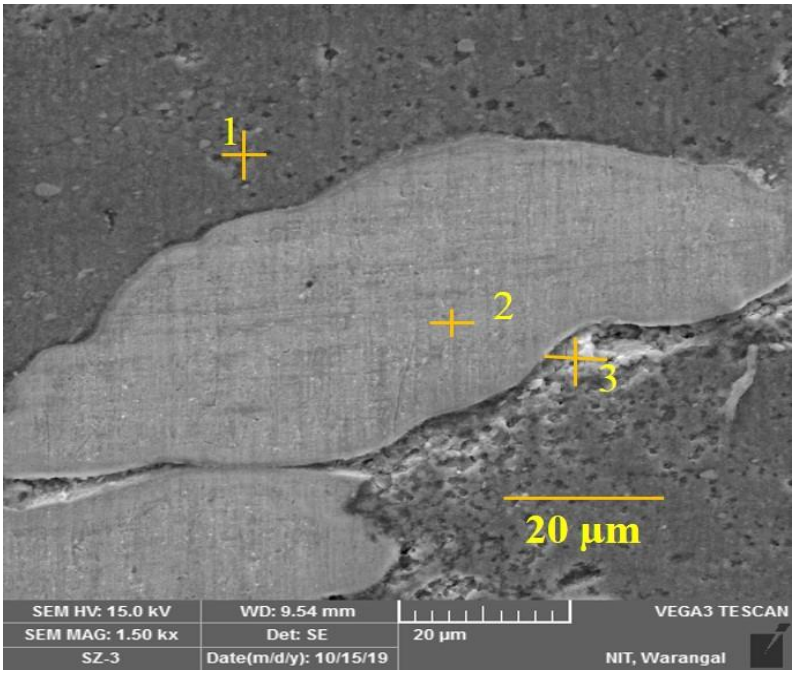

Figure 4.3 SEM image of weld at SZ.

Table 4.1 EDAX results at different points

Point	1	2	3
Al (wt %)	85	3	22
Cu (wt %)	7	58	68
Zn (wt %)	5	35	5

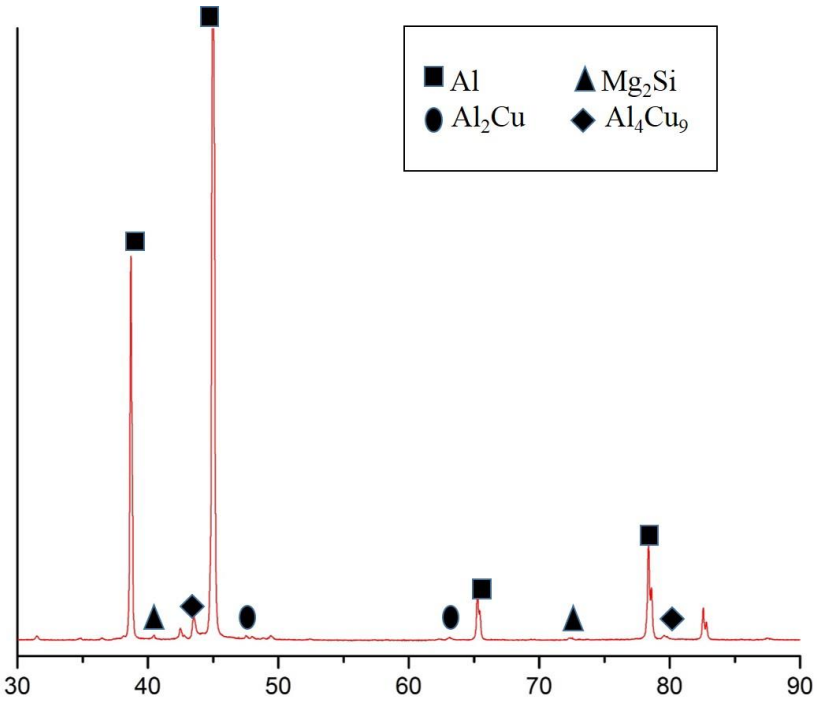

Figure 4.4 XRD results of weld with brass interlayer

4.2.2 Mechanical properties

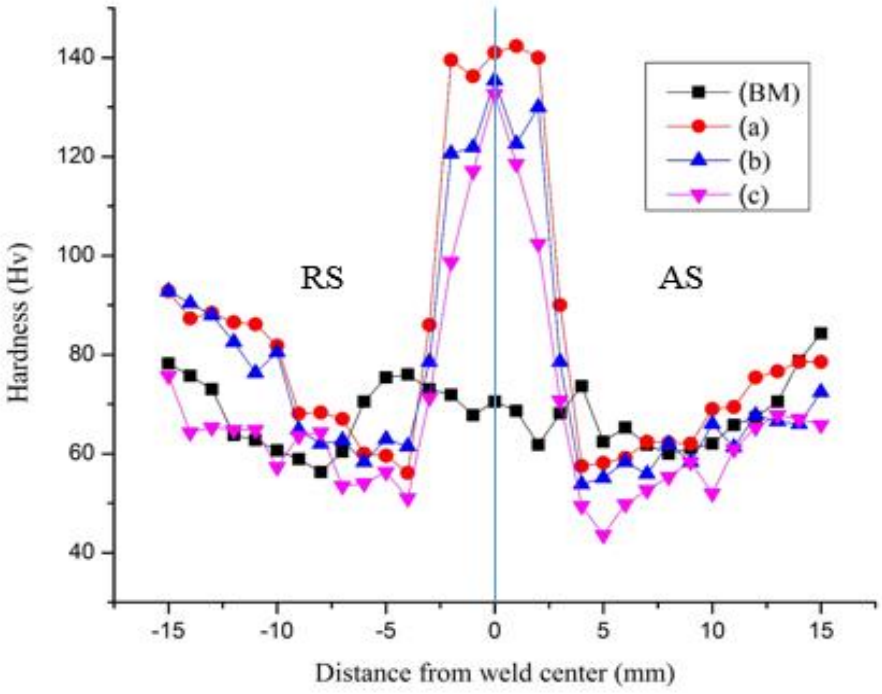

Figure 4.5 Microhardness profile of the weld using brass interlayer at (a) 800 rpm, (b) 900 rpm, and (c) 1000 rpm.

From microhardness profile as shown in **Figure 4.5**, it was observed that the hardness of weld in SZ was increased with the use of brass interlayer compared to the weld without interlayer. The increase in hardness in SZ is attributed to the distribution of brass particles and the formation of strong intermetallic phases. The average hardness value of weld metal without interlayer was 68 Hv. With brass, interlayer hardness is increased to 84 Hv at 800 rpm. The highest and lowest hardness values were obtained at 800 rpm and 1000 rpm, respectively. The effect of tool rotational speeds was observed. As the rotational speed increased, hardness decreased due to the high heat generated at higher rotational speeds. The results show that hardness values in all the zones at 800 rpm are higher. In the thermo-mechanically affected zone (TMAZ) and heat-affected zone (HAZ), the microhardness is lower than base metal due to the softening of the material.

Figure 4.6 shows the weld's ultimate tensile strength (UTS) without interlayer and with interlayer at three chosen parameters. The UTS value increased from 162 MPa to 220 MPa with interlayer at a tool rotational speed of 800 rpm. However, as the tool rotational speed increased from 800 rpm to 1000 rpm UTS value decreased which is attributed to the higher heat generation. The formation of IMCs only in SZ, but as the tool rotational speed increases, more softening of material is observed in TMAZ and HAZ, as explained in **Figure 4.5**, leading to failure of weld joint away from SZ.

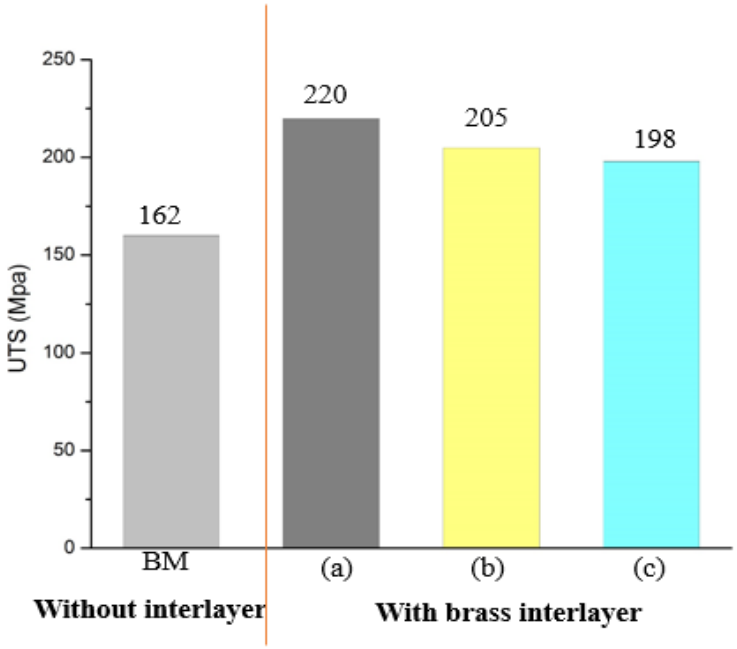

Figure 4.6 UTS of the weld without and with the use of interlayer at (a) 800 rpm, (b) 900 rpm and (c) 1000 rpm.

The lower value of joint efficiency obtained due to the small void has formed at the bottom of SZ, as shown in **Figure 4.1(a)-(c)**. The defect formation is due to the improper plunge depth, unavailability of interlayer at the bottom of SZ, and improper mixing of the material using square tapered tool.

From **Figure 4.7**, it was observed that fracture of all the welds at selected parameters had taken place towards the advancing side (AS). The crack initiated at the bottom of SZ and propagated towards AS.

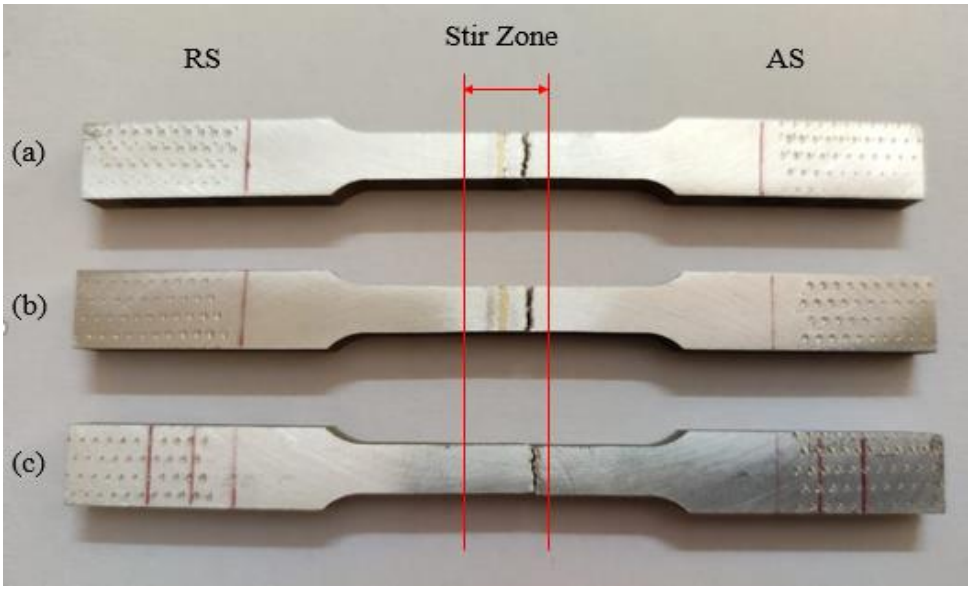

Figure 4.7 Fracture location of joints at (a) 800 rpm (b) 900 rpm (c) 1000 rpm.

In order to get defect-free joints and enhanced mechanical properties, a cylindrical threaded tool was used. The tool specifications and FSW process parameters are listed in **Table 4.2**.

Table 4.2 FSW process parameters and tool specifications

S. No.	Parameters	Values
1.	Tool rotational speed (rpm)	600, 700, 800, 900 and 1000
2.	Welding speed (mm/min)	25
3.	Tool shoulder diameter (mm)	18
4.	Tool pin length (mm)	5.9
5.	Plunge depth (mm)	0.2
6.	Tool pin diameter (mm)	6
7.	Tool tilt angle (degree)	2

4.2.3 Material flow

The macrostructure and microstructure obtained at the stir zone (SZ) of FSWed joints at various

tool rotational speeds (600 rpm-1000 rpm) with brass interlayer are displayed in **Figure 4.8** and **Figure 4.9,** respectively. The white region, i.e., SZ between black regions, denotes the area where the material is plastically deformed during welding. According to the direction of tool rotation and welding speed, the two sides of the weld joint are described as the advancing side (AS) and the retreating side (RS). The rotational and transverse speeds are two essential parameters for FSW that govern the heat input. In FSW process, higher rotational speed or slower welding speed results in increased heat input, producing favourable circumstances for Al and brass particles diffusion reactions, resulting in fine grain structure. (Huang et al. 2018) stated that the optimum combination of low welding speed and threaded pin profile results in proper material flow due to sufficient heat generation. However, The size and distribution of the brass particles in SZ mainly depend on the tool rotational speed (Akbari et al. 2012). The small brass particles in the SZ of the aluminum matrix are attributed to the intense stirring action using a threaded pin, which fragments brass interlayer particles dispersed in the SZ during FSW as shown in **Figure 4.9** From **Figure 4.9**, it was observed that the SZ consists of smaller brass particles detached from the brass interlayer and creates a chance of dispersion strengthening in the Al matrix. Therefore, the SZ can be considered as a composite with aluminium as matrix and brass particles as reinforcements. Furthermore, at low tool rotational speeds (600 rpm & 700 rpm), the heat generation is low, causing poor plastic deformation and improper material flow, resulting in more difficult to separate the brass particles. Although, defect free joint is obtained, the unreacted brass particles and non-uniform composite structure were observed as shown in **Figure 4.8(a) & (b)**. The distribution of brass particles in SZ were observed at higher magnification as shown in **Figure 4.9**. The non-uniform distribution of brass particles was observed in **Figure 4.9(a) & (b)**. The uniform composite structure in addition to the defect-free joint **(Figure 4.8(c))**, was observed at tool rotational speed of 800 rpm due to sufficient heat generation and proper material flow. The uniform distribution of brass particles was observed as shown in **Figure 4.9(c)**. At high tool rotational speeds (900rpm & 1000rpm), the excessive heat generation causes intense plastic deformation, resulting in decreased viscosity in the SZ. The decrease in viscosity enhances the flowability of materials and creates turbulence in the SZ (Mokabberi et al. 2018). The low viscosity in SZ causes softening and turbulence of brass layers at the interface, resulting in the formation of large brass layers. The large brass layers consisting of sharp angles cannot properly disperse in the aluminium matrix and lead to the formation of macro crack defects adjacent to the brass layers as presented in **Figure 4.8(d) & (e)**. In addition to this, the disappearance of composite structure is observed due to high temperature at higher rotational speeds. Although, the uniform distribution of brass

particles is observed in SZ, as shown in **Figure 4.9(d) & (e)**, the macro crack defects and the disappearance of composite structure were observed in the SZ. The defect-free joint and uniform composite structure were observed at a tool rotational speed of 800 rpm. For comparison purpose, the weld is carried without interlayer at 800 rpm and the defect-free joint was obtained with typical seen onion rings at SZ as shown in **Figure 4.8(f)** and the microstructure is shown in **Figure 4.9(f)**. The formation of onion rings confirms the proper material flow for the weld with and without interlayer at a rotational speed of 800 rpm as displayed in **Figure 4.8(c) & (f)**, whereas the brass particles are distributed along with onion rings as represented in **Figure 4.9(c)**. Therefore, sufficient heat is generated at 800 rpm and the brass particles are uniformly distributed in the SZ and it is considered as the optimum parameter to analyze the microstructure, mechanical properties, and corrosion behaviour.

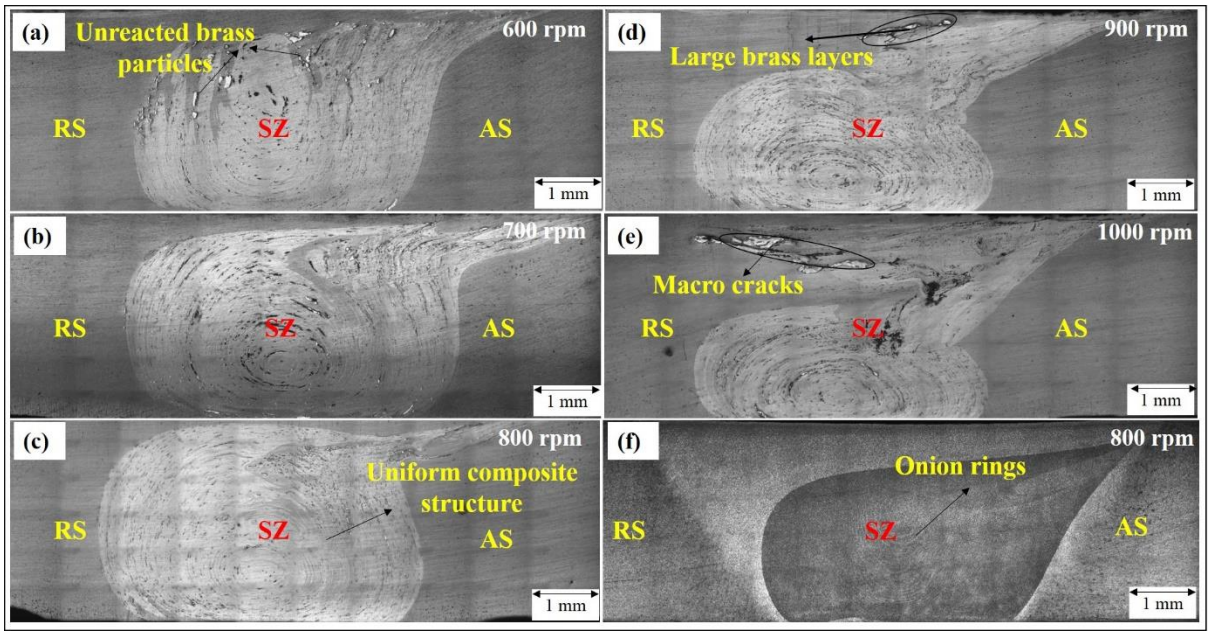

Figure 4.8 Macrostructure of weld with interlayer at tool rotational speed of (a) 600 rpm, (b) 700 rpm, (c) 800rpm, (d) 900 rpm, (e) 1000 rpm, and (f) without interlayer at 800 rpm.

The weld joint with interlayer at optimum tool rotational speed of 800 rpm formed an elliptical-shaped SZ, as shown in **Figure 4.8(c)**, whereas the weld without interlayer at the same parameters generated a basin-shaped SZ (**Figure 4.8(f)**). The shape of the SZ depends on tool geometry, process parameters, base metal temperature, and thermal conductivity (Zohoor et al. 2012). From **Figure 4.8**, it was observed that the size of SZ is less (**Figure 4.8(a)** and **(b)**) at low rotational speeds (600 rpm & 700rpm) due to improper material flow caused at lower temperature. The optimum SZ size (**Figure 4.8(c)**) is obtained at a tool rotational speed of 800 rpm. At high rotational speeds (900 rpm & 1000 rpm), a further decrease in SZ size (**Figure**

4.8(d) and **(e)**) was observed due to turbulence created at a very high temperature.

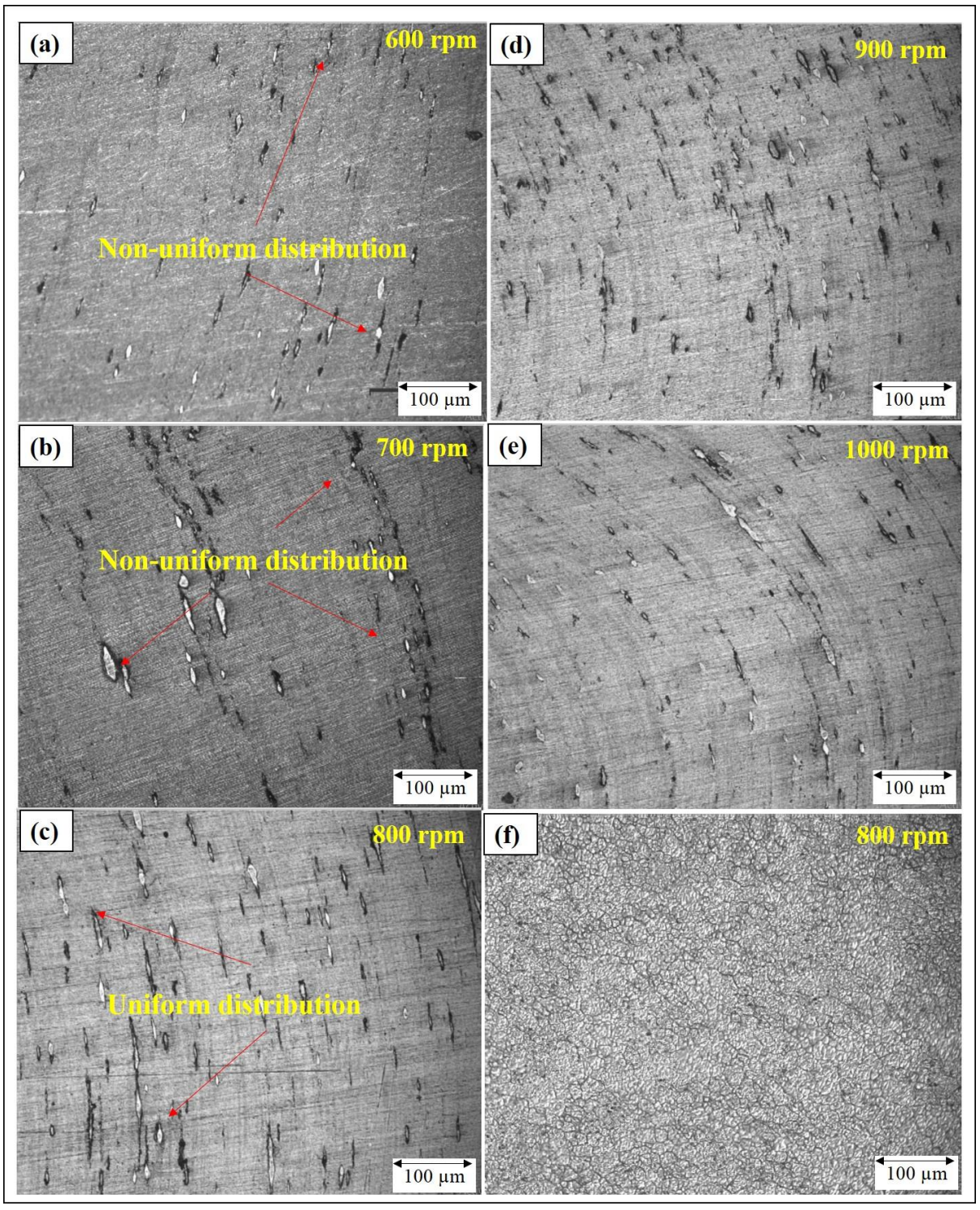

Figure 4.9 Stir zone microstructure of weld with interlayer at tool rotational speed of (a) 600 rpm, (b) 700 rpm, (c) 800 rpm, (d) 900rpm, (e) 1000 rpm, and (f) without interlayer at 800 rpm.

4.2.4 Intermetallic behaviour

The intermetallic behaviour was studied using SEM analysis, and the SEM images of BM and weld without interlayer are presented in **Figure 4.10**. The SEM image of BM shows large grains containing α-aluminium matrix. The bright region in the BM is a Si-rich element precipitated from the solid solution of AA6061 alloy, as represented with point A in **Figure 4.10(a)**. These precipitates act as strengthening precipitates and enhance the base metal strength. After FSW, these Si-rich precipitates are not dissolved completely in the Al matrix due to the higher melting point temperature than the temperature-induced (Gharavi et al. 2016). Due to the tool stirring action, these precipitate sizes got finer and were spread over the Al matrix uniformly during the FSW process. These act as strengthening precipitates for BM and FSWed joints. After FSW, the precipitates were broken into fine particles and uniformly distributed in the Al matrix, as displayed in **Figure 4.10(b)**. The EDAX results (at points A & B) confirm the presence of major alloying elements such as Mg and Si, and small white colour particles are observed as the secondary phases, as shown in **Figure 4.10(b)**. Generally, the secondary phase particles present in 6××× aluminium alloys are Mg_2Si which is unable to detect using SEM (Malopheyev et al. 2016).

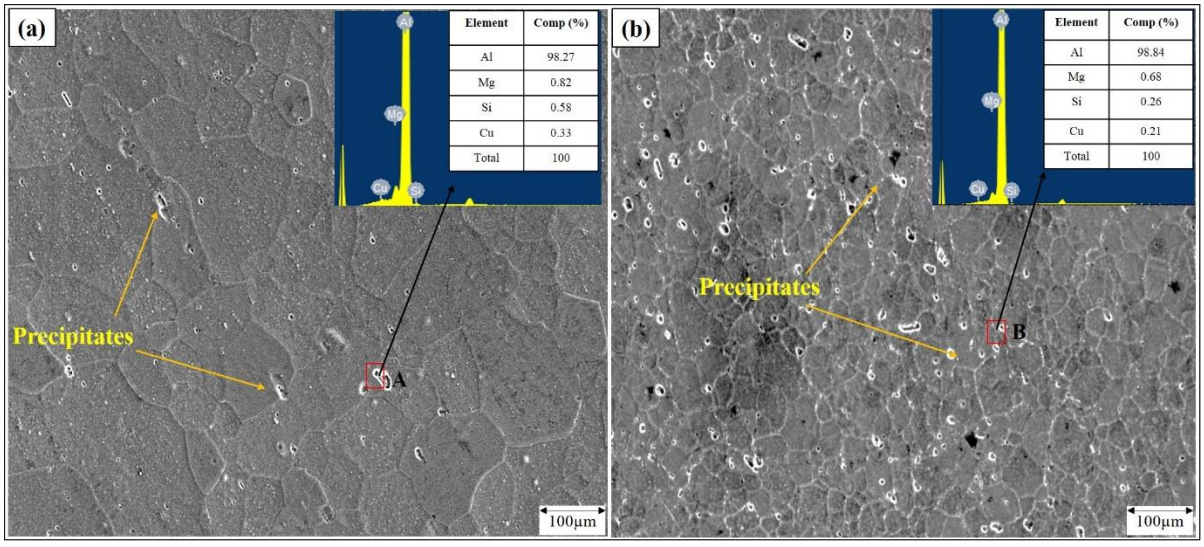

Figure 4.10 SEM and EDAX results of (a) BM and (b) Weld without interlayer

The SEM images of weld with brass interlayer are depicted in **Figure 4.11**. The brass particles and their fragments were dispersed in the SZ due to proper material flow and formed a composite-like structure, as presented in **Figure 4.11(a)**. At higher magnification, the interface of brass and aluminium was observed, as shown in **Figure 4.11(b)**. From **Figure 4.11(a)**, it was observed that brass particles were diffused in the aluminium matrix because there is a

possibility of interdiffusion reaction between brass particles and aluminium matrix attributed to the suitable temperature produced at optimum FSW process parameters (Mokabberi et al. 2018). A small diffusion layer thickness is formed at the interface **(Figure 4.11(b))** due to the interface being exposed to an appropriate temperature for a short period during the welding process. The formation of IMCs is possible where diffusion is possible at the interface. According to the aluminium–copper binary phase diagram, the simultaneous presence of copper and aluminium in a system may lead to the formation of IMCs. Moreover, at proper heat generation at optimum process parameters, IMCs formation in FSW of aluminium to brass is also possible through the solid-state diffusion between Al matrix and brass particle in the SZ. The slightly faster cooling rate for the Al-brass system results in more heat retained at the Al-brass interface, facilitating atomic diffusion and phase formation (Avettand-fènoël et al. 2020). Moreover, it is also possible that a solid solution of Zn in the aluminum matrix was obtained due to the diffusion and dissolution of Zn atoms from the brass particles in the aluminum matrix (Mokabberi et al. 2018). A few cavities and cracks around the interface were observed as a result of brittle IMCs formed during the welding process. EDAX analysis was carried out to examine the IMC's formation. EDAX spectra of marked points A, B, and C are shown in **Figure 4.11(a)** and **(b)**. The presence of Cu and Zn in all spectrums confirms the existence of brass particle fragments in the SZ. Moreover, at point A (interface of Al and brass particle), the ratio of aluminium to copper is 1.92, which is approximately the same as the weight ratio of Al_2Cu IMC. At point B (a random point away from the brass particle), the Cu and Zn weight ratio is the same, it could be the result of the formation of CuZn IMC and it indicates the presence of brass fragmentation. At point C, the weight ratio of Al and Cu is the same as Al_4Cu_9 IMC.

To confirm the diffusion and interaction of brass particle with the aluminium matrix, EDS line scan and elemental mapping were carried out for the weld with interlayer are shown in **Figure 4.12**. In the cross-section SEM image **(Figure 4.12(a))**, selected a red line for EDS scan from left to right, and the associated element intensity curves are displayed in **Figure 4.12(b)**. The diffusion i.e., interface width in the curve (**Figure 12(b)**) indicates that the relatively complete reaction of the brass particles with aluminum matrix. The dispersion of brass particles in the Al matrix was observed using EDS maps in **Figure 4.12(c)**. The slight colour difference (red and black) at the interface indicated by arrows in **Figure 4.12(c)** specifies interfacial diffusion and interaction between the two materials. The distribution of brass fragments was confirmed in EDS maps (green and purple colour) which indicates distribution of Cu and Zn elements in

aluminium matrix as displayed in **Figure 4.12(d)** and **(e)**, respectively.

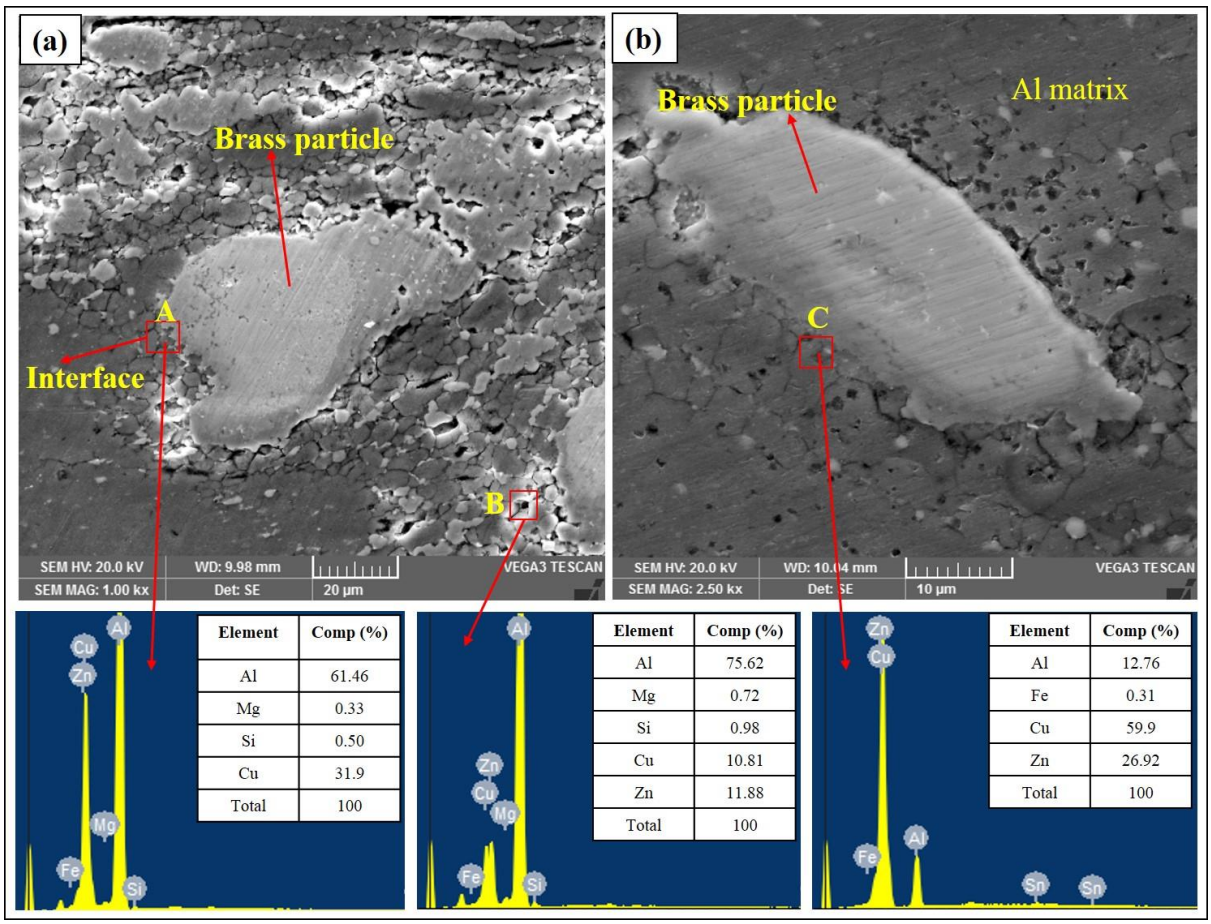

Figure 4.11. SEM and EDAX results of weld with interlayer at (a) Low and (b) High magnification.

The XRD results of BM, weld with and without interlayer are depicted in **Figure 4.13**. High-intensity peaks of Al and low-intensity peaks of Mg_2Si precipitates were observed for the base metal and weld without interlayer as depicted in **Figure 4.13(a) & (b)**. Formation of strengthening IMCs such as Al_2Cu and Al_4Cu_9 were confirmed by the XRD results for the weld with brass interlayer as shown in **Figure 4.13(c)**. More peaks of Al_2Cu were observed than Al_4Cu_9, which confirms the dominant IMC among all IMCs and uniform distribution of Al_2Cu. Al_2Cu and Al_4Cu_9 IMCs in the weld at optimum parameter conditions show that a certain amount of stirring occurs at the interface, and entraps some Cu in the stir zone. In addition, the XRD pattern shows a small amount of Cu-Zn IMC. Other researchers have also obtained the same kind of strengthening IMCs (Akbari et al. 2012; Esmaeili et al. 2011; Khojastehnezhad et al. 2018; Mokabberi et al. 2018).

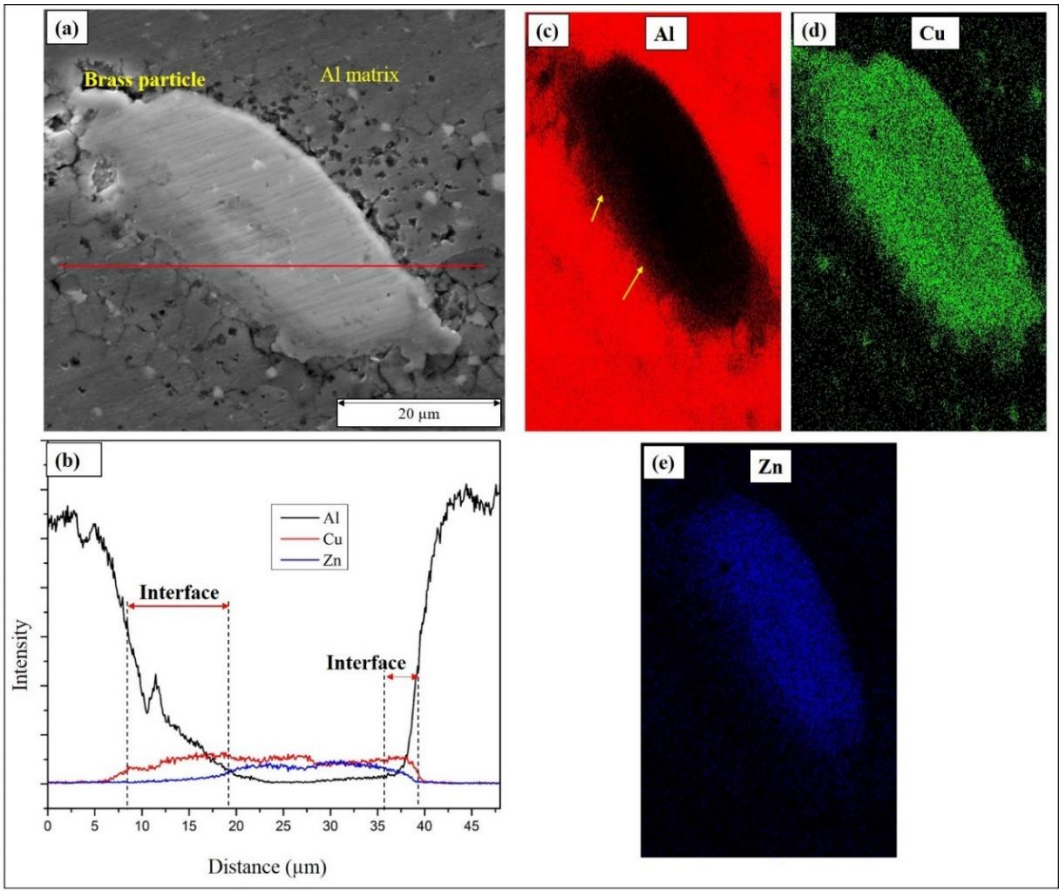

Figure 4.12 (a) SEM micrograph and (b) EDS line scan curves, and (c-e) EDS maps of weld with interlayer.

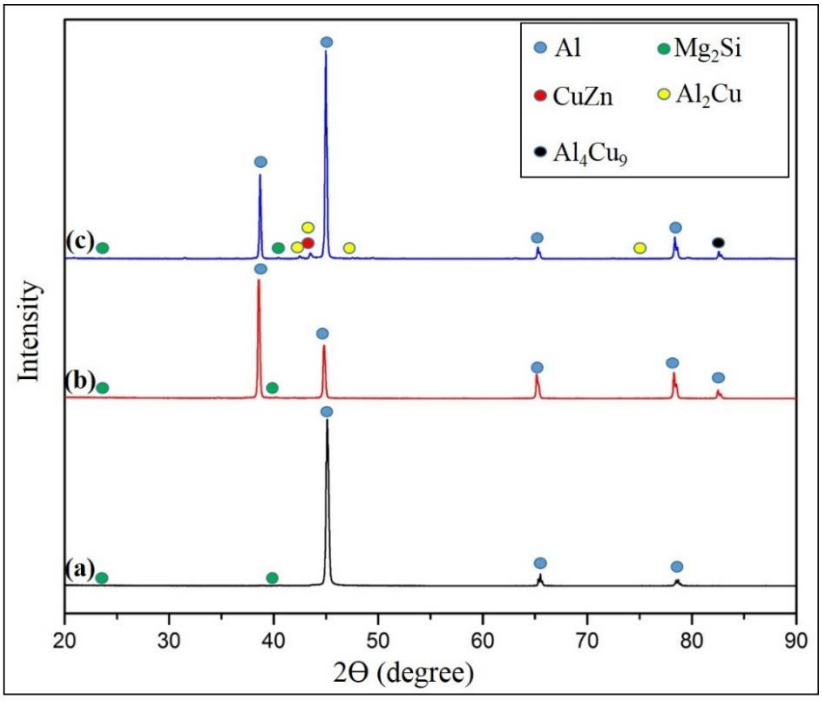

Figure 4.13 XRD plots of (a) BM, (b) Weld without interlayer, and (c) Weld with interlayer.

4.2.5 Grain structure evolution

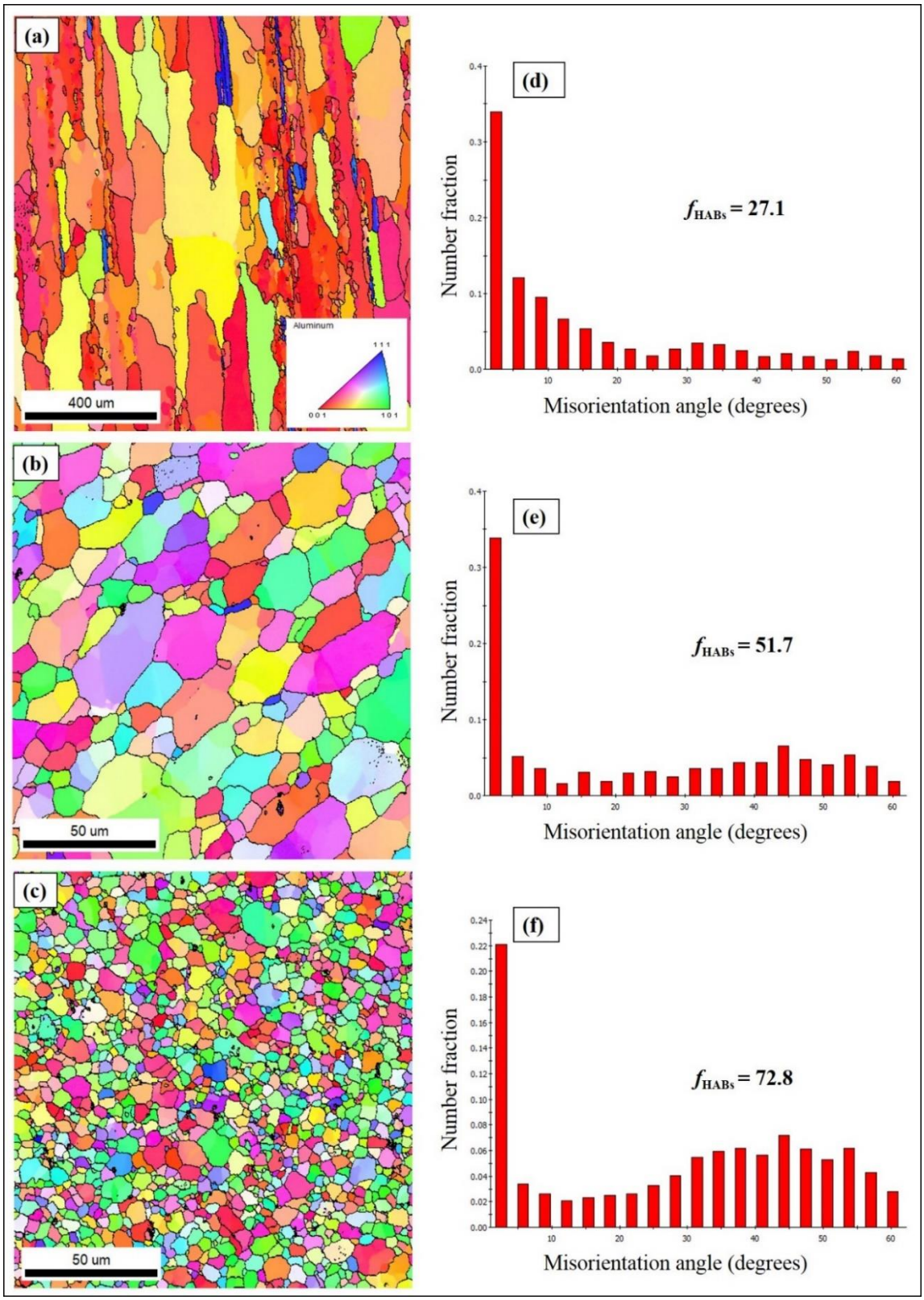

Figure 4.14 EBSD microstructure of (a) BM, (b) Weld without interlayer, and (c) Weld with interlayer, and Misorientation angle distribution chart of (d) BM, (e) Weld without interlayer, (f) Weld with interlayer.

The grain structure in the SZ was examined using the EBSD technique to understand grain structure evolution during FSW. EBSD (microstructure + inverse pole figure) images of BM, FSWed samples at 800 rpm with and without interlayer are presented in **Figure 4.14**. The fraction of low angle grain boundaries (LABs), high angle grain boundaries (HABs), and grain size are summarised in **Table 4.3**.

Table 4.3. EBSD Results

Samples	Grain Size (μm)	Fraction of grain boundaries (%)	
		LABs (<15^o)	HABs (>15^o)
Base metal	28.1 ± 3.1	72.9	27.1
Without interlayer	5.2 ± 0.6	48.3	51.7
With interlayer	2.3 ± 0.1	27.2	72.8

Based on misorientation angle distribution, the volume fraction HABs for BM, weld without, and with interlayer are represented in **Figure 4.14(d), (e)** and **(f)** respectively. The BM shows the elongated grain structure oriented along the rolling direction consisting of high fraction of LABs (**Figure 4.14(a))** with an average grain size of 28.1μm. The grain refinement with a high fraction of HABs was observed for the weld with and without interlayer (**Figure 4.14(b)** and **(c))** formed due to the severe plastic deformation (SPD) and dynamic recrystallization (DRX) mechanism during FSW. The increase in HABs was due to dynamic recovery (DRV) and continuous DRX (CDRX).

The CDRX is an effective DRX mechanism for aluminium alloys, can significantly influence grain structure evolution, and refined grains can be generated (Yu et al. 2021) (Fonda et al. 2021). Since alloying additions to aluminium have no evident influence on the stacking fault energy, DRV is predicted to dominate in aluminium alloys when subjected to hot deformations (Mcnelley et al. 2008). Generally, DRV arises during the hot working of metals like Al alloys consists of high stacking fault energy. At the initial deformation stage, the rise in flow stress leads to dislocations multiplication and interaction. The increase in dislocation density can increase the rate of recovery and dislocations start to rearrange and forms low angle grain boundaries (LABs) as subgrains develop. The dislocations were continually generated in the grains and subgrains during the higher temperature deformation to accommodate the strain incompatibility of adjacent grains and subgrains, leading to the beginning of CDRX. In CDRX, by repeatedly absorbing of dislocations into the subgrain boundaries, the subgrains grow and rotate, resulting in the development of equiaxed recrystallized grains with HABs (Mcnelley et

al. 2008; Su et al. 2005). The volume fraction of HABs for the weld with interlayer is higher than weld without interlayer.

Moreover, with the addition of brass interlayer, more grain refinement was observed **(Figure 4.14(c))** because the brass particles act as a nucleation site for further recrystallization process, resulted in small grains than weld without interlayer **(Figure 4.14(b))**. The correlation between the heating time (t), nucleated grain size (D_o), and average grain size (D) is presented in Equation (2).

$$D - D_o = kt^n \quad (2)$$

Where k is a constant coefficient, D_o is the nucleated grain size at the start of the experiment. Generally, the n value is less than 0.5, but at higher temperatures and lower solute atoms in the solid solution, the value will rise to more than 0.5. In contrast to the commercially usable aluminium base metal, adding a brass interlayer and the dissolution of Zn and Cu atoms in the aluminium matrix raises the impurity atoms and reduces the exponent n in Equation (2) (Mokabberi et al. 2018). As a result, weld with interlayer resulted in finer grain structures in the stir zone than weld without interlayer.

4.2.6 Mechanical properties

4.2.6.1 Microhardness

The microhardness profile along the transverse cross-section of weld samples is presented in **Figure 4.15**. The hardness of SZ, HAZ and TMAZ of weld joints with and without interlayer is lower than base metal (110 Hv). The mechanical stirring and heat cycle impact the evolution of the dislocations, grain size, and particularly precipitates, which further influence the subsequent mechanical properties in FSW (Meng et al. 2021). AA6061-T6 alloy is a precipitation hardening alloy, affecting the mechanical properties of the FSW sample with the precipitation factor rather than the grain refinement factor. Due to more prolonged thermal exposure at elevated temperatures (0.6–0.7T_m, where T_m is the melting point temperature of BM) during FSW, the dissolution of the precipitate and coarsening may occur. As a result of the dissolving of second-phase particles and the decrease in dislocation densities, the hardness of the FSWed samples decreases at SZ (Satyanarayana et al. 2021).The average hardness in SZ for the weld with interlayer (85 Hv) is higher as compared to the weld without interlayer (65 Hv) due to the formation of hard IMCs which was discussed in SEM and XRD analysis. The hardness of weld with interlayer is directly influenced by the distribution of detached interlayer

particles and the formation of IMCs (Khojastehnezhad et al. 2018). The hardness values in the retreating side (RS) are lower than the advancing side (AS) for both the weld joints due to the high thermal softening caused by the high temperature generated in HAZ on RS (Kumar et al. 2021).

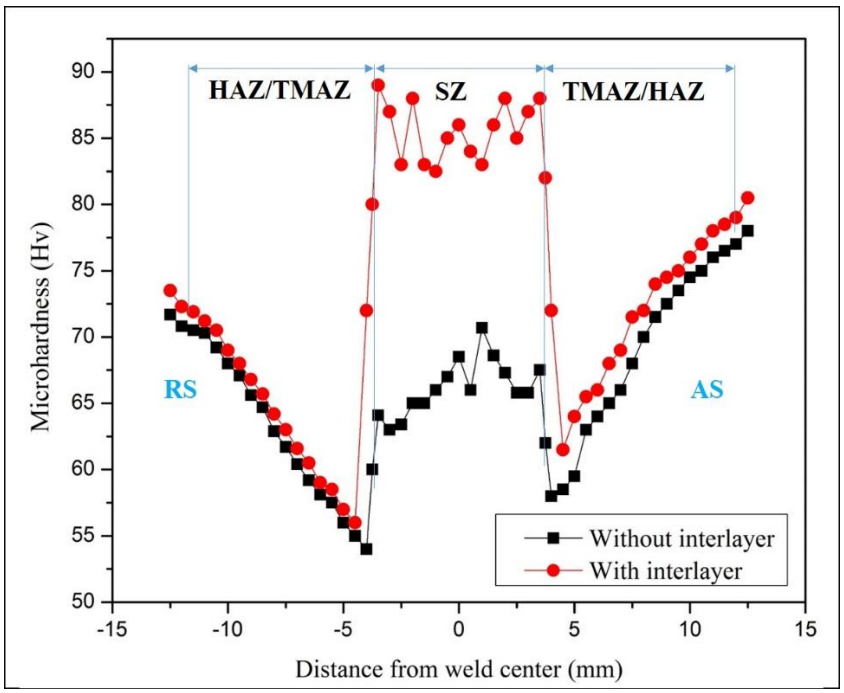

Figure 4.15 Microhardness profile of weld join at 800 rpm with and without interlayer.

4.2.6.2 Tensile test

The tensile curves of BM and both weld samples are presented in **Figure 4.16** and tensile properties are summarized in **Table 4.4**. From **Figure 4.16(a)**, it was observed that the strength of welds with and without interlayer is relatively lower than the BM due to the thermal softening caused at SZ as explained in the hardness analysis**.** However, weld with interlayer showed higher strength than weld without interlayer. The proper material flow and formation of uniform composite-like structure at optimum tool rotational speed of 800 rpm resulted in perfect metallurgical bonding at the interface. The formation of IMCs at the SZ resulted in strong bonding between aluminium and brass. This diffusion layer at the interface gradually merges two materials (i.e., aluminium and brass), avoiding sharp metallurgical differences that can deteriorate the mechanical properties. Furthermore, the lamellar dispersion of IMCs serves as a crack propagation barrier. When a load is applied during the tensile test, cracks prefer to travel over hard particle-rich regions, but cracks deflect through the hard particle-poor regions (Esmaeili et al. 2011). The above factors led to an increase in the strength of the weld with interlayer. The weld joint strength with interlayer is increased from 192 MPa without interlayer

to 247 MPa with interlayer. The weld joint efficiency with interlayer increases from 55% without interlayer to 71% with interlayer corresponding to that of base metal. Moreover, the elongation decreases for weld with interlayer compared to weld without interlayer due to the formation of hard IMCs in SZ.

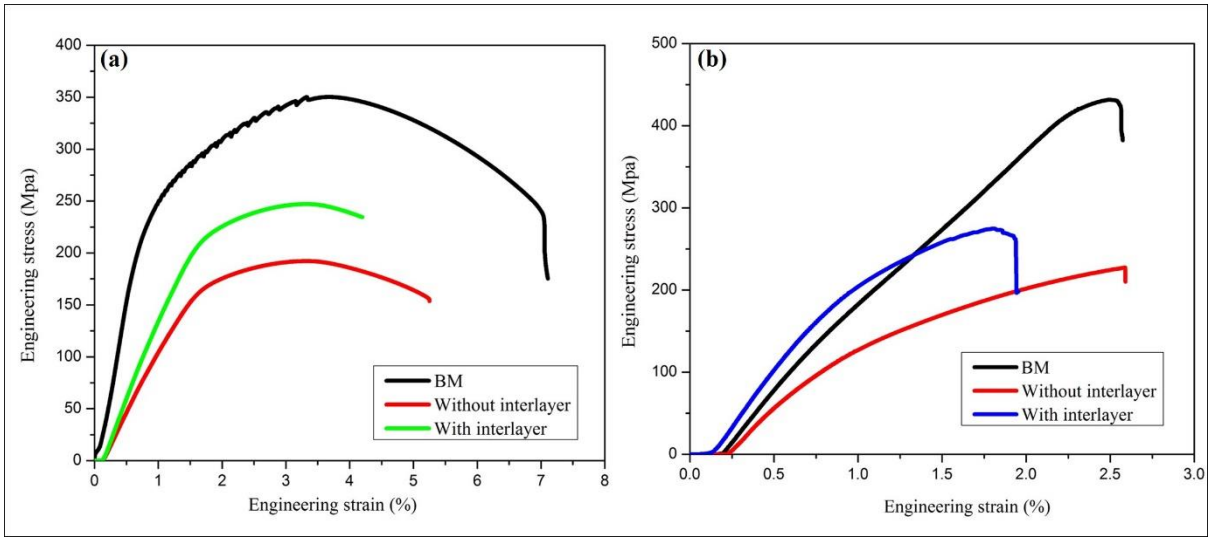

Figure 4. 16 . Stress-strain curves of (a) Transverse tensile specimen, and (b) V-notch tensile specimen.

Table 4.4 Tensile test values

Alloy	Transverse tensile test		V notch tensile test	
	UTS (MPa)	YS (MPa)	EL (%)	NTS (MPa)
Base metal	345 ± 5	245 ± 4	7.1 ± 1.1	431 ± 6
Weld without interlayer	192 ± 3	164 ± 3	5.2 ± 0.8	227 ± 5
Weld with interlayer	247 ± 4	210 ± 3	4.1 ± 0.3	274 ± 4

UTS: Ultimate tensile strength, **YS**: Yield strength, **EL**: Elongation, **NTS**: Notch Tensile Strength.

The fracture locations of the transverse tensile test samples are shown in **Figure 4.17**. The weld without interlayer fractured on the retreating side at the interface of TMAZ-HAZ, as displayed in **Figure 4.17(b),** and the weld with interlayer fractured in HAZ on RS as shown in **Figure 4.17(c)**. The load is concentrated in the lower strength region, i.e., the HAZ region of the weld joint during tensile deformation (Wang et al. 2016). From **Figure 4.8**, it was observed that shattered brass particles accumulation and more IMCs formation on AS as the material flows from RS to AS. The temperature-induced during FSW is asymmetric and higher temperature

is found on RS led to a decrease in hardness as discussed in microhardness section. These are the causes for fracture of weld samples on RS at the HAZ-TMAZ interface. All the tensile failures have occurred either at HAZ or TMAZ, and no failure was observed in SZ. Therefore, a V-notch tensile specimen was prepared and tested to ensure and compare the actual strength in the SZ of weld joints. The stress-strain curves of V-notch tensile specimens are displayed in **Figure 4.16(b)** and the tensile properties are summarised in **Table 4.4**. The results show that the strength of V-notched samples shown higher strength than transverse tensile tested samples. Based on these results, it was concluded that the load-carrying capacity of V-notch tensile samples is higher due to load concentration acting at higher hardness i.e., sharp notched SZ area. The failure of the samples obtained in SZ **(Figure 4.17(d)-(f))** shows the actual strength of the weld. The V-notch tensile strength of the weld joint with interlayer is higher than the joint without interlayer.

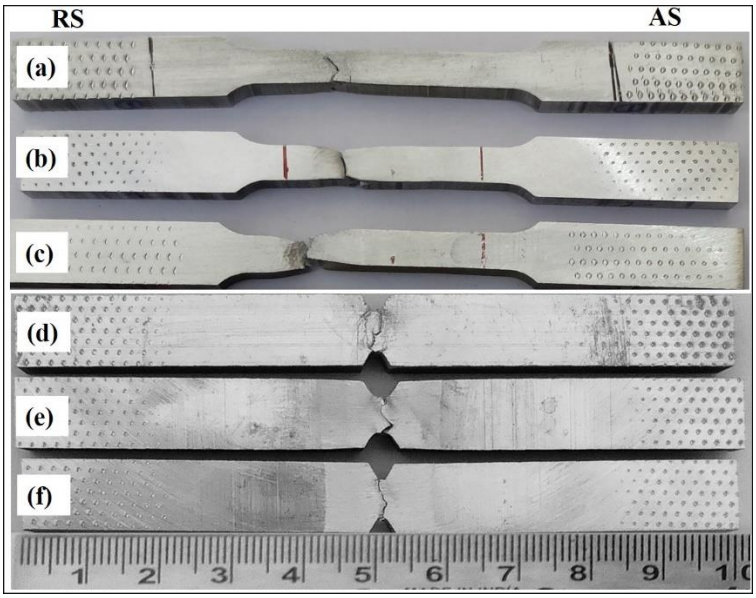

Figure 4.17 Fractured transverse tensile samples of (a) BM, (b) weld without interlayer, and (c) weld with interlayer. Fractured V-notch tensile samples of (d) BM, (e) weld without interlayer, and (f) weld with interlayer

The fracture surfaces of the transverse tensile tested specimen are depicted in **Figure 4.18.** From **Figure 4.18**, it was observed that all the fractures are composed of different sizes of dimples which indicates that the failure is due to the ductile shear fracture. BM shown a high density of large dimples **(Figure 4.18(a))**, whereas weld without interlayer shown a low density of large dimples, as represented in **Figure 4.18(b)**. The small dimples and flat surfaces for the weld with interlayer have shown the ductile and brittle fracture as displayed in **Figure 4.18(c)**,

attributed to the continuous distribution of IMCs.

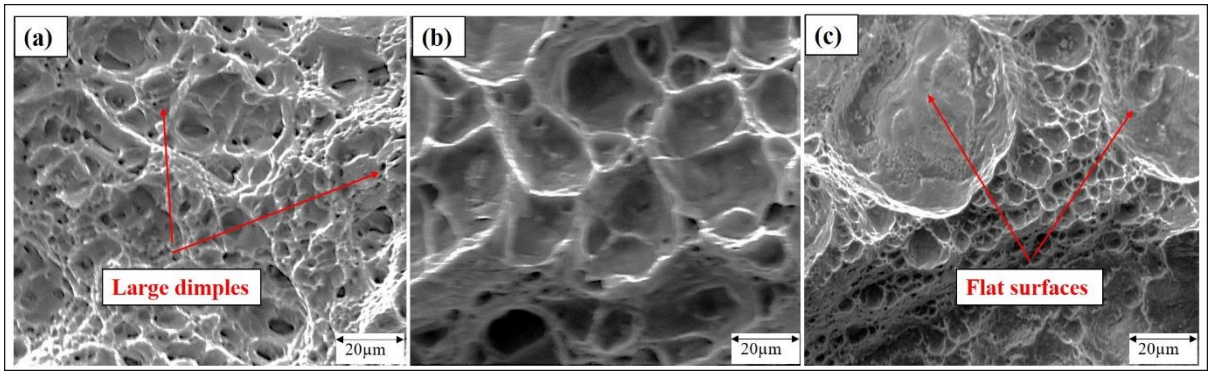

Figure 4.18 . Fracture images of (a) BM, (b) Weld without interlayer, and (c) Weld with interlayer.

4.2.7 Corrosion behaviour

4.2.7.1 Weight loss test

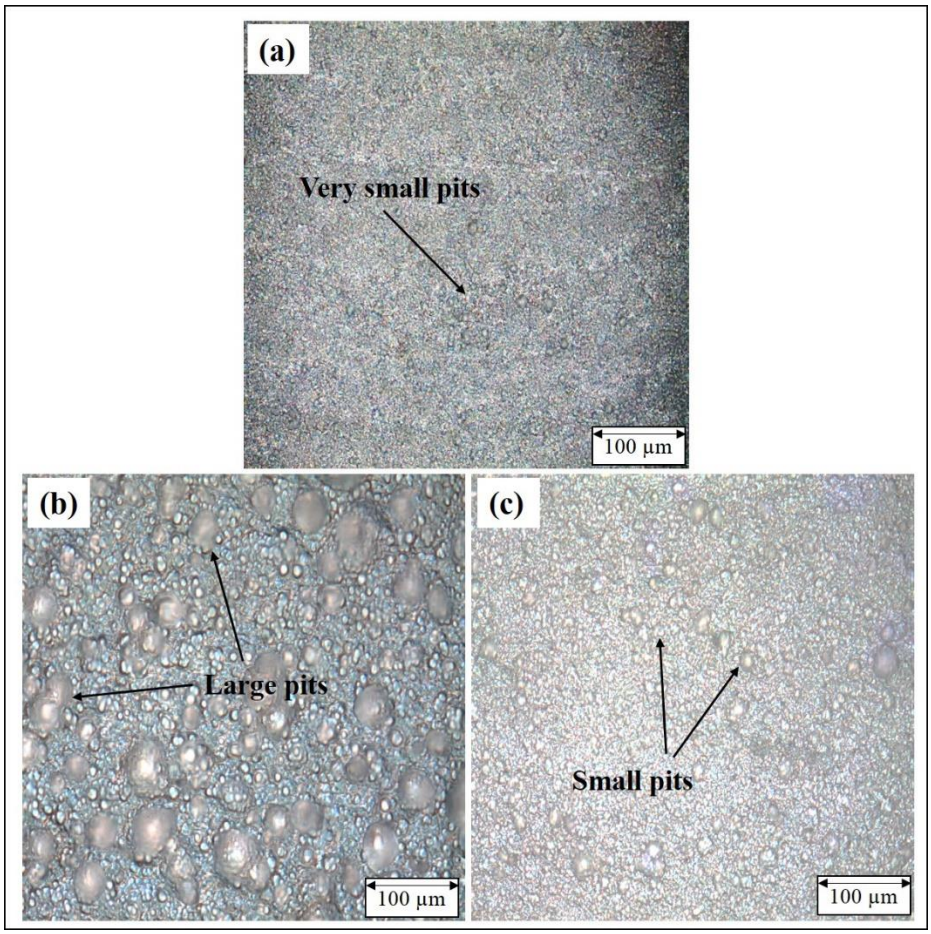

Figure 4.19 Corroded surface of (a) BM, (b) weld without interlayer, and (c) weld with interlayer after immersion test.

The weight loss and corrosion rate of the immersed samples are documented in **Table 4.5**. It was observed that the corrosion rate of welded samples is more than BM, indicating that corrosion rate increased after FSW. The weight loss occurs due to the dissolution of the corroded surface of aluminium during the initial stage of oxidation (Sravanthi et al. 2018) Generally, the weight loss of the samples is based on the corrosion attack and formation of pits, as shown in **Figure 4.19**. At the end of the process, pits are formed on the samples with ring-like deposits (corrosion products). The formation of small pits **(Figure 4.19(a))** on BM and weld with interlayer (**Figure 4.19(c))** indicates that these samples have a low susceptibility to localized corrosion after immersion. The more corrosion attack for the weld without interlayer has comprised with the large pits as shown in **Figure 4.19(b)**.

Table 4.5 Weight loss test results

S. No.	Samples	Weight loss (mg/cm^2)	Corrosion rate (mpy)
1	Base metal	8.5 ± 0.9	7.49 ± 0.8
2	Weld with interlayer	10.9 ± 1.2	9.66 ± 0.9
3	Weld without interlayer	19.8 ± 2.0	17.57 ± 1.8

4.2.7.2 OCP Test

The open-circuit potential (OCP) curves of BM and weld samples are displayed in **Figure 4.20(a)**. The OCP curves for the BM and FSWed samples maintained approximately constant trends throughout the process with slight fluctuations. From these results, it was concluded that the stability of potential is due to the homogeneous surface reactivity. The small fluctuations in potential are due to the surface of the alloy being attacked by the chloride solutions. The primary causes of fluctuations are the formation and dissolution of passive film in dynamic competitive equilibrium (Rao et al. 2010). The final OCP values of BM, weld with and without interlayer are -830 mV, -850 mV, and -890 mV respectively. The welded samples showed more electronegative values than BM. Moreover, the weld with interlayer shown less electronegative value than weld without interlayer, which indicates that weld with interlayer has low tendency to corrode as compared to weld without interlayer.

4.2.7.3 Potentiodynamic polarization (PDP) test

The PDP curves of BM and welded samples are presented in **Figure 4.20(b)**. The corrosion resistance of the samples is represented as E_{cor} (corrosion potential) which is a thermodynamic

parameter, can reflect the corrosion resistance of the metals (Zhang et al. 2020). Based on PDP curves, the E_{cor} corresponds to the tip of the polarisation curve, i.e., the intersection point of the anodic and cathodic polarization curve. The E_{cor} is the point at which the metal starts to corrode. Poor and better corrosion resistance is indicated by a low corrosion potential (more negative value) and high corrosion potential (less negative value) respectively. The potential values of BM, weld surface with and without interlayer are -860 mV, -880 mV, and -905 mV respectively. The BM showed better corrosion resistance than welded samples. The distribution of precipitates undergoes a cathodic reaction and forms a galvanic coupling with the Al matrix. Generally, the corrosion rate of metals depends on the difference in electrochemical potential between Al matrix and precipitates. During the corrosion process, precipitates act as cathode and aluminium acts as an anode. The potential gap accelerates anodic and cathodic processes by transferring electrons from the anode to the cathode, driving galvanic corrosion. For larger potential difference, the driving force is higher leads to a decrease in corrosion resistance (Joon et al. 2019). The weld joint with interlayer shown better corrosion resistance than weld without interlayer, as presented in **Figure 4.20**.

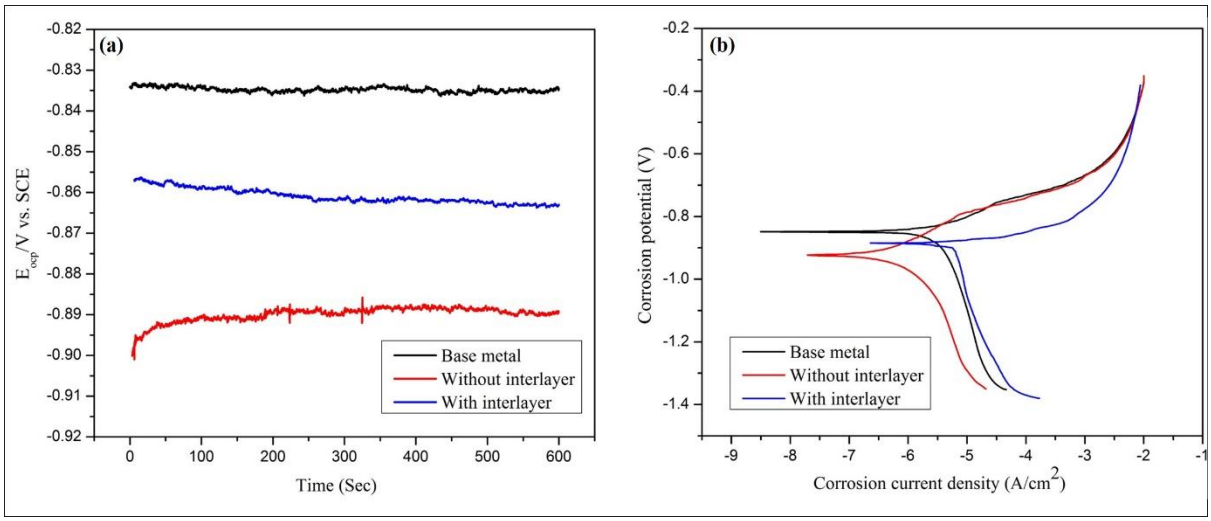

Figure 4.20 (a) OCP curves, and (b) PDP curves of BM, weld with and without interlayer

The Mg_2Si precipitate has a more negative value of corrosion potential, and galvanic interaction between these precipitates and the Al matrix is more results decrease in corrosion resistance for the weld without interlayer (E. et al. 2011). The improved corrosion resistance for the weld with interlayer is attributed to the formation of Al_2Cu IMC, which has less activation energy to the corrosion process (Chen et al. 2007). This suggests that the galvanic interaction between these IMCs and the Al matrix is very little and improved the corrosion resistance. The improvement in corrosion resistance due to the formation of Al_2Cu IMC in Al-Cu dissimilar FSW was observed by (Akinlabi et al. 2014). In addition, the improvement in

corrosion resistance of the aluminium weld joint with the addition of Zn interlayer as compared to the weld without Zn interlayer is observed (Shamsipur et al. 2018).

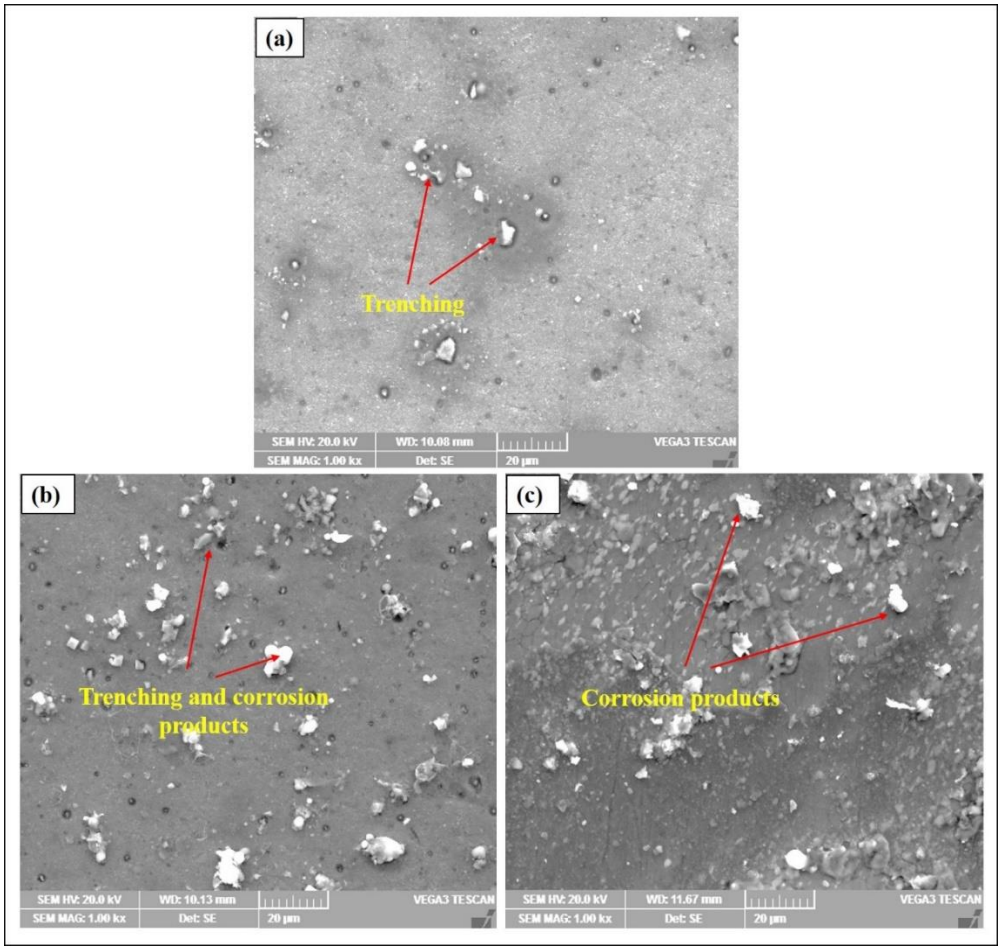

Figure 4.21 SEM images of corroded samples (a) BM, (b) Weld without interlayer, and (c) Weld with interlayer

At the beginning of the corrosion process, the precipitates dissolve around the aluminium called trenching. The BM showed small trenches, and no pits were observed, as displayed in **Figure 4.21(a)**. For the weld without interlayer, due to the more negative value of Mg_2Si precipitates, which start to dissolves faster than the Al matrix, thus sample shown the corrosion products and more number of trenches, as displayed in **Figure 4.21(b)**. The corrosion products are observed for the weld with interlayer **Figure 4.21(c)** and IMCs are not dissolved as the galvanic interaction of Al_2Cu and Al matrix is less. These results conclude that weld with interlayer shown better corrosion resistance than weld without interlayer. The PDP test results are in good agreement with the immersion test.

The weld is also carried out using triangular tool and with interlayer by varying rotational speeds. The results showed the large unreactive brass particles in the SZ.

Hence, cylindrical threaded tool and optimized parameters such as 800 rpm rotational speed and 25 mm/min tool transverse speed are considered as best parameters to enhance the mechanical properties of the weld with interlayer. The cylindrical threaded tool and optimized parameters are used for water-cooled FSW.

4.3 Effect of cooling media and interlayer on microstructure and mechanical properties of welded joint

4.3.1 Macro and microstructure

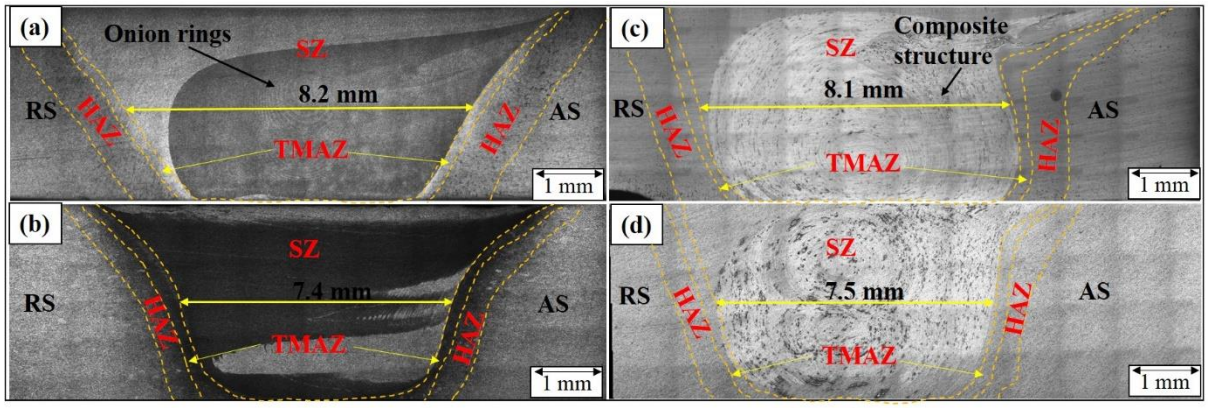

Figure 4.22 Macrostructures of weld without interlayer of (a) NCFSW, (b) WCFSW and with interlayer of (c) NCFSW, (d) WCFSW

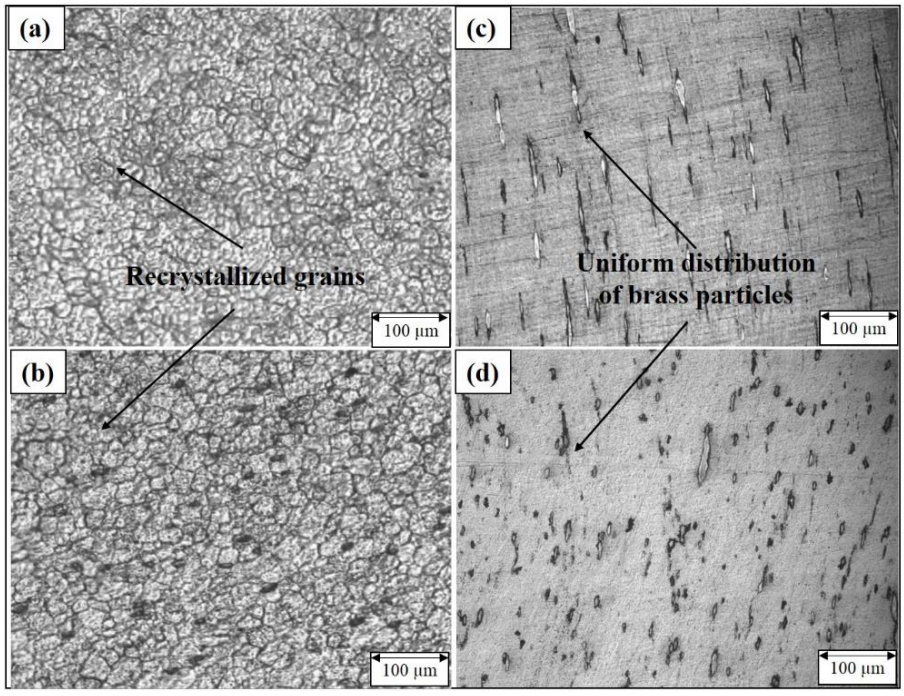

Figure 4.23 SZ microstructures of weld without interlayer of (a) NCFSW, (b) WCFSW and with interlayer of (c) NCFSW, (d) WCFSW

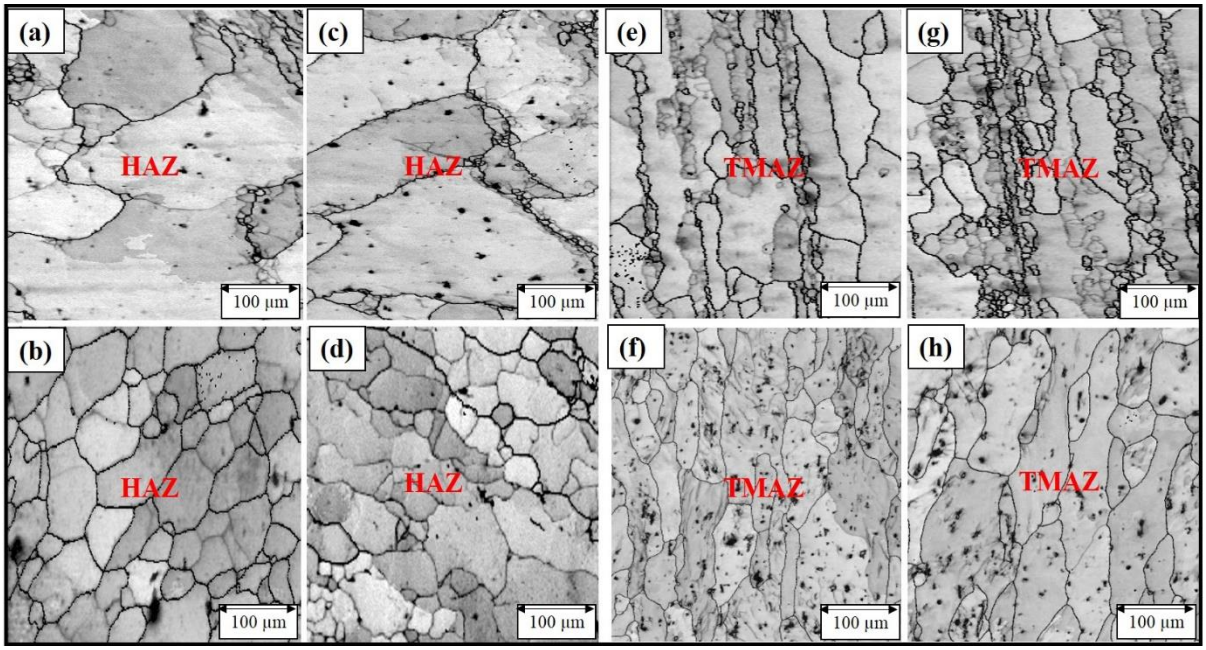

Figure 4.24 HAZ microstructures of weld without interlayer of (a) NCFSW, (b) WCFSW and with interlayer of (c) NCFSW, (d) WCFSW. TMAZ microstructures of weld without interlayer of (e) NCFSW, (f) WCFSW and with interlayer of (g) NCFSW, (h) WCFSW

The macrostructures obtained from FSWed AA6061 joints under both cooling media are presented in **Figure 4.22.** Due to heat generation and intense plastic deformation during FSW, distinct grain size occurs in different zones. Lines separating the different zones are displayed in **Figure 4.22.** From the macrostructure, three different zones, SZ, TMAZ, and HAZ were identified. **Figures 4.23** and **4.24** show high magnification images of SZ, HAZ, and TMAZ to better illustrate and discuss the microstructure developed during welding. The weld cross-section represents defect-free joints at all weld conditions, as shown in **Figure 4.22(a)-(d)**. The brass particles' uniform distribution was observed in the SZ of NCFSW and WCFSW (**Figure 4.23(c)** and **(d))**, respectively. Consequently, the uniform composite structure was obtained for the weld joints with interlayer under both cooling media, as shown in **Figure 4.22(c)** and **2(d)**. The uniform composite structure consists of brass particles as reinforcement and Al as matrix. The defect-free joint with typical onion rings is observed for weld without interlayer under both cooling media, as displayed in **Figure 4.22(a)** and **(b)**. **Figure 4.23(a)** and **(b)** shows the dynamically recrystallized fine and equiaxed grains in SZ for the weld without interlayer under both cooling media. The typical feature of onion rings structure was observed for all weld joints, and the brass particles are dispersed along with the rings, as shown in **Figure 4.23(c)** and **(d)**. The width of SZ was measured at the midsection along the transverse direction for all the weld conditions and varied with cooling media. The SZ width of WCFSW joints with and

without interlayer is reduced, as shown in **Figure 4.22(b)** and **(d**), compared to the NCFSW weld. At HAZ, the coarse grains were observed for NCFSW with and without interlayer, as shown in **Figure 4.24(a)** and **(c)**, respectively. Simultaneously, TMAZ formed for NCFSW with and without interlayer, as displayed in **Figure 4.24(e)** and **(g)**. A decrease in grain size was observed at the HAZ for the WCFSW with and without interlayer (**Figure 4.24(b)** and **(d))**, respectively. Refined and elongated grains at TMAZ of WCFSW with and without interlayer were observed compared to NCFSW weld as displayed in **Figure 4.24(f)** and **(h)**.

Based on macrostructure (**Figure 4.22**), it can be deduced that there is a significant difference in grain size of weld joints. The intense tool stirring action of the threaded pin fragmented the brass interlayer and dispersed it throughout the SZ (**Figure 4.23(c)** and **(d))**. Therefore, there is a possibility of dispersion strengthening in Al matrix during the FSW process. This may result in the formation of a composite structure with Al matrix (**Figure 4.22(c)** and **(d))**. Additionally, the appropriate dispersion and distribution of brass particles in the Al facilitate material mixing and effective metallurgical bonding as a result of sufficient heat generated at optimized process parameters (Xue et al. 2011). The severe plastic deformation and heat generated due to the friction between tool and BM, resulted in the recrystallization process in SZ (Wahid, Khan, and Siddiquee 2019). As a result, the equiaxed grain structure was obtained for weld without interlayer under both cooling media (**Figure 4.23(a)** and **(b)**). The detailed microstructural analysis at the SZ of all weld joints was discussed in the later section with EBSD results.

The weld without interlayer formed basin-shaped SZ **(Figure 4.22(a)** and **(b))** and the weld with interlayer formed elliptical-shaped SZ as shown in **(Figure 4.22(c)** and **(d))** under both cooling media. The shape of SZ primarily depends on tool geometry, thermal conductivity, process parameters, and BM melting point temperature (Zohoor et al. 2012). One interesting phenomenon observed from the macrostructure was that the cooling condition influences material flow. The temperature generated during NCFSW relieves material flow stress, which causes turbulence, resulting in a larger size of SZ (**Figure 4.22(a)** and **(c))**. The reduction in the size of SZ (**Figure 4.22(b)** and **2(d))** with water cooling is due to faster cooling rate attributed to the complete submergence of weld plates during WCFSW. When the samples are welded in water, the excess heat would be removed in time, resulting in a lower temperature. Moreover, the low temperature in WCFSW dominates the pin-driven global material transportation, while shoulder-induced flow dominates in the NCFSW joint (Patel et al. 2020). As a result of this phenomenon, WCFSW joints exhibited less plastic deformation, and the limited role of shoulder-induced flow resulted in a smaller SZ size than NCFSW joint.

The coarser grains occurred in HAZ (**Figure 4.24(a)** and **(c)**) due to the thermal cycle and because of no deformation during FSW process. The elongated grains in TMAZ (**Figure 4.24(e)** and **(g)**) were due to the frictional heating, and slight mechanical deformation containing slightly refined and elongated grains (Kumar et al. 2021) stated that following the application of water coolant, the cooling rate increases, resulting in a shorter period to maintain the peak temperature after the weld. Consequently, the grain size decreased in HAZ and TMAZ (**Figure 4.24(b)**, **(d), (f),** and **(h))** of the WCFSW with and without interlayer.

4.3.2 Intermetallic behaviour

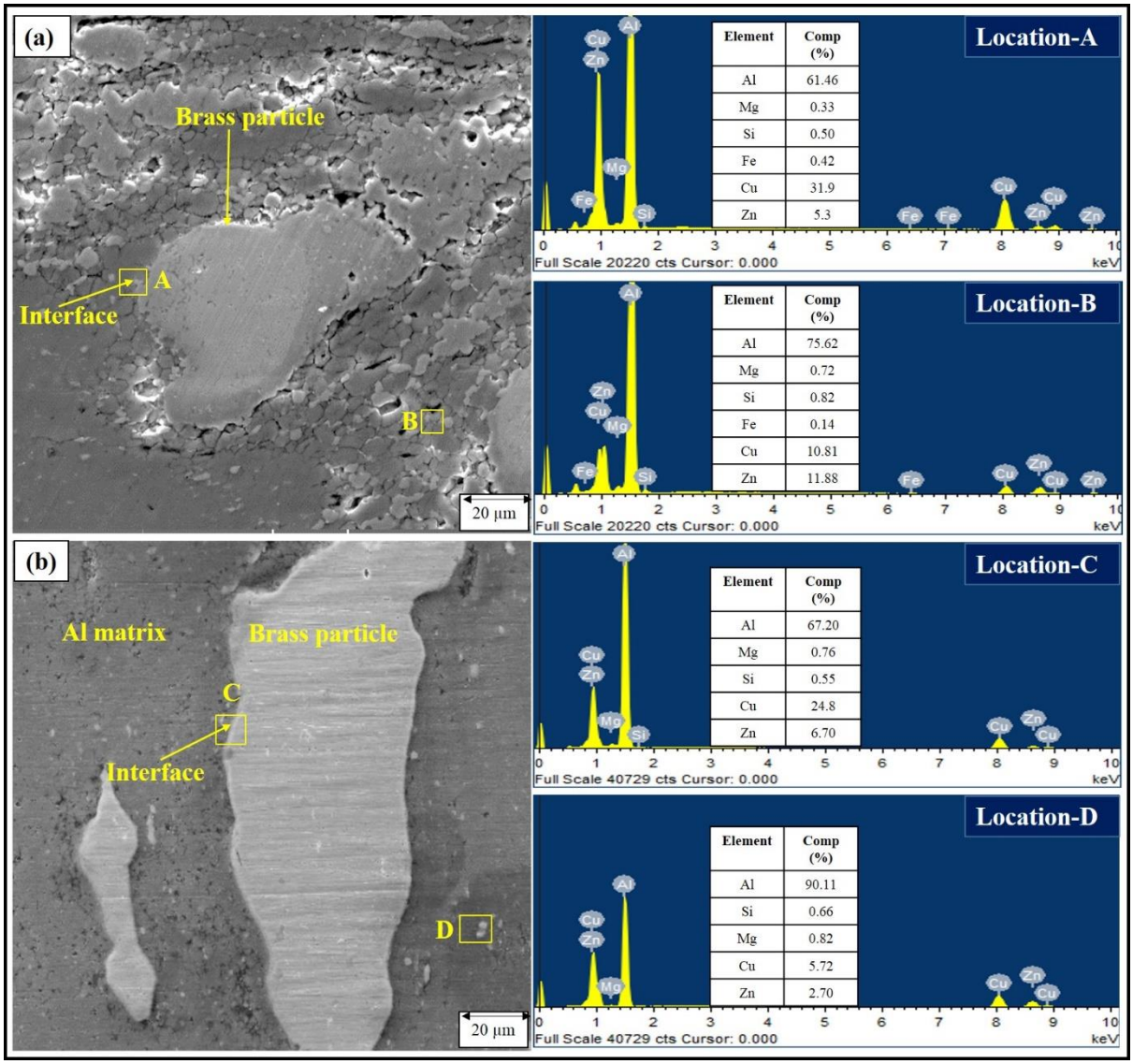

Figure 4.25 SEM and EDAX results of weld with interlayer of (a) NCFSW and (b) WCFSW

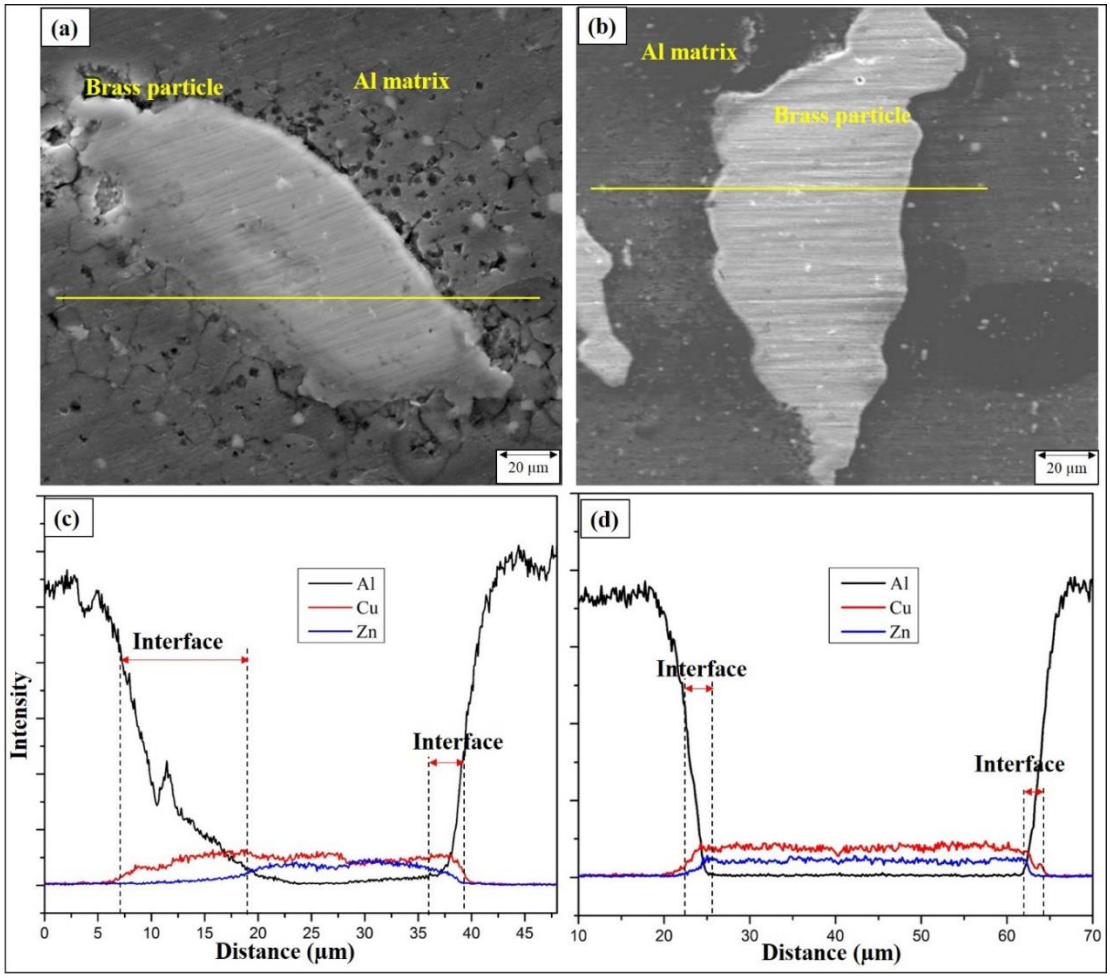

Figure 4.26 SEM images of weld with interlayer of (a) NCFSW, (b) WCFSW for line scan and corresponding EDAX line curves of (c) NCFSW and (d) WCFSW

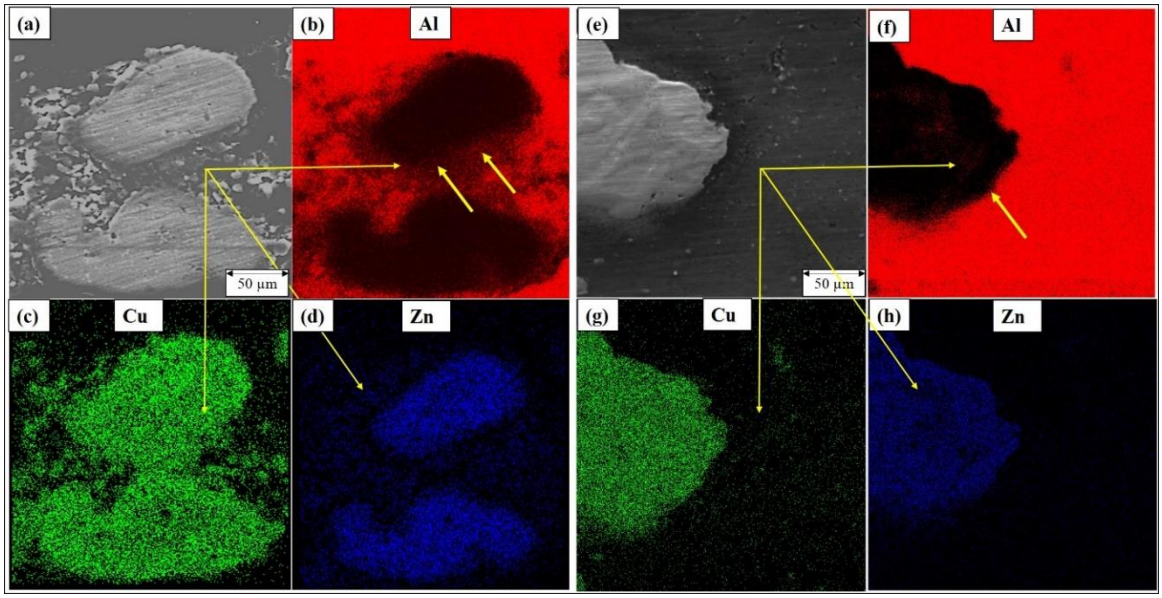

Figure 4.27 SEM images of weld with interlayer of (a) NCFSW, (e) WCFSW- corresponding EDAX maps of NCFSW (b-d) and WCFSW (f-h)

The intermetallic behaviour of welds with interlayer was studied using SEM and EDAX analysis for both cooling media, as depicted in **Figure 4.25**. SEM analysis revealed that brass particles and their fragments scattered and diffused in SZ as shown in **Figure 4.25(a)** and **(b)**. Microcracks and small voids at the interface were observed for NCFSW joint **(Figure 4.25(a))**. Smooth interface and no cracks or voids were obtained in WCFSW joint (**Figure 4.25(b)**). The presence of alloying elements and probable IMCs in the SZ of the weld joint under both cooling media was analyzed using EDAX analysis (**Figure 4.25**).

The variation in thickness of the Al-brass interface was observed for weld with interlayer under both cooling media. In order to confirm the interface thickness, a line was selected for EDAX scanning from left to right in the cross-section of SEM images of NCFSW and WCFSW joints as presented in **Figure 4.26(a)** and **(b)**, respectively. The corresponding elemental intensity curves are presented in **Figure 4.26(c)** and **(d)**. Diffusion, i.e., interface width in the curves, reveals that the brass particles reacted completely with the Al matrix. However, the thickness of the interface was much more for NCFSW (**Figure 4.26(c)**) than for WCFSW joint, as shown in curve **(Figure 4.26(d))**. To confirm the diffusion of brass particles in the Al matrix, EDAX maps were used, as shown in **Figure 4.27.** The small colour variation (black and red) near the interface, represented by arrows (**Figure 4.27(b)** and **(f)**), illustrates the interaction and diffusion of the two materials.

These images also confirm more thickness of interface (at arrows) for NCFSW (**Figure 4.27(b)**) compared to WCFSW welds (**Figure 4.27(f)**). During NCFSW, a large number of fragments were introduced into Al matrix, as observed in **Figure 4.27(a-d)**. However, during the WCFSW process, the density and size of brass fragments decreased, as shown in **Figure 4.27(e-h)**. The distribution of brass fragments such as Cu and Zn are indicated with green and purple colour, respectively. The high density of Cu and Zn were distributed in Al matrix for NCFSW **(Figure 4.27(c)** and **(d))**, while the fine and minimum number of fragments were distributed in WCFSW joint **(Figure 4.27(g)** and **(h))**. These results describe that coarse and high density of IMCs formed for the NCFSW joint, while fine and fewer IMCs were formed for WCFSW joint.

The diffusion of brass particles (**Figure 4.25(a)** and **(b))** in Al matrix is attributed to adequate material flow caused by enough heat generated, resulting in the formation of a composite-like structure. Moreover, the diffusion of brass particle is ascribed to the possibility of brass particle inter-diffusion with Al matrix at process temperature. IMCs may form at the interface of two dissimilar materials where diffusion is possible (Mokabberi et al. 2018). According to Al-Cu binary phase diagram, the simultaneous existence of Al and Cu in a system can result in the

formation of IMCs. (Esmaeili et al. 2011) reported that the FSW of Al to brass might result in the formation of IMCs through solid-state diffusion between Al matrix and brass particles. During FSW, the heat is generated due to friction between the working metals, and tool permits SZ to reach the eutectic temperature. Consequently, the melting at the grain boundary allows rapid diffusion of Al and brass atoms, and the rapid solidification results in the formation of IMCs (Patel et al. 2020).

The material flow causes mechanical mixing, high supersaturation of vacancies, and short circuit diffusion, resulting in an increase in the kinetics of IMC formation (Taillard et al. 2012). Generally, the diffusion of atoms in a crystalline lattice depends on a thermally activated process that can be substantially accelerated by defects such as dislocations and vacancies. The material experiences high strain rates during FSW, as high as 160 S^{-1} (Ramanjaneyulu et al. 2014). In this case, the vacancy concentration and dislocation increase, creating the path for the diffusion of atoms. Moreover, the dislocation lines can act as a path for the diffusion of atoms (Zhang, et al. 2021). IMCs may form on account of solid-state diffusion. The local thermal cycle and chemical composition influence the nature of IMCs formation, which are assisted by plastic deformation during FSW (Taillard et al. 2012). The macro cracks (**Figure 4.25(a)**) are due to the formation of hard and brittle IMCs. Continuous brittle IMCs at the interface obstruct the deformation through Al material movement, and thus ductility loss occurs in SZ. This may lead to crack formation while tool stirring for NCFSW, and the same results were observed by (Patel et al. 2020) and (Zhang et al. 2021). The rapid cooling rate in water resulted in suppression in the formation of brittle IMCs, leading to smooth interface (**Figure 4.25(b)**). The prolonged exposure of the interface at a higher temperature led to a more thickness of Al-brass interface (**Figure 4.26(c)**). The decrease in thickness is due to faster cooling rate and short exposure time at low temperatures, leading to thin layer IMCs. The water cooling contributed to a decrease in the thickness of Al-brass interface (**Figure 4.26(d)**). The occurrence of a thin diffusion layer hinted the presence of an effective joint formed between two matrices (Zhang et al. 2014). The water-cooling significantly reduced the peak temperature of WCFSW joint, minimized the growth and volume fractions of IMCs. The smooth interface with water-cooled FSWed dissimilar materials was also obtained by (Zhang et al. 2021). Furthermore, a thin diffusion interlayer describes the presence of an adequate metallurgical bonding between the two metals, i.e., brass and Al.

The EDAX spectra at the interface at points A-D (**Figure 4.25(a)** and **(b))** specify the presence of Cu and Zn elements. The weight ratio of Al to Cu at both points (A & C) is approximately

2, which is same as the weight ratio of Al_2Cu IMCs. Al_2Cu is a strengthening IMC, and the presence of such IMCs confirms good metallurgical bonding between Al matrix and brass particles. Additionally, a solid solution of Zn in the Al matrix may be formed as a result of the diffusion and dissolution of Zn atoms from brass particles in Al matrix (Mokabberi 2018). The occurrence of IMCs in the weld interface might impact the mechanical properties of the weld joint and provide a preferential route for crack propagation upon structure loading. Moreover, the mechanical properties of the weld joint strongly depend on the thickness of IMCs (Zhou et al. 2019).

Viscosity played a significant role in the distribution of large size Cu and Zn elements **(Figure 4.27(c)** and **(d))** in Al matrix. Since the peak temperature of NCFSW is higher than that of WCFSW, the viscosity of the material being welded was clearly lower than WCFSW. As a result, the lower viscosity of Al permitted the brass particles to mix more easily into it during NCFSW (Zhang et al. 2014). Another remarkable phenomenon in this study is that almost no Al matrix was stirred or diffused in the brass particles. This is because the melting point of brass fragments is higher than Al matrix, and the degree of softening for Al is higher than brass, i.e., the viscosity of Al is lower than brass. Thus it is easier for the brass fragments to be stirred into the Al matrix, and similar findings were observed by (Zhang et al. 2014).

The SEM images of the weld without interlayer of NCFSW and WCFSW are shown in **Figure 4.28.** A significant point in **Figure 4.28** is the size and distribution of precipitates. The fine precipitates along the grain boundaries were observed for the weld joint of WCFSW **(Figure 4.28(b))** than NCFSW, which showed coarser precipitates **(Figure 4.28(a))**. AA6061-T6 is a heat-treatable alloy, and Mg_2Si precipitates form in these alloys. Moreover, Mg_2Si precipitates were formed at all the weld conditions, and the same was reported by (Abdollahzadeh et al. 2021).

The EDAX results are presented in **Figure 4.28** (at locations A and B) showed the existence of Mg and Si elements, which could result from Mg_2Si precipitates. Generally, grain boundaries are the preferred sites for precipitate formation for weld without interlayer (**Figure 4.28**) under both cooling media (Abdollahzadeh et al. 2021). The volume percentage of grain boundaries increases as grain size decreases, increasing the number of precipitation sites. This is due to the fact that the size of precipitates reduces as the number of precipitates increases for a constant volume fraction of precipitates (Fathi et al. 2019). The severe plastic deformation and high heat generation under NCFSW led to grain growth and precipitates coarsening (**Figure 4.28(a)**). However, the faster cooling rate in WCFSW impeded the growth of grains

and precipitates (**Figure 4.28(b)**). The fine precipitates and grain refinement in SZ may improve tensile strength.

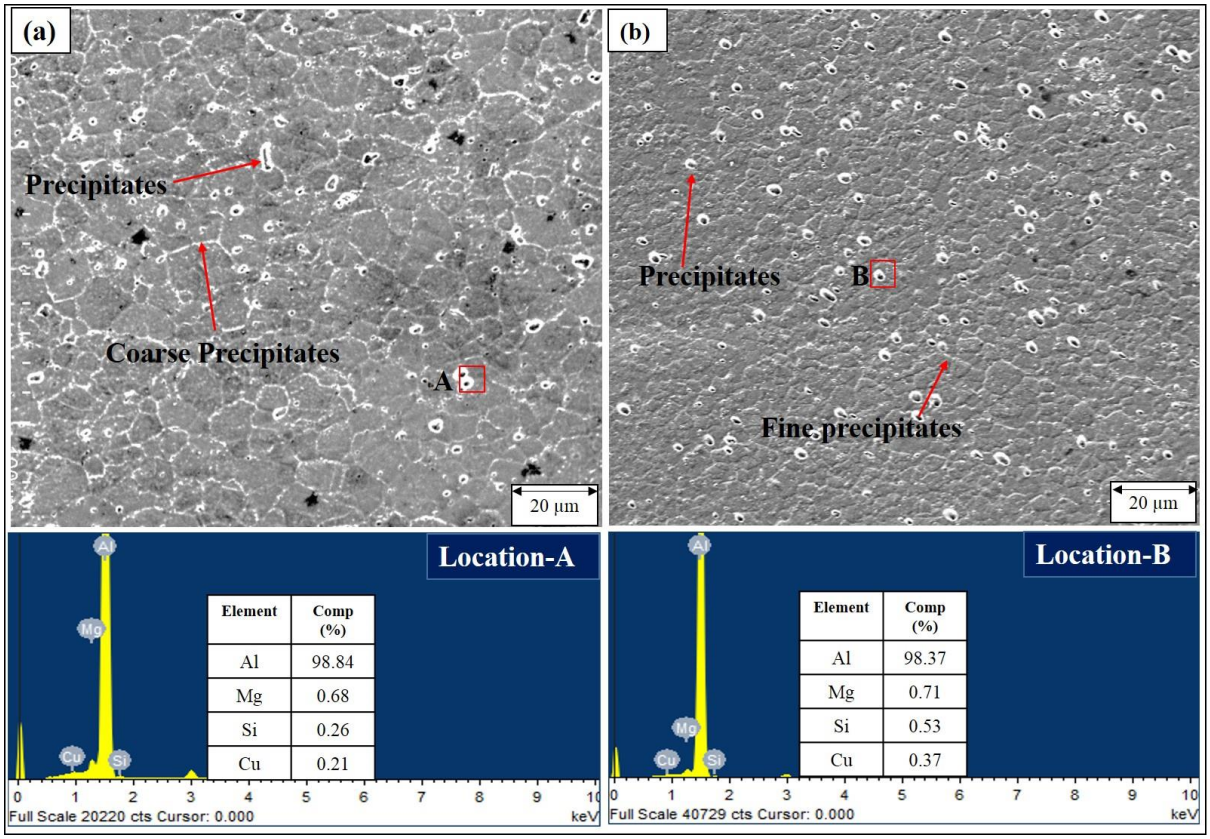

Figure 4.28 SEM and EDAX results at SZ of weld joints without interlayer (a) NCFSW and (b) WCFSW

4.3.3 Phase identification

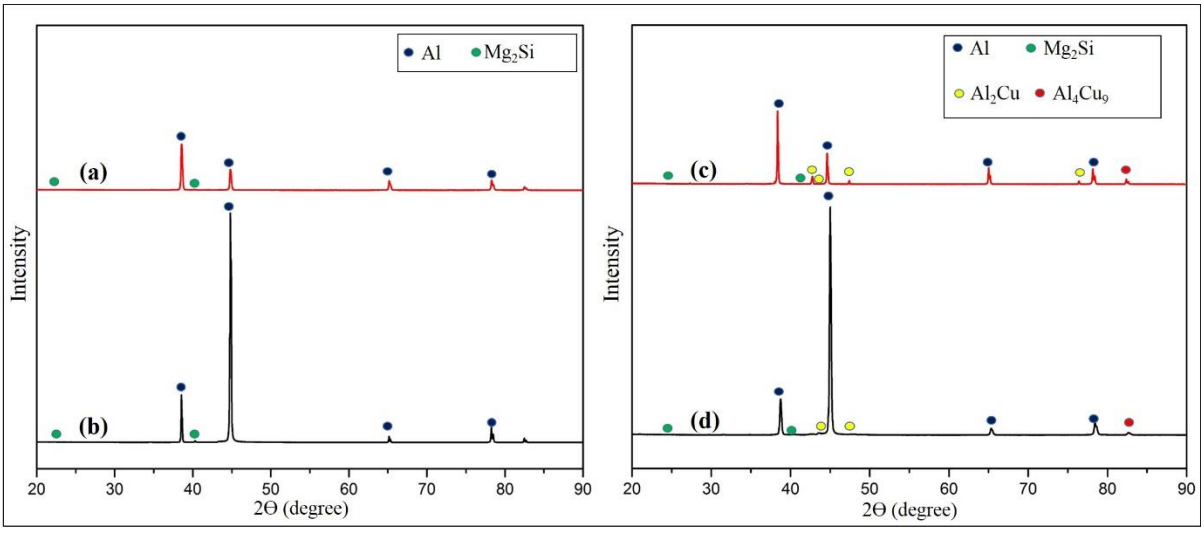

Figure 4.29 XRD plots of weld without interlayer of (a) NCFSW, (b) WCFSW and with interlayer of (c) NCFSW and (d) WCFSW.

The phases of IMCs were identified by XRD analysis. The XRD results of weld joints at SZ with and without interlayer under both cooling media are presented in **Figure 4.29**. XRD results illustrate the formation of high-density of strengthening IMCs such as Al_2Cu and Al_4Cu_9 in the spectrums of the NCFSW joint (**Figure 4.29(c)**). The high and more peaks of Al_2Cu were observed for the weld joint of NCFSW than for WCFSW. However, fewer intensity peaks of IMCs were observed in the spectrum of WCFSW **(Figure 4.29(d))**. From SEM and EDAX, it was apparent that WCFSW reduced the amount of brittle IMCs compared to NCFSW. For weld without interlayer of NCFSW and WCFSW, shown in **Figure 4.29(a)** and **(b)**, both the joints showed the formation of Mg_2Si strengthening IMCs. However, the difference in precipitate size and distribution was explained with SEM results **(Figure 4.28)**.

The possible formation of IMCs in Al-brass FSW is CuZn, AlCu, Al_2Cu, and Al_4Cu_9 (Esmaeili et al. 2011). Generally, Al_2Cu forms at a deformation temperature during FSW. The deformation temperature that occurs under both cooling media results in the formation of Al_2Cu IMCs, and the same kind of result were observed in FSWed Al-Cu dissimilar metals by (Mehta et al. 2017). The more dominating Al_2Cu IMC formation (**Figure 4.29(c)**) was attributed to enough heat generated, resulting in sufficient interaction between brass and Al matrix (Avettand-fènoël et al. 2020). Moreover, during NCFSW, plastic deformation and hot working lead to reach the eutectic temperature. In addition, a slower cooling rate occurs in NCFSW. These two reasons contributed to the growth of several IMCs. The reduced IMCs (**Figure 4.29(d)**) are due to the temperature-induced for WCFSW being lower than Al-brass eutectic temperature and faster cooling rate. Although the temperature-induced in WCFSW is low, some IMCs are still observed. The reasons include the density of lattice defect, and dislocation which can be increased by intense plastic deformation of the material that subsequently facilitates diffusion of atoms. Furthermore, the high impact of stirring may provide additional energy for Al-brass interaction (Zhang et al. 2014).

4.3.4 Grain structure analysis

The EBSD analysis was used to examine the grain structure in SZ to understand grain structure evolution during FSW. **Figure 4.30** shows EBSD (microstructure + inverted pole figure) images of FSWed joints under both cooling media. Based on misorientation angle distributions, the volume fraction of High Angle Grain Boundaries (HABs) for weld joints under both cooling media are represented in **Figure 4.31**. EBSD results consist of grain size, the fraction of Low Angle Grain Boundaries (LABs), and HABs, are documented in **Table 4.6**.

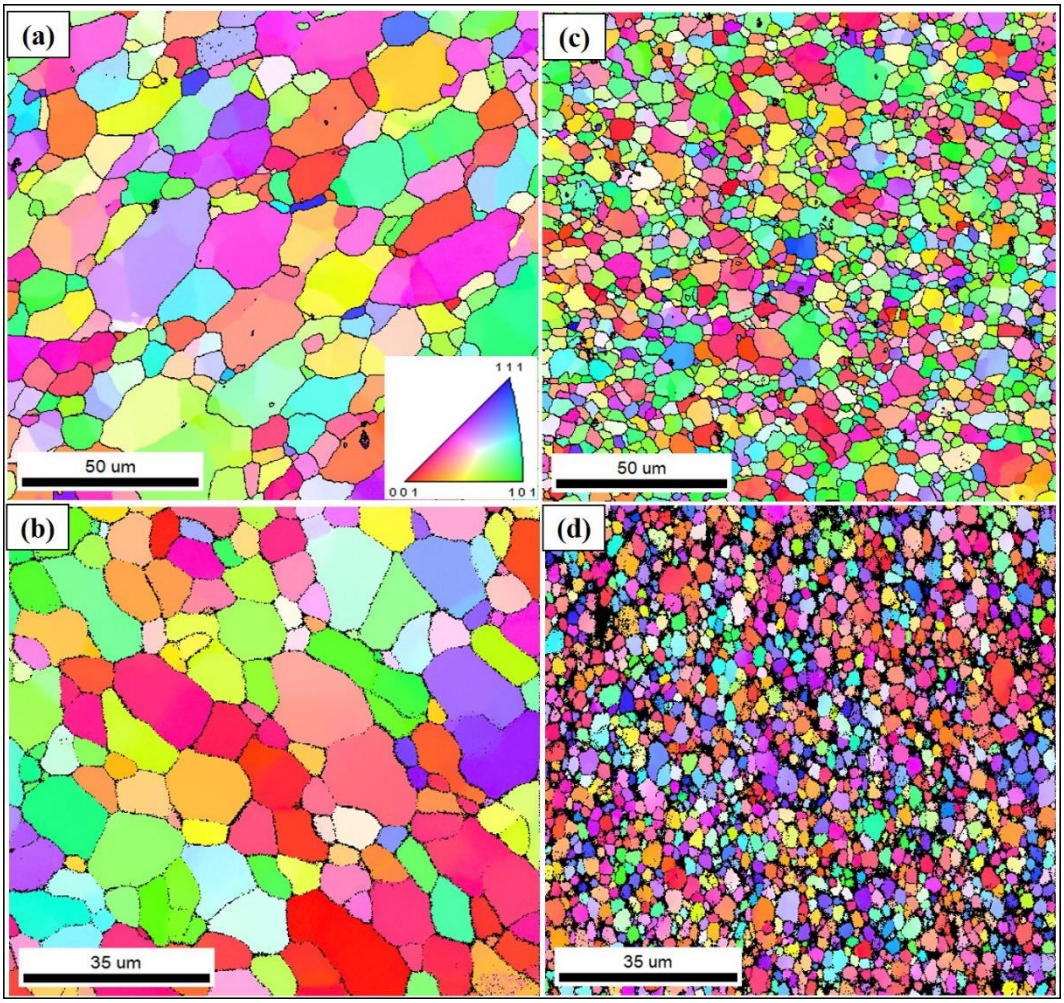

Figure 4.30 EBSD microstructure of weld without interlayer of (a) NCFSW, (b) WCFSW and with interlayer of (c) NCFSW, (d) WCFSW

Fine and equiaxed grains were obtained for all the weld joints. The NCFSW joint without interlayer consists of coarser grains (**Figure 4.30(a))** with a very low fraction of HABs **(Figure 4.31(a))**. Moreover, more grain refinement and increased fraction of HABs were observed for NCFSW with interlayer with the addition of brass interlayer **(Figure 4.30(c))** and **(Figure 4.31(c))**, respectively. The grain size decreased for WCFSW without interlayer **(Figure 4.30(b))** with an enhanced fraction of HABs **(Figure 4.31(b))** compared to NCFSW without interlayer. The WCFSW with interlayer showed the lowest grain size **(Figure 4.30(d))** with a high fraction of HABs **(Figure 4.31(d))** compared to the other samples.

The fine and equiaxed grains for all the weld joints were obtained due to Dynamic Recrystallization (DRX) during FSW. The primary grain refinement mechanism during FSW of Al alloys is DRX, strongly influenced by heat input and driven by Dynamic Recovery (DRV).

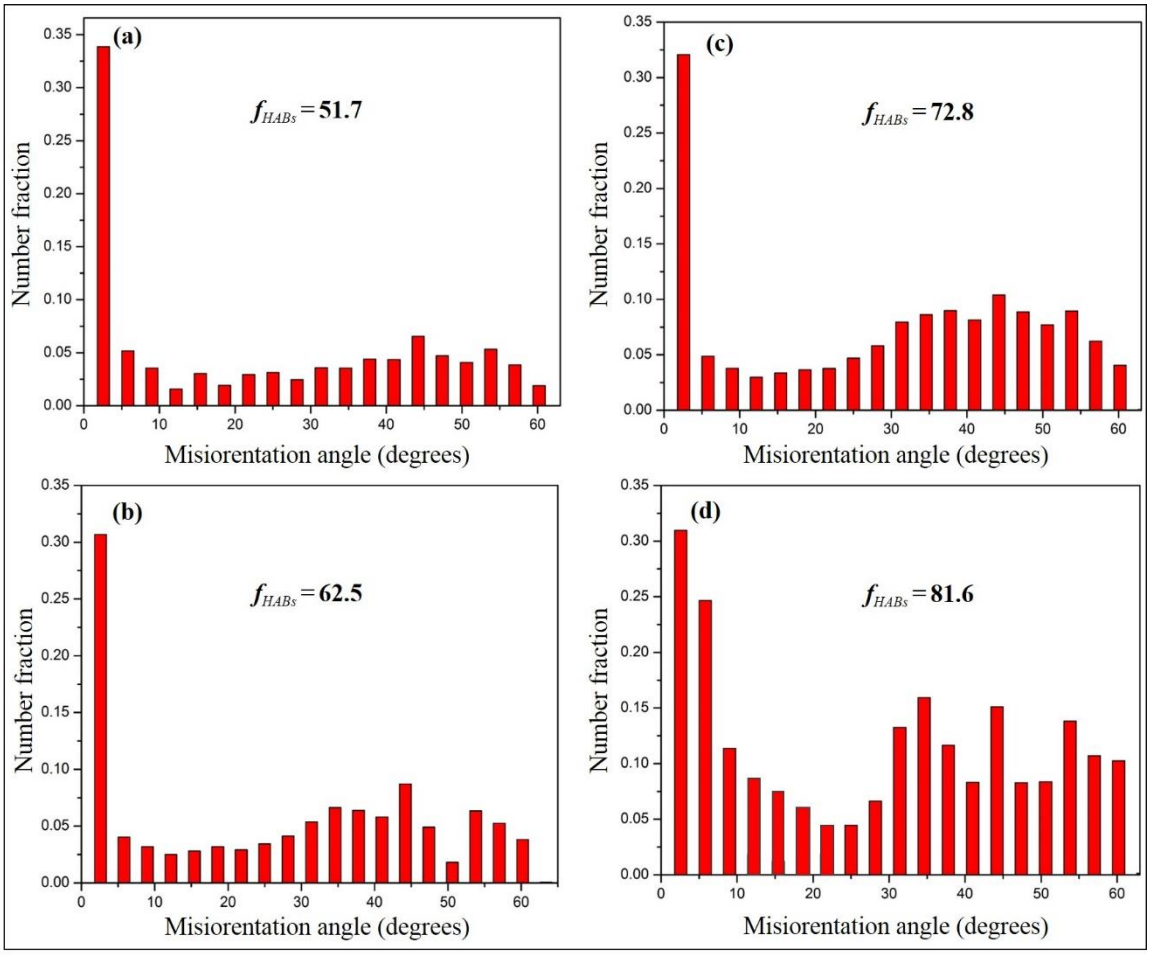

Figure 4.31 Misorientation angle distribution of welds without interlayer of (a) NCFSW, (b) WCFSW and without interlayer of (c) NCFSW, (d) WCFSW

Table 4.6 EBSD Result

Samples	Grain size (μm)	Fraction of grain boundaries (%)	
		LABs (<15°)	HABs (>15°)
NCFSW Without interlayer	5.2 ± 0.6	48.3	51.7
NCFSW With interlayer	2.3 ± 0.1	27.2	72.8
WCFSW without interlayer	4.2 ± 0.3	35.5	64.5
WCFSW with interlayer	1.6 ± 0.1	18.4	81.6

Moreover, Al alloys have a very high stacking fault energy, which favours the occurrence of DRX during DRV. DRV occurs predominantly in materials with a high stacking fault energy, such as Al alloys, where dislocations can cross slip, and climb between planes. Since alloying additions to Al have no noticeable impact on the stacking fault energy, DRV is predicted to predominate in Al alloys during hot deformation (Su et al. 2005), (Mcnelley et al. 2008). The

rotation of the tool during FSW results in mechanical deformation and heat generation in SZ. When the lattice structure is deformed, the strain energy in the lattice structure increases, resulting in lattice defects such as dislocations and point defects. The increase in deformation leads to produce more dislocations. As the density of dislocations increases, it starts to rearrange in the lattice structure (Mahto et al. 2021). DRV occurs when this large number of dislocations are rearranged, resulting in the formation of new subgrain boundaries within the major grains. The misorientation angle is small ($\Theta < 15^{o}$) for these boundaries, referred to as LABs. Due to the mechanical stirring action of the rotating tool, these types of grain boundaries vary continuously and rotate, increasing their misorientation angle. Thus, LABs are transformed into HABs ($\Theta > 15^{o}$), and as a consequence, fine grains develop in the microstructure (Su et al. 2005). Three mechanisms that contribute to the rotation of subgrain boundaries during the DRX process are subgrain growth, grain boundary lattice gliding, and lattice slip. Due to the high strain rate in FSW, lattice rotation with boundary slip does not occur. Moreover, grain growth is also not possible as the grain size of the FSWed joint is smaller than BM. Thus, the primary mechanism for the formation of DRX in FSW is lattice gliding (Biswas et al. 2012). The recrystallized grain size is dependent on the amount of heat applied, strain rate, and rate of cooling.

The coarse grains of NCFSW without interlayer (**Figure 4.30(a))** is due to the high heat-induced and the slower cooling past FSW, in NCFSW samples. As a result, sufficient energy and time are available for recrystallized grains to grow. Since the brass particles act as a nucleation site for further recrystallization during NCFSW with interlayer, resulting in small grains **(Figure 4.30(c))** than weld without interlayer. The decrease in grain size for NCFSW without interlayer **(Figure 4.30(b))** is due to faster cooling rate. Very fine grain for NCFSW with interlayer (**Figure 4.30(d)**) demonstrates that submersion in water results in finer microstructures than natural cooling. The grain size of WCFSW joint decreased due to heat being removed by flowing water over the weld joint during welding, which lowered the high-temperature retention period of the weld joint (Sinhmar et al. 2017). In addition, during WCFSW, the heat produced by friction is transmitted, resulting in faster cooling rate than at NCFSW, inhibiting grain growth. The increased fraction of HABs in WCFSW with interlayer **(Figure 4.31(d))** is due to the substantially higher fraction of recrystallization. The reason is that the material generates a significant number of dislocations and strain, and the stored dislocations easily drive recrystallization and recovery during the weld's cooling stage (Satyanarayana et al. 2021). The decrease in grain size of FSWed dissimilar joints under water cooling compared to natural cooling was also observed by other researchers (Mofid et al. 2012;

Patel et al. 2020).

4.3.5 Mechanical properties

4.3.5.1 Microhardness

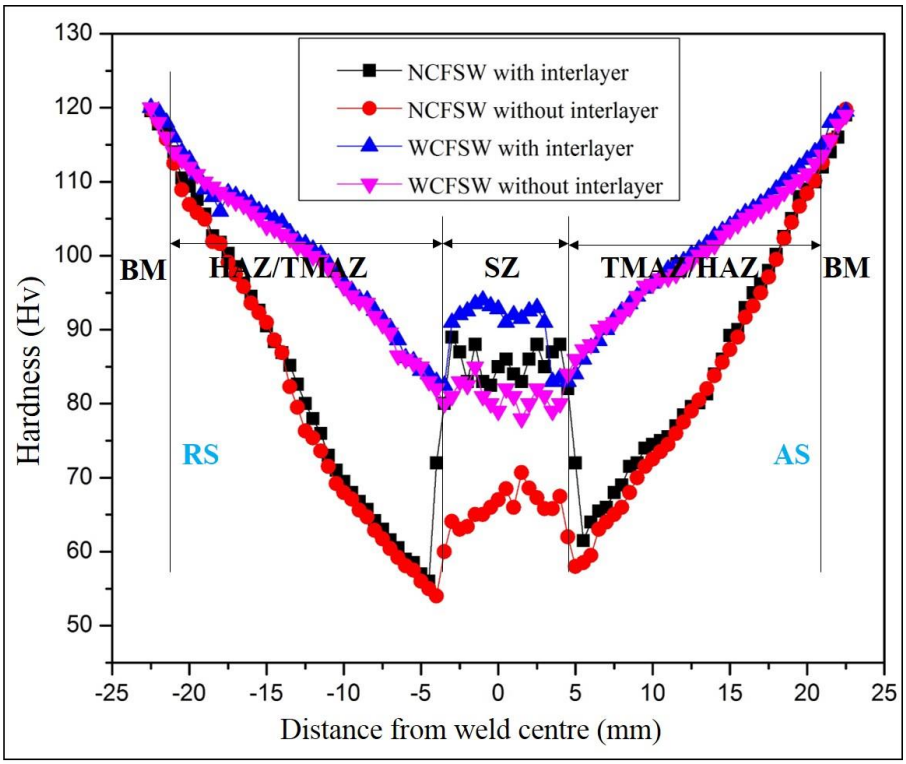

Figure 4.32 Hardness profile of the weld with and without interlayer of NCFSW and WCFSW joints

The hardness profiles of the welds under both cooling media are depicted in **Figure 4.32**. From **Figure 4.32**, the lowest hardness in SZ is observed for NCFSW without interlayer. The hardness in SZ improved for NCFSW weld with interlayer. However, the hardness in HAZ/TMAZ of NCFSW with and without interlayer is lower than SZ and observed to be the same. The WCFSW without interlayer improved hardness in SZ compared to NCFSW without interlayer. Moreover, WCFSW with interlayer showed the highest hardness in SZ compared to other weld samples. Moreover, significant hardness improvement of WCFSW in HAZ and TMAZ was observed for both welds with and without interlayer.

The hardness of the welds mainly depends on precipitation distribution, grain size, and dislocation density (Fathi et al. 2019). The reduced hardness in SZ of NCFSW without interlayer is attributed to precipitate dissolution, reduction of dislocation densities, and grain coarsening during FSW. The hardness in SZ improved for NCFSW joint with interlayer which

was on account of the formation of IMCs and the detachment of brass particles. The decrease in hardness of TMAZ/HAZ was attributed to grain coarsening and precipitate dissolution (**Figure 4.24(a)** and (**c)**) by high heat generation and slow cooling rate. The development of PFZ might also be a cause of decrease in the hardness of HAZ/TMAZ (Abdollahzadeh et al. 2021). The increase in hardness of WCFSW without interlayer is attributed to the reduction in dissolution of precipitates with water cooling. However, the water cooling suppressed the formation of IMCs, as explained in intermetallic behaviour section, the decrease in grain size caused an increase in the hardness of SZ. The increase in hardness for water-cooled dissimilar welding was also observed by (Mehta et al. 2017). The improvement of HAZ/TMAZ hardness for WCFSW with and without interlayer is attributed to water cooling, which reduced the peak temperature, thereby achieving grain refinement (**Figure 4.24(b)** and **(d)**) and preventing the thermal softening than NCFSW. Thus, WCFSW increased the hardness not only in SZ but also in HAZ and TMAZ. The increased hardness of HAZ can improve the tensile characteristics of the overall weld joint (Zhang et al. 2014).

4.3.5.2 Tensile results

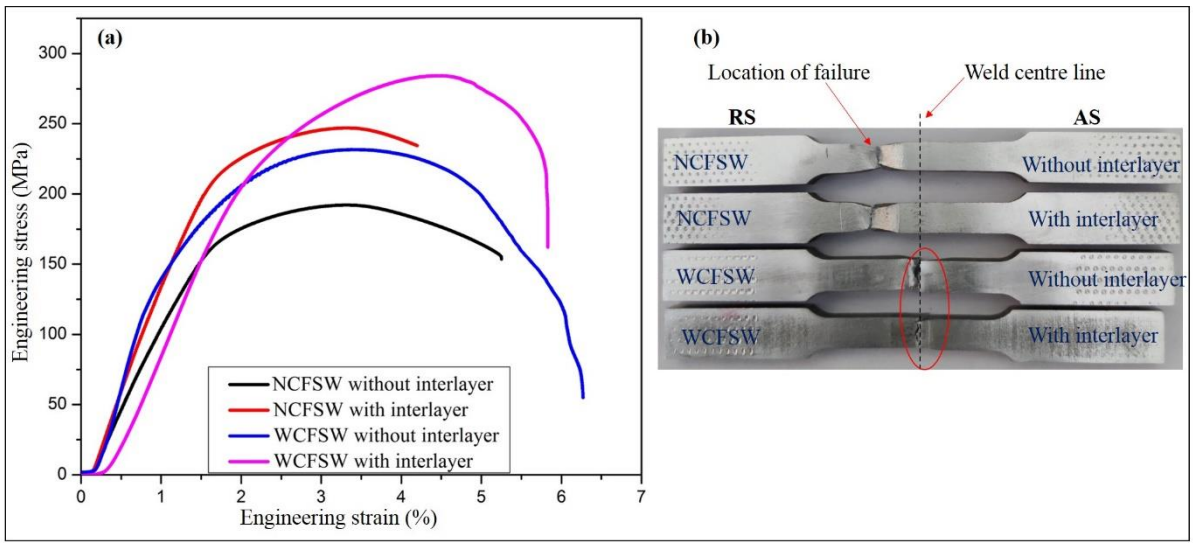

Figure 4.33 (a) Tensile curves of the weld joints and (b) Fractured transverse tensile samples of the welds.

The tensile curves of welds with and without interlayer under both cooling media are demonstrated in **Figure 4.33(a)**. The results of the tensile test are documented in **Table 4.7**. From **Figure 4.33(a)**, it was seen that lowest strength values were obtained for NCFSW without interlayer joint. The improved strength was observed for NCFSW with interlayer compared to NCFSW without interlayer.

Table 4.7 Tensile results

Weld media	UTS (MPa)	Y.S. (MPa)	E.L. (%)	Joint failure location
NCFSW without interlayer	192 ± 3	164 ± 3	5.2 ± 0.8	HAZ/TMAZ
NCFSW with interlayer	247 ± 4	210 ± 3	4.1 ± 0.3	HAZ/TMAZ
WCFSW without interlayer	231 ± 6	180 ± 3	6.3 ± 0.5	SZ
WCFSW with interlayer	284 ± 9	225 ± 5	5.8 ± 0.5	SZ

UTS: Ultimate tensile strength; **Y.S.**: Yield strength; **E.L.**: Elongation

The enhancement of strength and percentage of elongation was observed for WCFSW without interlayer in comparison to NCFSW without interlayer. The highest strength was obtained for WCFSW with interlayer than remaining weld conditions. The percentage of elongation also improved for WCFSW with interlayer compared to NCFSW. The tensile test specimens' failure locations are displayed in **Figure 4.33(b)**. The fracture morphology of welds with and without interlayer under both cooling media is displayed in **Figure 4.34**.

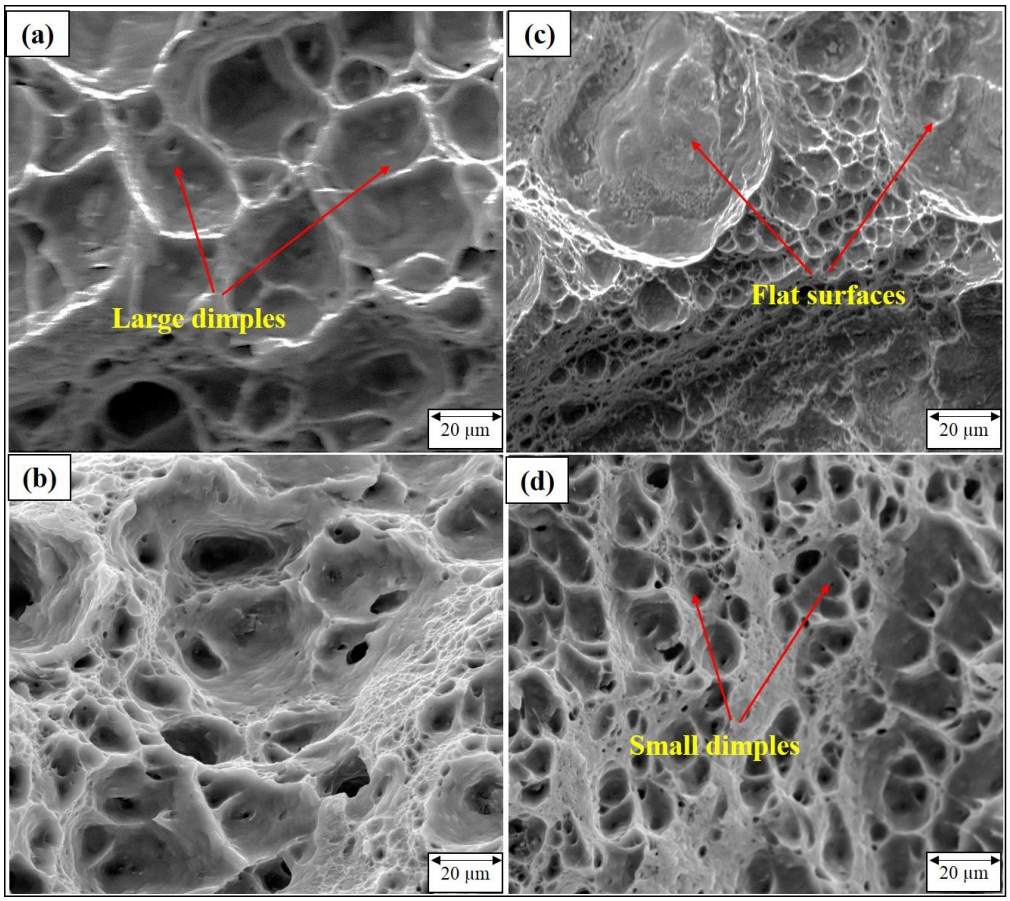

Figure 4.34 Fractography of weld without interlayer of (a) NCFSW, (b) WCFSW and weld with interlayer of (c) NCFSW, (d) WCFSW.

From **Figure 4.34**, it was observed that all the fractured samples showed dimples of various sizes. Large dimples were observed in the fracture surface of NCFSW joints (**Figure 4.34(a)**). Large dimples were observed on the joint fracture surface of the weld without interlayer under both cooling media **(Figure 4.34(a)** and **(b))**. Small dimples and flat surfaces were obtained for the weld with interlayer under both cooling media, as displayed in **Figure 4.34(c)** and **(d)**. The low strength in NCFSW without interlayer is attributed to precipitation dissolution and grain growth caused due to high thermal softening and slow cooling rate. The strength of the NCFSW joint with interlayer improved which could be ascribed to formation of strengthening IMCs such as Al_2Cu and Al_4Cu_9. A significant metallurgical interaction between Al and brass was occurred due to the formation of IMCs at the SZ. At the interface, this diffusion layer gradually mixes two materials (Brass and Al), avoiding major metallurgical differences that can deteriorate mechanical properties. The aspects mentioned above contributed to increase in strength of NCFSW with interlayer. However, NCFSW with interlayer exhibited lower elongation and better marginal strength than without interlayer. This is due to the brittle IMCs formation resulting from high heat generated during NCFSW. Since WCFSW without interlayer uses a low heat input, the precipitates are refined and uniformly dispersed throughout the matrix, resulting in a high density of precipitates. The fine precipitates and refined grains obstruct grain boundary movement, increasing joint strength than NCFSW without interlayer (Fathi et al. 2019) . Generally, brittle IMCs are the leading cause of cracks in NCFSW with interlayer since the fracture spreads predominantly through the brittle intermetallic layers. The cracks are inhibited in WCFSW with interlayer, resulting in higher strength than for NCFSW (Mehta et al. 2017). As a result, WCFSW with interlayer showed the highest strength compared other samples. This is due to the suppression of formation of IMCs, and accumulation of dislocations.

The percentage of elongation is improved for WCFSW with interlayer compared to NCFSW. This can be attributed to the finer and fewer IMCs, and accumulated dislocations distributed uniformly during the tensile test. As a result, the stress concentration would remain for a more extended period, and the joints can withstand higher deformation before breaking, resulting in more elongation. The improvement in elongation with water cooling FSWed dissimilar joint was also observed by (Chen et al. 2021). WCFSW without interlayer showed enhanced strength and ductility than NCFSW without interlayer due to the grain refinement caused by faster cooling rate. The volume fraction of grain boundaries increases as grain size decreases. Grain boundaries inhibit dislocation movement, resulting in increased strength and hardness. Additionally, the presence of more grain boundary area in fine-grained materials delays crack

propagation and improves ductility (Abdollahzadeh et al. 2021). Hence, both strength and ductility improved simultaneously for WCFSW with and without interlayer. In addition, the overall strength of WCFSW with interlayer enhanced due to the prevention of grain coarsening in HAZ/TMAZ with low temperature-induced by water cooling. Although the strength was enhanced, the weld joints of NCFSW and WCFSW with interlayer showed lower fracture to elongation than without interlayer. The two possible reasons for the low fracture to elongation were presented. (a) Because of its hard and brittle nature, the presence of a substantial number of IMCs decreased the fracture to elongation in NCFSW joint and (b) The WCFSW caused the formation of fine grain microstructure, which resulted in hard SZ, as a result of which low fracture to elongation ratio was obtained (Patel et al. 2020).

The NCFSW joints with and without interlayer were fractured at the interface of HAZ/TMAZ (**Figure 4.33(b)**) on the RS, where low hardness was recorded in HAZ/TMAZ. Generally, the minimum hardness zone of the joints is most sensitive to tensile fracture (Sinhmar et al. 2017). It was found that the results of fracture locations were in agreement with the microhardness profile. For NCFSW, low hardness was observed in HAZ due to grain coarsening and precipitate dissolution; therefore, failure occurred in HAZ. During FSW, the material flows from RS to AS. As a result, more brass particles accumulated at AS (**Figure 4.22(c)** and **(d)**), and the temperature-induced on RS is more. The high temperature causes greater dissolution of strengthening precipitates, and grain growth in HAZ/TMAZ. These are the reasons for failure of the samples in TMAZ/HAZ on RS for NCFSW with and without interlayer. WCFSW with and without interlayer joints fractured in SZ due to improved hardness in HAZ. The shifting of water-cooled weld fracture location towards weld center, i.e., SZ was also observed by (Sinhmar et al. 2017) and (Kumar et al. 2021).

Generally, in metals, dimples indicate a ductile fracture, and these are formed when dislocations interact. Dislocations can easily slide, climb, and cross-slip during the initial stages of deformation. Frank–Read sources and double-cross-slip multiplication are two mechanisms for dislocation development that can be activated by increased deformation. However, when the number of dislocations increases, their interaction results in dislocation lock that inhibit further dislocation slip. At this stage, increasing the applied force further results in the formation of voids at the lock locations. Voids expand and combine to form dimples, which eventually result in ductile fracture (Abdollahzadeh et al. 2021). Large dimples on the joint fracture surface of the weld without interlayer in both cooling media **(Figure 4.34(a)** and **(b))** indicate ductile fracture. Moreover, it is evident that significant plastic deformation was obtained during the tensile test. However, the dimple feature becomes ambiguous in WCFSW

without interlayer joint fracture surface. This implies a reduction in plastic deformation, and the same kind of fracture features was observed by (Fathi et al. 2019). Moreover, it demonstrates that adequate plastic deformation occurred for WCFSW without interlayer joints during the tensile test. This is because WCFSW without interlayer has high elongation. Small dimples and flat surfaces on the fracture surface of weld with interlayer under both cooling media (**Figure 4.34(c)** and **(d))** indicate ductile and brittle failure. However, WCFSW with interlayer showed ductile (**Figure 4.34(d)**) fracture compared NCFSW with interlayer, citing fewer IMCs generated during the weld.

4.3.6 Corrosion Analysis

4.3.6.1 PDP test:

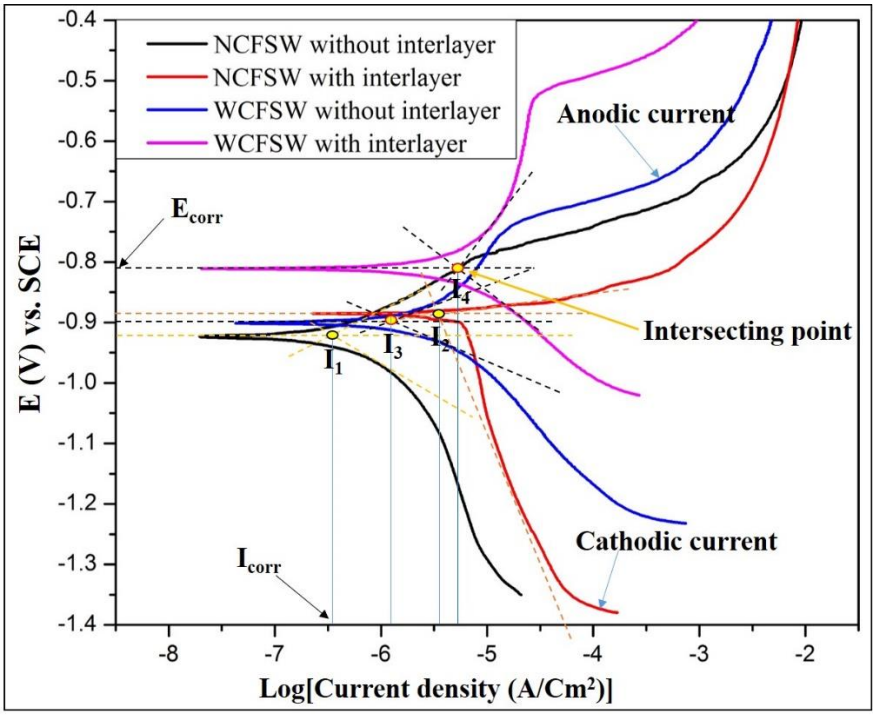

Figure 4.35. PDP curves of weld with and without interlayer of NCFSW and WCFSW

Table 4.8 Corrosion values

Weld condition	Corrosion potential E_{corr} (V (SCE))	Current density I_{corr} (A/Cm^2)
NCFSW without interlayer	-0.926	2.26×10^{-6} (I_1)
NCFSW with interlayer	-0.889	1.23×10^{-6} (I_2)
WCFSW without interlayer	-0.905	1.73×10^{-6} (I_3)
WCFSW with interlayer	-0.816	0.84×10^{-6} (I_4)

The PDP curves of the FSWed joints with and without interlayer under both cooling media are shown in **Figure 4.35**, produced by a steady-state polarization test. The Tafel fitting results of PDP curves, i.e., corrosion current density (I_{corr}) and corrosion potential (E_{corr}) values are documented in **Table 4.8.** Here, E_{corr} is the point corresponding to the tip of polarization curves, i.e., the point where the tangents of cathodic and anodic polarization curves intersect as represented in **Figure 4.35**. Furthermore, E_{corr} indicates the corrosion tendency of the samples, and I_{corr} values quantify the corrosion rate. A low corrosion potential (higher negative E_{corr} value) specifies poor corrosion resistance. Generally, a higher current density (high value of I_{corr}) indicates a higher corrosion rate. From PDP curves (**Figure 4.35)**, it was observed that low E_{corr} value (more negative) of NCFSW without interlayer indicates low corrosion resistance. The enhanced corrosion resistance of NCFSW with interlayer was observed compared to NCFSW without interlayer. However, WCFSW with interlayer showed better corrosion resistance than all weld joints.

The change in microstructural heterogeneity influences corrosion current density. The heterogeneity in the weld joint leads to macroscopic galvanic coupling, which accelerates the corrosion process (Xie et al. 2021). Moreover, the size of precipitates/IMCs plays a significant role in corrosion behaviour. The formation of IMCs influence E_{corr} and also I_{corr} values. Generally, corrosion occurs due to the potential difference between Al matrix and precipitates/IMCs. Galvanic corrosion occurs as the Al matrix acts as an anode and IMCs act as the cathode. The potential difference between IMCs and Al matrix is a motive force for galvanic corrosion, accelerating the cathodic and anodic reactions by transferring electrons from anode to cathode (Choi et al. 2019). The higher the potential difference, the more corrosion can occur. The coarser Mg_2Si precipitates formed in NCFSW joint without interlayer have more negative corrosion potential (E. et al. 2011). Hence, there is a more galvanic interaction between these precipitates and Al matrix, resulting in a reduction in corrosion resistance. The low E_{corr} of NCFSW with interlayer is attributed to the formation of Al_2Cu IMCs, which have low activation energy to initiate the corrosion process (Sinhmar et al. 2017). Moreover, Al_2Cu is the dominant IMC formed during weld with interlayer under both cooling media, as explained in intermetallic behaviour section. This specifies that the galvanic coupling between these IMCs and Al matrix is low, increasing corrosion resistance compared to NCFSW without interlayer. The WCFSW without interlayer resulted in fine precipitates and formed less galvanic interaction with Al matrix, resulting in better corrosion resistance than the NCFSW without interlayer. However, WCFSW with interlayer showed better corrosion resistance than all weld joints. This is ascribed to the decrease in volume fraction of IMCs such as Al_2Cu (as

explained in intermetallic behaviour section). The decrease in size and volume fraction of IMCs resulted in a decrease in the intensity of galvanic interaction. Thus, the corrosion attack was lower in case of WCFSW joint with interlayer. The fine distribution of Al_2Cu in SZ enhanced corrosion resistance, and a similar effect was observed by (Rao et al. 2010) and (Xu et al. 2020). I_{corr} values of WCFSW with interlayer are lower compared to remaining weld joints, indicating the reduced corrosion rate. Also, the higher values of I_{corr} indicate the possibility of pitting corrosion (Esther et al. 2014).

4.3.6.2 EIS test

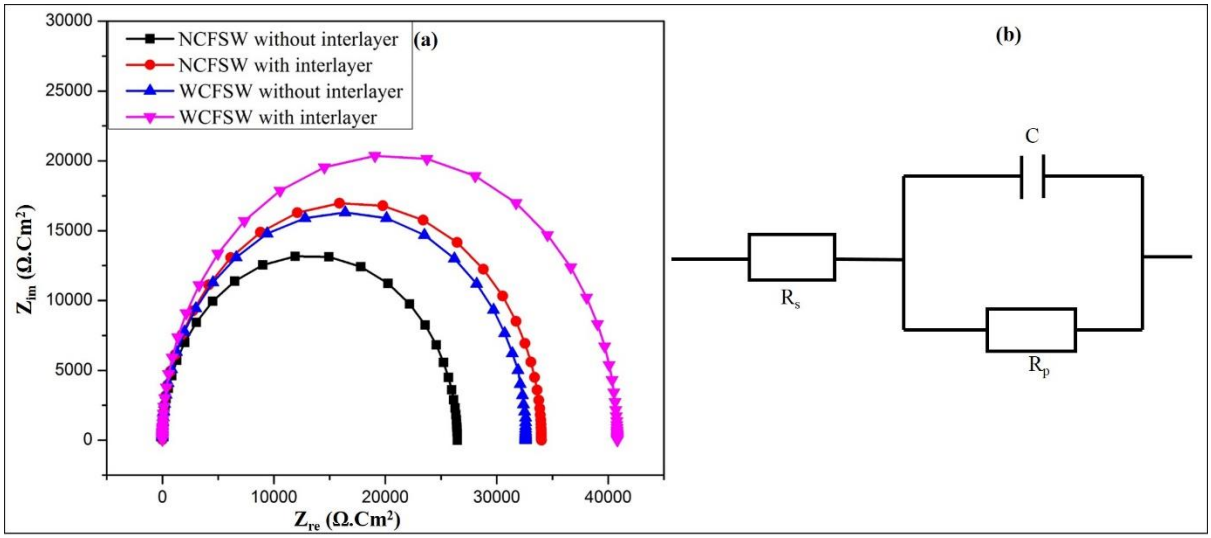

Figure 4.36 . (a) Typical Nyquist plot, (b) Equivalent circuit used for impedance data fitting.

Table 4.9 EIS data fitting results

Weld condition	R_s (Ω. cm^2)	C (μF. cm^{-2})	R_p (kΩ. cm^2)
NCFSW without interlayer	4.39	14.4×10^{-3}	26.07
NCFSW with interlayer	4.54	12.2×10^{-3}	33.75
WCFSW without interlayer	4.94	13.6×10^{-3}	32.15
WCFSW with interlayer	5.66	11.5×10^{-3}	40.50

The Nyquist plots of the EIS test weld joints under both cooling media are shown in **Figure 4.36(a)**. EIS data fit results are documented in **Table 4.9**. The corroded surface of weld samples under both cooling media is presented in **Figure 4.37**. The Nyquist plot consists of imaginary impedance (Z_{im}) on the y-axis and real impedance (Z_{re}) on the x-axis. An equivalent circuit termed Constant Phase Elements (CPE) was established to fit the EIS experimental plots as shown in **Figure 4.36(b)**. The data fit results are represented in terms of polarization resistance

(R_p), solution resistance (R_s), and capacitance (C). The EIS test produced R_s was nearly identical for all the weld joints and had a much lower value than R_p. The corrosion rate is the reciprocal of R_p, which specified that a higher value of R_p indicates a lower corrosion rate (Xie et al. 2021). The corroded surface of NCFSW without interlayer showed more corrosion attack with trenches and pits, as shown in **Figure 4.37(a)**. Only corrosion products were observed for NCFSW with interlayer as displayed in **Figure 4.37(c))**.

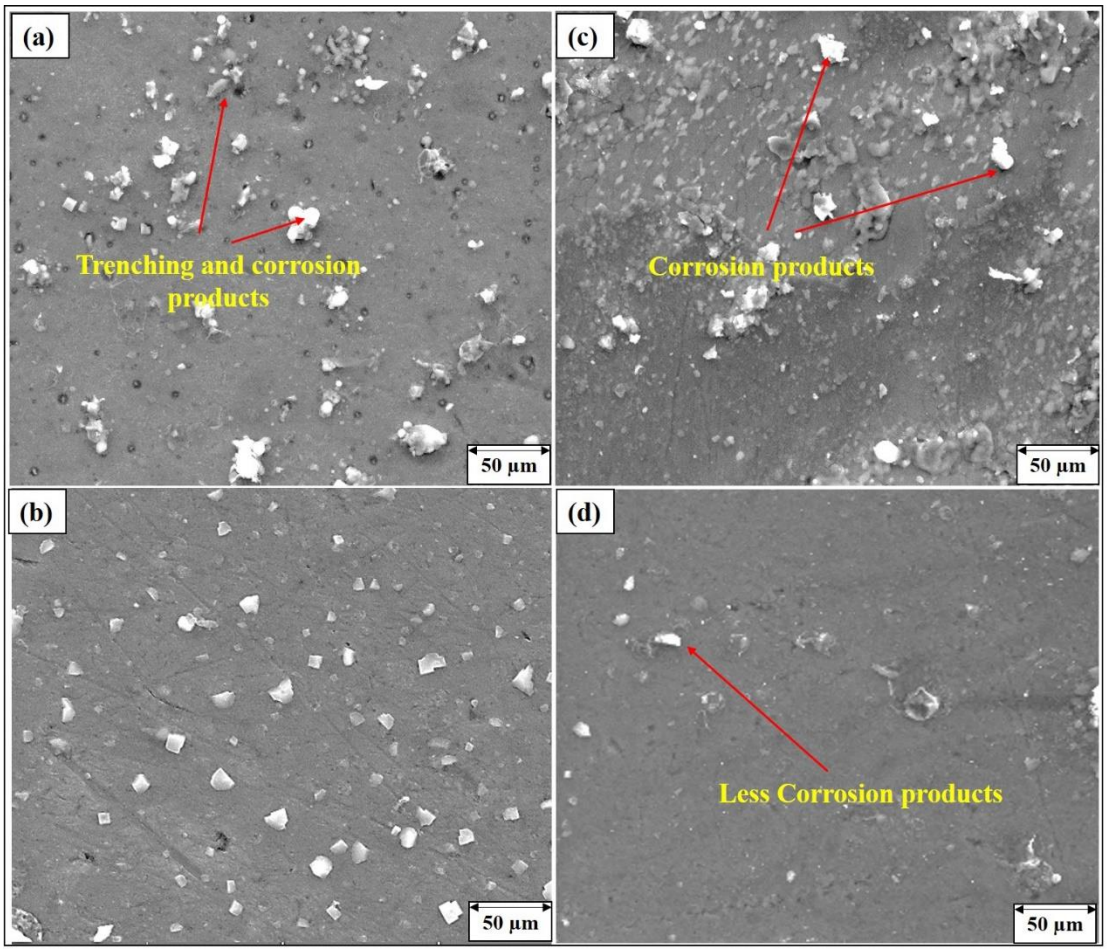

Figure 4.37 The corroded surface of the weld without interlayer of (a) NCFSW, (b) WCFSW and weld with interlayer of (c) NCFSW (d) WCFSW.

However, few corrosion products were observed for WCFSW without interlayer, as shown in **Figure 4.37(b)**. The WCFSW with interlayer showed very few corrosion products, as shown in **Figure 4.37(d)**. A higher value of R_p was observed for WCFSW with interlayer joints, which specifies lower corrosion rate than for all other weld joints. As the C value increases, the diffusion rate increases, leading to an increase in corrosion rate. The Nyquist plot shows a couple of high capacitive loops/semi-circles with identical shapes. This indicates a similar corrosion mechanism with only minor differences in impedance magnitude. However, corrosion resistance is related to the semi-circle diameter produced in the Nyquist plot. The

bigger diameter of the semi-circle indicates high corrosion resistance than smaller diameter semi-circle. The WCFSW with interlayer showed a larger diameter. This describes corrosion resistance of WCFSW with interlayer better than other weld joints. According to the results of PDP and EIS studies, it was observed that WCFSW with interlayer showed the highest corrosion resistance, and the NCFSW without interlayer showed the lowest corrosion resistance. The results of the PDP test match those of the impedance test.

At the beginning of the corrosion process, Al matrix around the precipitates dissolves and forms trenches. As the process continues, after some time the precipitates themselves dissolve, leading to potential changes in pit formation. Due to higher negative value of Mg_2Si precipitates, which dissolve more rapidly than Al matrix, there were more corrosion products and trenches (**Figure 4.37(a)**). Undissolved IMCs led to reduced galvanic interaction between Al_2Cu IMCs and Al matrix. Consequently, only corrosion products are formed on the surface of the NCFSW weld with interlayer (**Figure 4.37(c)**). However, the pits do not form for WCFSW without interlayer (**Figure 4.37(b))** due to the fine precipitates. Very few corrosion products on WCFSW with interlayer (**Figure 4.37(d))** attributed to the suppression of formation of IMCs. The above-explained type of corrosion attack suggests that the corrosion occurs typically in zones adjacent to IMCs/precipitates. The decrease in IMCs in SZ caused a decrease in the intensity of the galvanic cell formed between IMCs and Al matrix, resulting in less corrosive attack, and a similar corrosion attack was observed by (Xu et al. 2020).

4.4 Damping capacity and wear characteristics of welds with and without interlayer of natural cooling and water cooling

4.4.1 Frequency-dependent damping

Frequency-dependent damping capacity of weld samples and BM are displayed in **Figure 4.38**. The dislocation density of BM and weld samples are documented in **Table 4.10**. The damping capacity decreased marginally with increased frequency, and a similar trend was observed for all weld conditions. The inherent damping of a material is determined by composition of the material and the phases that are present. Although the overall composition is same before and after welding, a phase transition occurs after welding, which can be described as the dissolving of the precipitate phase, which causes a change in the matrix's composition. The decrease in grain size or grain boundary area increase might be attributable to the higher damping immediately after friction stir welding. The dislocation density is decreased after welding **(Table 4.10)** due to the high heat generated during FSW. Ignoring the effect of decrease in

dislocation densities since it is anticipated to have a minimal impact and also requires further investigation. Moreover, the damping capacity depends on various mechanisms such as interface, inherent, dislocation, and grain boundary damping.

Table 4.10 Grain size and dislocation densities.

Sample	Grain size (μm)	Dislocation density (ρ) $\times 10^{-6}$ (m/m^3)
BM	28.1 ± 3.1	13.64
NC without interlayer	5.2 ± 0.6	8.95
NC with interlayer	2.3 ± 0.1	9.23
WC with interlayer	1.6 ± 0.1	16.52

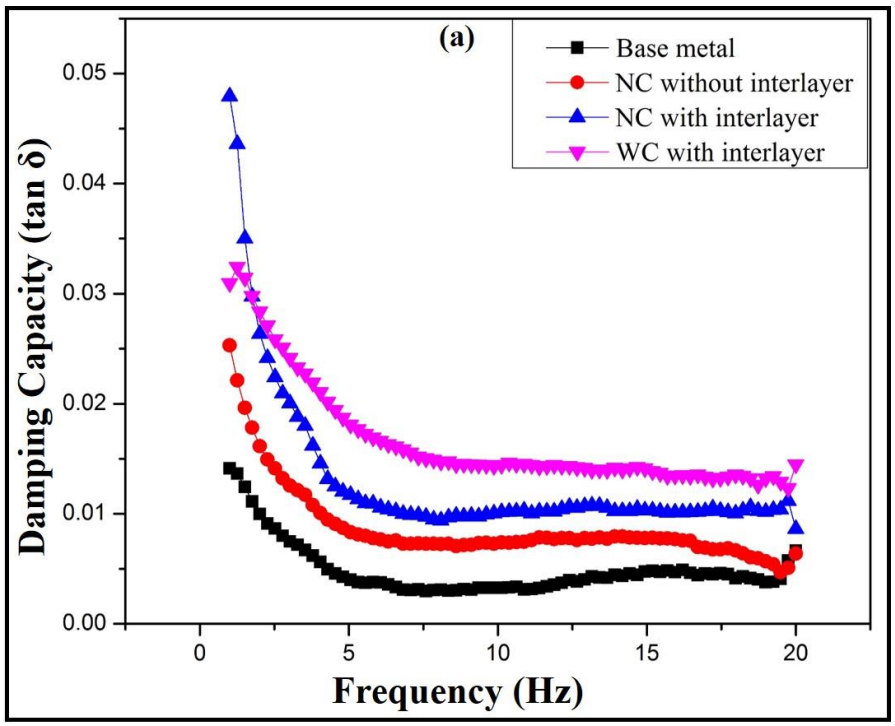

Figure 4.38 Frequency dependent-damping capacity of welds

From **Figure 4.38**, it was observed that the weld samples showed better damping capacity than BM, attributed to grain refinement. The decrease in grain size increased grain boundary area. Hence the damping capacity is enhanced after FSW. Moreover, the addition of brass interlayer enhanced the damping capacity compared to without interlayer. The following equation (2) is used to predict the damping capacity of composites, according to Wolfenden and Wolla (Venkateswara Reddy et al. 2020).

$$\eta_C = \eta_p V_p + \eta_m V_m + \eta_i V_i \quad (2)$$

Where η_C, η_p, η_m, and η_i are damping capacities of composite, particle, matrix, and interface, respectively. The weld with interlayer is treated as a composite consisting of Al as matrix and brass as reinforcement particles. Generally, the inherent damping capacity of brass is higher than Al matrix (Zhang et al. 1993). Thereby, the weld with interlayer increased the damping capacity. Here, the effect of dislocation densities was neglected because grain boundary and composite formation are the primary factors of enhanced damping capacity, and the same was reported by (Venkateswara Reddy et al. 2020). Moreover, WC weld with interlayer exhibited higher damping capacity than other weld joints due to suppression in the formation of IMCs. The decrease in IMCs improved the mobility of grain boundaries, thereby enhancing the damping capacity.

Furthermore, the proportion of interface, i.e., matrix-reinforcement interface, improves as the reinforcement fraction increases. The interfaces are two-dimensional flaws that move in response to dynamic loads and increase damping. Schoeck theory can also explain the contribution of interfaces to damping (Q^{-1}- quality inverse factor or damping capacity) (Perez et al. 1993).

$$Q^{-1} = 4.5(1-\nu)^2/(2-\nu) \times Vf$$

Where ν: Poisson's ratio, Vf: volume fraction of particles. This relationship demonstrates that the interfacial damping is precisely related to the volume percentage of reinforcement particles.

4.4.2 Temperature-dependent damping

The temperature-dependent damping capacity of welds is represented in **Figure 4.39**. Damping increases as the temperature increases. BM showed poor damping due to coarser grains. Weld samples exhibited better damping capacity than BM. The ease of grain boundary movement at high temperatures, especially when subjected to external stress, helps energy dissipation and enhances damping. Moreover, WC weld with interlayer exhibited more temperature-dependent damping due to the fine grains than the remaining weld samples. As a result, grain size and interface boundaries were assumed to be much more essential than dislocations to enhance high-temperature damping. Grain boundaries are the key factor influencing high-temperature damping (Reddy et al. 2022), and the same was observed in the current study.

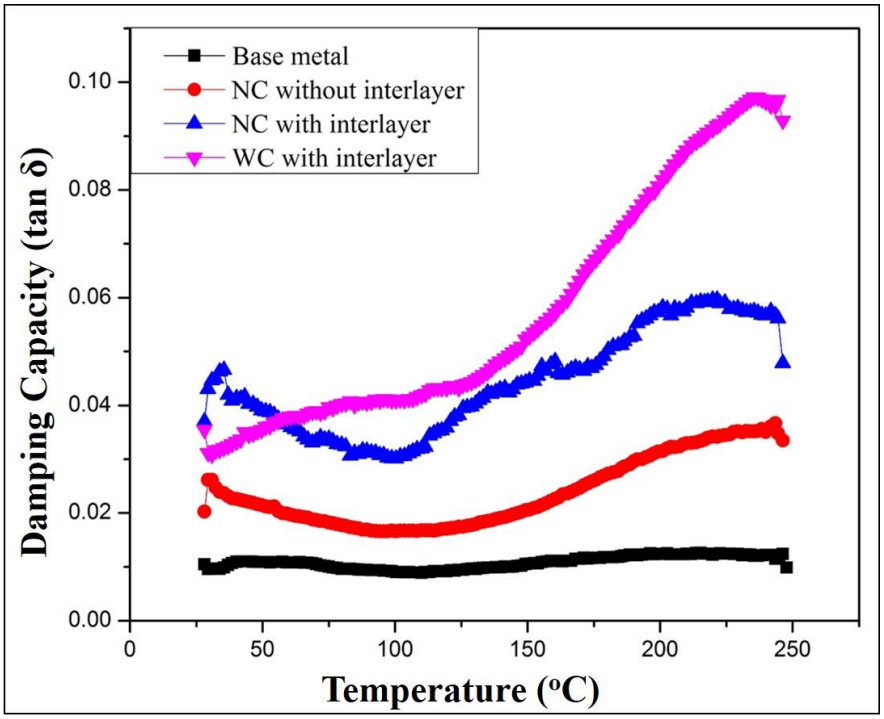

Figure 4.39 Temperature-dependent Damping capacity of welds

4.4.3 Storage modulus and loss modulus

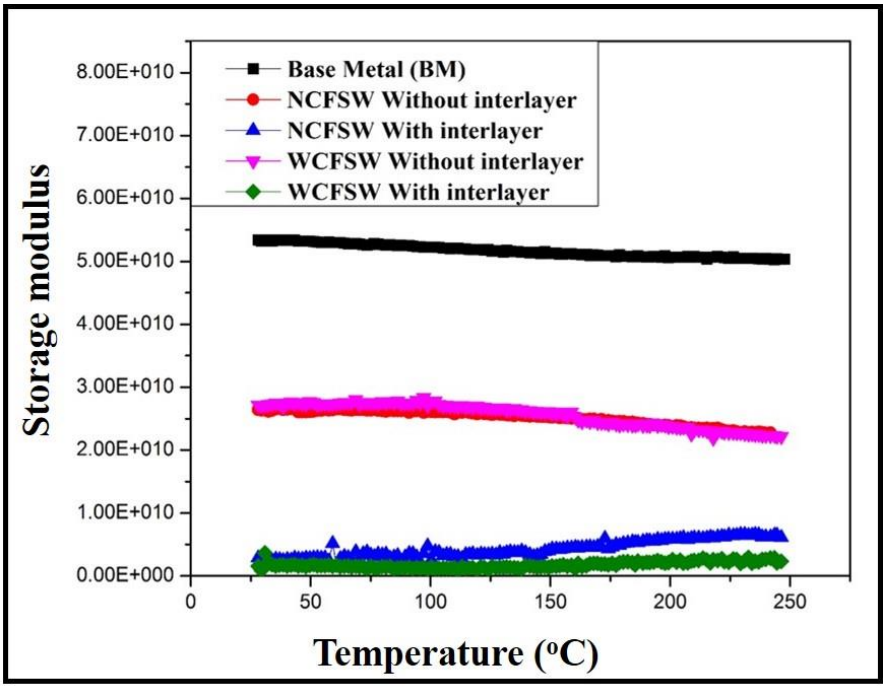

Figure 4.40 Storage modulus of welds

The damping capacity is the ratio between the loss modulus and the storage modulus. This relationship indicates that an increase in loss modulus or a reduction in storage modulus will increase damping. The decrease in storage modulus for weld with interlayer is noticeable in

Figure 4.40. WC weld with interlayer showed low storage modulus. The drop in bond strength caused by a rise in temperature affects the storage modulus (Rojas et al. 2012). On the other hand, the temperature dependence of loss modulus is the same as the temperature-dependent damping capacity (**Figure 4.39)**.

4.4.4 Wear characteristics

Wear tests were performed for welding with and without interlayer under both cooling media and base metal before welding. The coefficient of friction (COF) under 30 N load is displayed in **Figure 4.41**.

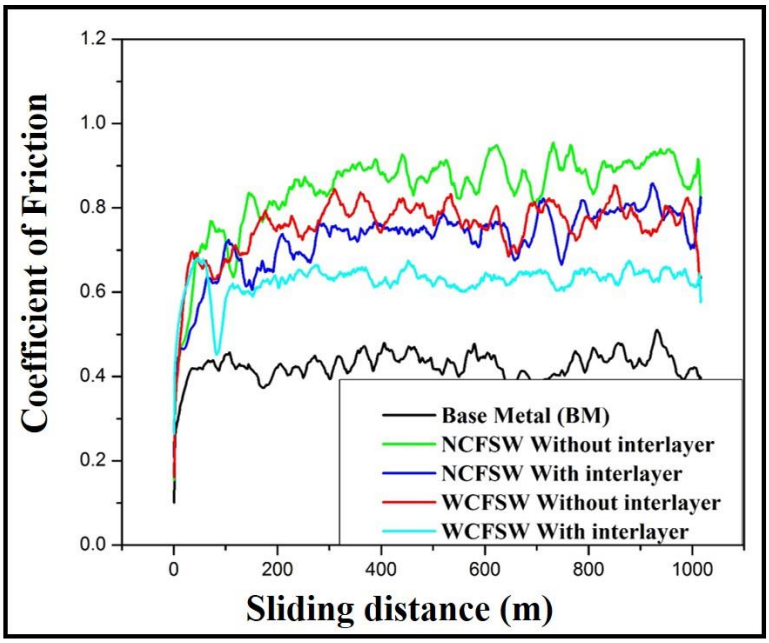

Figure 4.41 Variation of coefficient of friction with sliding distance

From **Figure 4.41**, it is observed that all samples have undergone a sliding mechanism with a low friction coefficient at starting distances, after which they achieve a steady-state condition. The wear rate of all the samples under 30N is presented in **Figure 4.42.** Usually, the friction test results are consistent with the microhardness test, and their causes may be identical. Lower COF of weld with interlayer sample is attributed to incorporating brass particles in the SZ, which lowers COF by enhancing matrix hardness and bearing capacity. **Table 4.11** summarises the wear characteristics of the BM and weld samples subjected to various loads. As per the results, the mean COF and wear rate of BM is the lowest, and those of weld without interlayer are the highest. The low COF and wear rate of weld with interlayer compared to without interlayer may be attributable to the lubricating effect of brass particles (Palanivel et al. 2016). In addition, the COF of samples subjected to a higher applied load is higher due to the increase

in contact force and nominal contact areas. In addition, all samples lose greater weight as the load increases.

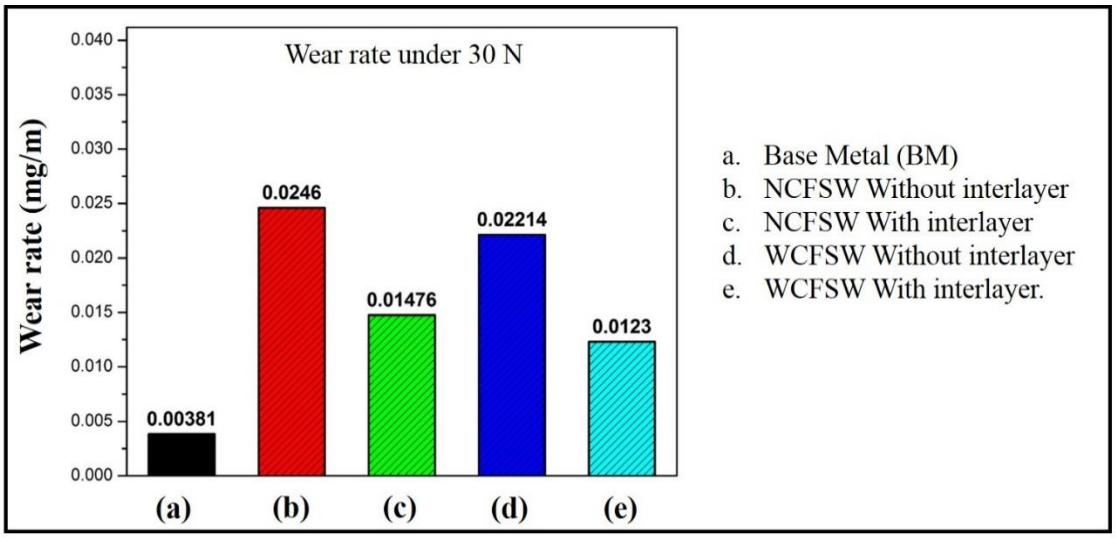

Figure 4.42 Wear rate of weld samples under 30 N load

Figure 4.43 shows the comparison of the wear rate of all samples. From **Figure 4.43**, it can be observed that the weight loss at 50 N is greater due to a larger friction resistance between the samples and the corresponding surface. Furthermore, at this force, higher frictional resistance produces an increase in temperature as well as a reduction in hardness and wear resistance (Huang et al. 2018).

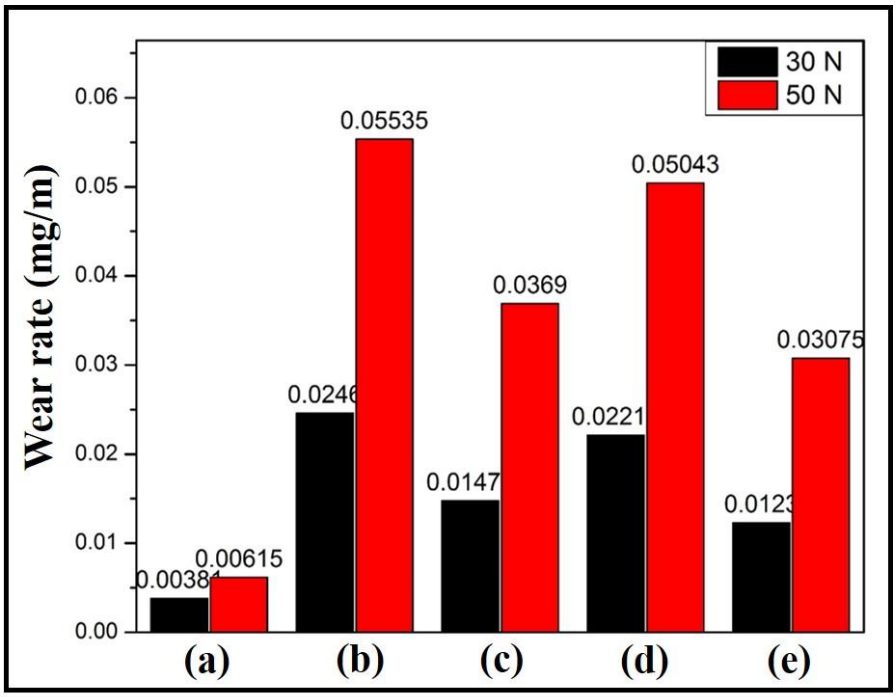

Figure 4.43 Comparison of wear rate of weld samples under 30 N and 50 N load.

Table 4.11 Wear test results

	Coefficient of friction (COF)		Wear rate (mg/m)	
Sample	30 N	50 N	30 N	50 N
BM	0.426	0.520	0.0038	0.0061
NC without interlayer	0.845	0.901	0.0246	0.0553
NC with interlayer	0.726	0.862	0.0147	0.0369
WC without interlayer	0.757	0.845	0.0221	0.0504
WC with interlayer	0.628	0.743	0.0123	0.0307

4.4.4.1 Wear morphology

The SEM images of worn surfaces of BM and weld samples under 30 N and 50 N load is displayed in **Figure 4.44** and **4.45**, respectively. The degree of delamination, debris, fractures, and craters varies amongst samples. Plastic deformation of the surfaces, the appearance of delamination, and craters are the characteristics of adhesive wear that are more prominent on the surface of worn welds without interlayer (**Figure 4.44(b)** and **(d)**). Due to thermal softening after FSW, welds without an interlayer exhibit more plastic deformation and are softer than the base metal. The weld surface with interlayer under both cooling media shows low and shallow wear features (**Figure 4.44(c)** and **(e)**). However, the higher wear resistance, scratch marks and sliding directions are more prominent. This can be ascribed to the brass particles' reinforcing effect, which improves the material's resistance to wear. By analyzing the wear characteristics (**Figure 4.44**), it can be determined that the hard reinforcing particles in the weld with interlayer sample function as load-bearing and offer strong resistance to delamination, resulting in a lower rate of material removal (Anvari et al. 2013). The worn surface of WC weld without interlayer exhibits localized plastic deformation and the production of shallow grooves.

For WC weld with interlayer, plastic deformation nearly disappears, and sliding tracks are observed owing to the formation of finer Al_2Cu IMCs and uniform dispersion of brass particles. It is important to note that the grooves generated in weld with interlayer during sliding wear are quite shallow, which may be attributable to the two considerations listed below. First, the formation of Al_2Cu and exhibit superior interface bonding with the Al matrix. In this instance, only a limited number of Al_2Cu particles are shattered and separated from the Al matrix due to the excellent interface bonding, which permits the load to travel across the particle/matrix interface and then function as an abrasive particle (Alishavandi et al. 2020).

Second, formed Al_2Cu particles with high hardness can act as a barrier to prevent the abrasive particle from scratching and ploughing. These two mechanisms result in the development of shallow grooves in weld with interlayer. Based on the preceding study, it is acceptable to conclude that these formed Al_2Cu particles have restricted matrix plastic deformation, resulting in a gradual transition of wear mode from adhesive to adhesive and delamination.

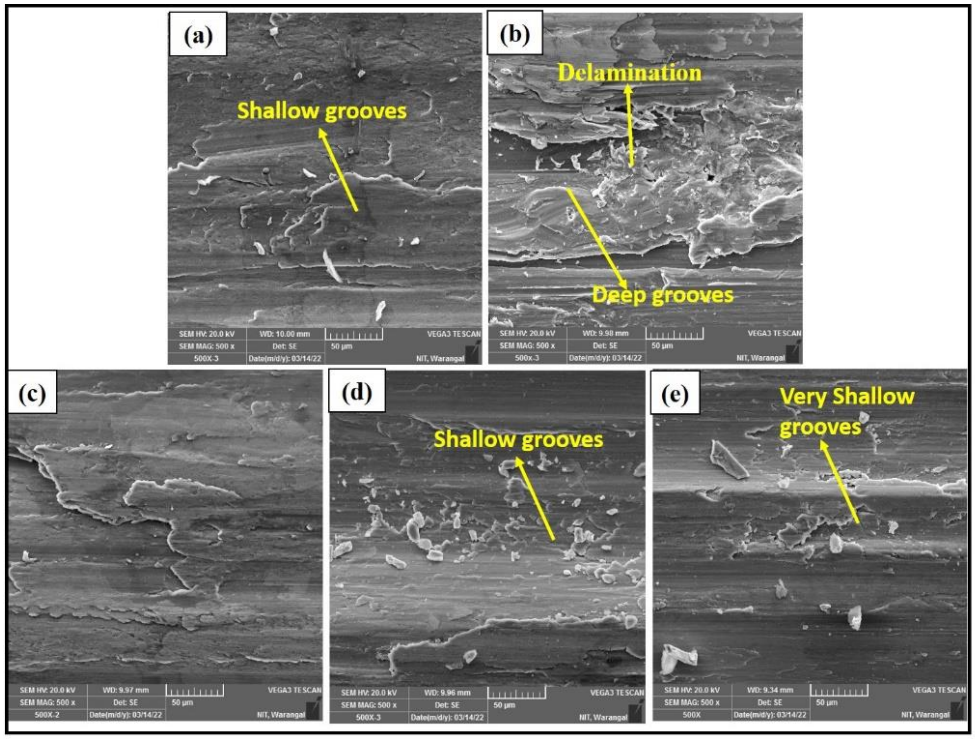

Figure 4.44 Worn surfaces of (a) BM, (b) NCFSW without interlayer, (c) NCFSW with interlayer, (d) WCFSW without interlayer and (e) WCFSW with interlayer for a sliding distance of 1000 m under 30 N load.

The mechanism of wear rate under 50 N load is similar to that of 30 N load, as shown in **Figure 4.45**. Compared to 30 N load, at 50 N load condition, there are generally very large and deep pits, which are believed to be the result of a ploughing action that dislodges hard particles, as shown in **Figure 4.45**. The worn surface of NC weld without interlayer demonstrates a severe plastic deformation, characterised by the formation of shallow craters with some irregular tearing ridges surrounding them, indicating that the wear type is predominantly adhesive, which explains the high mass loss and the high friction coefficient (**Figure 4.45(b)** and **(d)**). The hard reinforcing particles in welds with interlayers serve as load-bearing particles and provide great resistance to delamination, resulting in a decreased rate of material removal (**Figure 4.45(c)** and **(e)**).

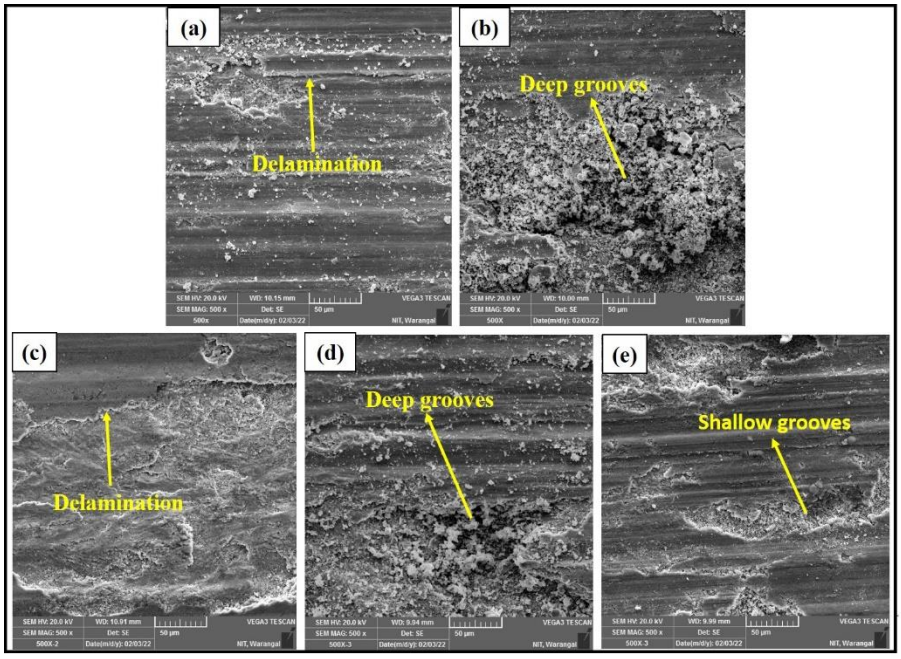

Figure 4.45 Worn surfaces of (a) BM, (b) NCFSW without interlayer, (c) NCFSW with interlayer, (d) WCFSW without interlayer and (e) WCFSW with interlayer for a sliding distance of 1000 m under 50 N load.

4.5 Fatigue behaviour

4.5.1 Fatigue crack growth rate of welds under natural cooling

As shown in **Figure 4.46**, the fatigue crack length (a) vs number of fatigue cycles (N) graph is plotted to evaluate the fatigue life of samples. According to the graph, the fatigue life of weld samples is better than that of BM, and as the number of fatigue cycles increased, increased the FCG rate. It demonstrates that weld samples prevented the fatigue crack from growing further. In weld samples, characteristics such as fine-grained structure, a large proportion of grain boundaries, precipitation factor, etc., impede fatigue crack propagation and prevent the fracture from growing further.

The fatigue crack growth process can be classified into three stages: (I) low-speed propagation region (crack initiation), (II) stable propagation region, and (III) rapid propagation zone as shown in **Figure 4.47(a)**. Region-I (R-I) is the stage of crack initiation. In this region, crack propagation stops as the value of da/dN approaches zero and as K approaches a critical value (K_{th}) below which it cannot propagate (Su et al. 2020). According to **Figure 4.47(a)**, the sample with the smallest grain size has the highest K_{th}, and the weld with interlayer sample has the highest K_{th} since its grain size is smaller than the other samples. The weld with interlayer

sample with the smaller grain size has a greater volume fraction of grain boundaries, which can act as barriers to crack propagation. In Region-II (R-II), also known as the steady-state fracture propagation stage, the FCG rate is linear. The FCG rate deviates from linearity at low and high ΔK values.

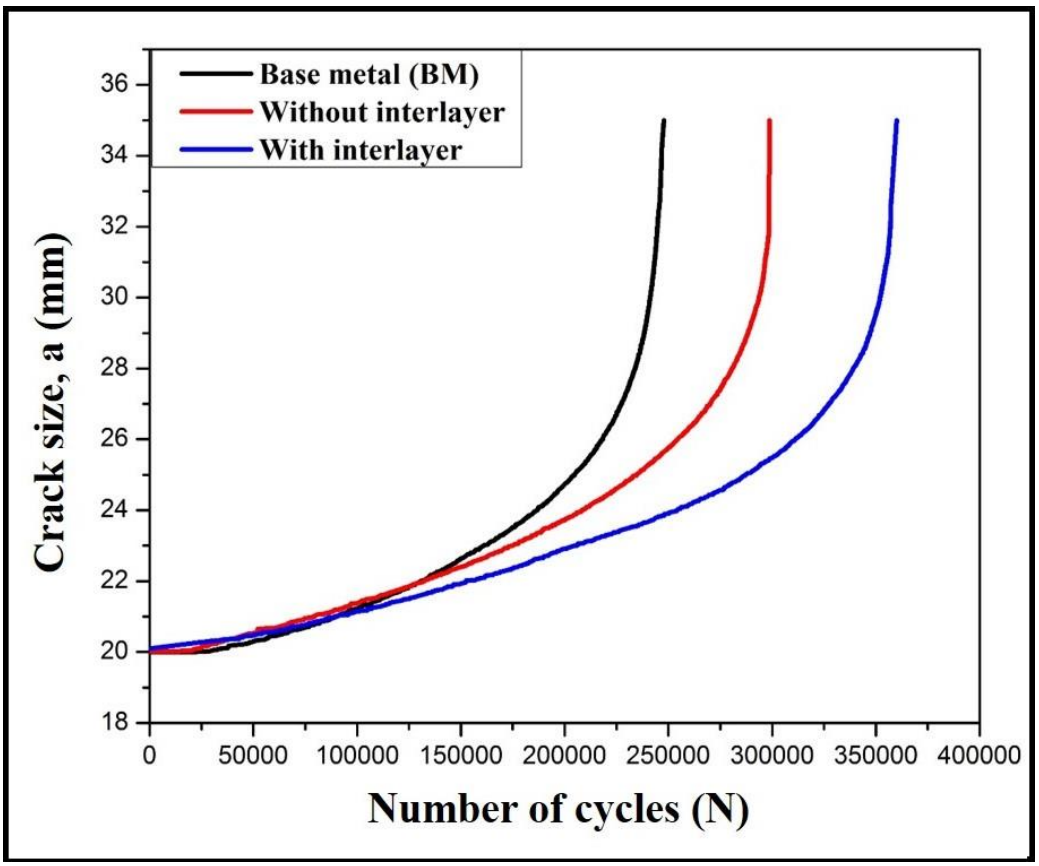

Figure 4.46 Number of cycles (N) Vs. Crack size (a) curve

Figure 47(b) depicts the log-log curve of the fatigue crack propagation rate da/dN vs. stress intensity factor K of Region-II for the liner fitting computation of Paris constants. The logarithmic curve of the linear region is described by the Paris model given by

$$\frac{da}{dN} = C\ (\Delta K)^m$$

Where C and m are constants (Beden et al. 2009). The equation shows that the da/dN depends exclusively on K, regardless of the stress ratio value. A linear relationship may be established between log(K) and log(da/dN), as shown by the equation.

$$\log\left(\frac{da}{dN}\right) = \log C + m \log(\Delta K)$$

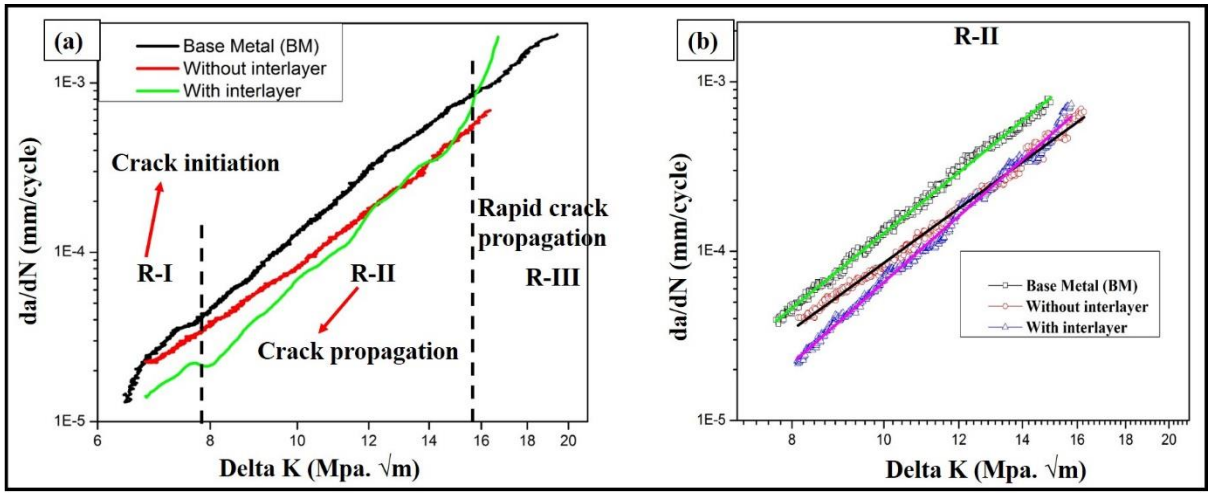

Figure 4.47 log-log plot of da/dN vs. ΔK graph showing three different regions of crack propagation and (b) log-log plot of da/dN vs. ΔK graph or Paris curve showing Region-II for evaluating Paris constants.

Table 4.12 shows the estimated values of the Paris constant, such as slope (m) and intercept (C). The steeper the slope, the bigger the m, indicating that the da/dN is more sensitive to changes in K. **Table 4.12** shows that the fitting findings in Region-II showed a linear relationship with a correlation coefficient of 0.996 or higher. At the early phases of fracture propagation, the crack growth rate of BM samples is faster than that of weld samples with the same K value, and the da/dN of weld with interlayer is the smallest. R-III is also known as a rapid or unstable crack propagation area. Microstructural flaws can significantly accelerate fracture propagation relative to this region's base metal at high ΔK.

Table 4.12 Paris constants

Sample	C	m	R^2	R
BM	3.60E-09	4.07	0.9968	0.998
Without interlayer	7.24E-09	4.54	0.9871	0.993
With interlayer	7.51E-10	4.94	0.9899	0.994

Figure 4.48 depicts low-magnification fracture images of BM, weld samples with and without interlayer revealing three distinct fracture areas. Different fracture locations of the BM are not clearly visible because they did not withstand a large number of fatigue cycles **(Figure 4.48(a))**. Still, the fracture regions of the weld samples are clearly visible (**Figure 4.48(b)** and **(c)**). At low magnification, fatigue fracture characteristics like striations, dimples, and cracks are not evident. **Figure 4.49** depicts the high magnification SEM fracture images of BM and

weld samples with and without interlayer. The fractured image of BM shows the ridges and plateaus interposed with a flat surface (**Figure 4.49(a))**. Weld samples witnessed peak and valley type of fracture surface, which contains striations marks and secondary cracks (**Figure 4.49(b)** and **(c)**). The presence of dimples on the fracture surface of BM suggested rapid crack propagation during the second stage, leading to an earlier fracture. The majority of striation markings are discontinuous, indicating rapid crack propagation. The FCG rate can also be approximated based on the space between striations. The weld with interlayer has a smaller striation space than the weld without interlayer. The distance between striations is proportional to the rate of fracture propagation. The precipitation/intermetallic component influences striations and fatigue crack development significantly. As a barrier to the progression of fractures, precipitate particles create a slight bending of the striate when they approach. However, in certain instances, the brittle intermetallics have poor contact with the aluminium matrix, function as stress concentration zones, and accelerate fatigue progression.

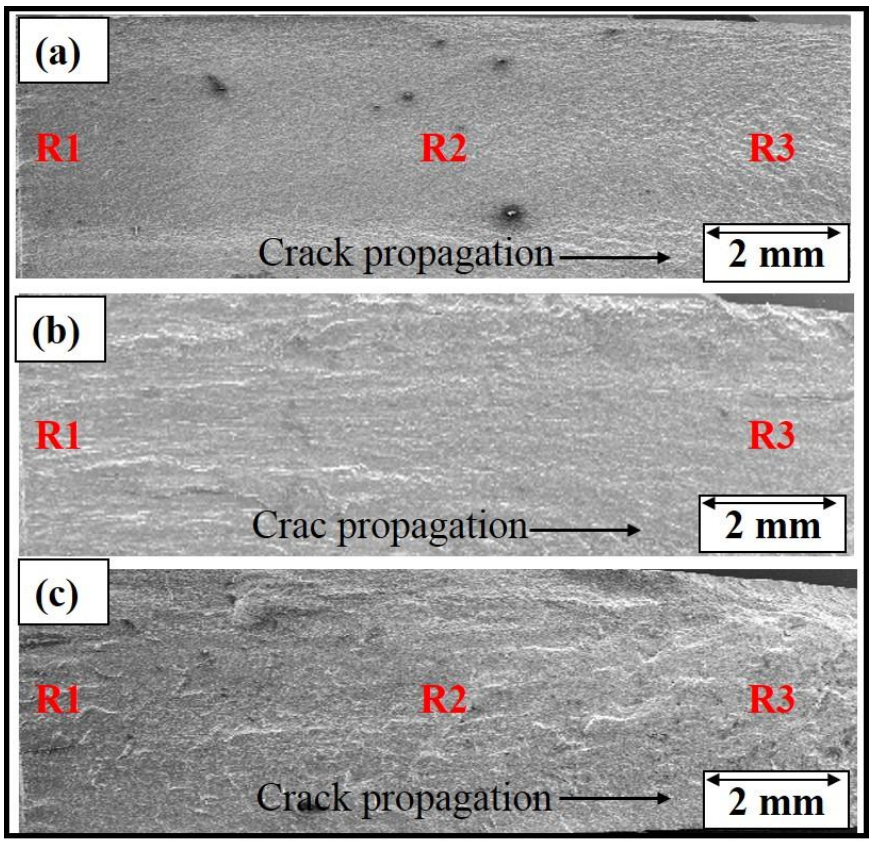

Figure 4.48 Low magnification fracture surfaces of (a) BM, (b) Weld without interlayer, and (c) Weld with interlayer.

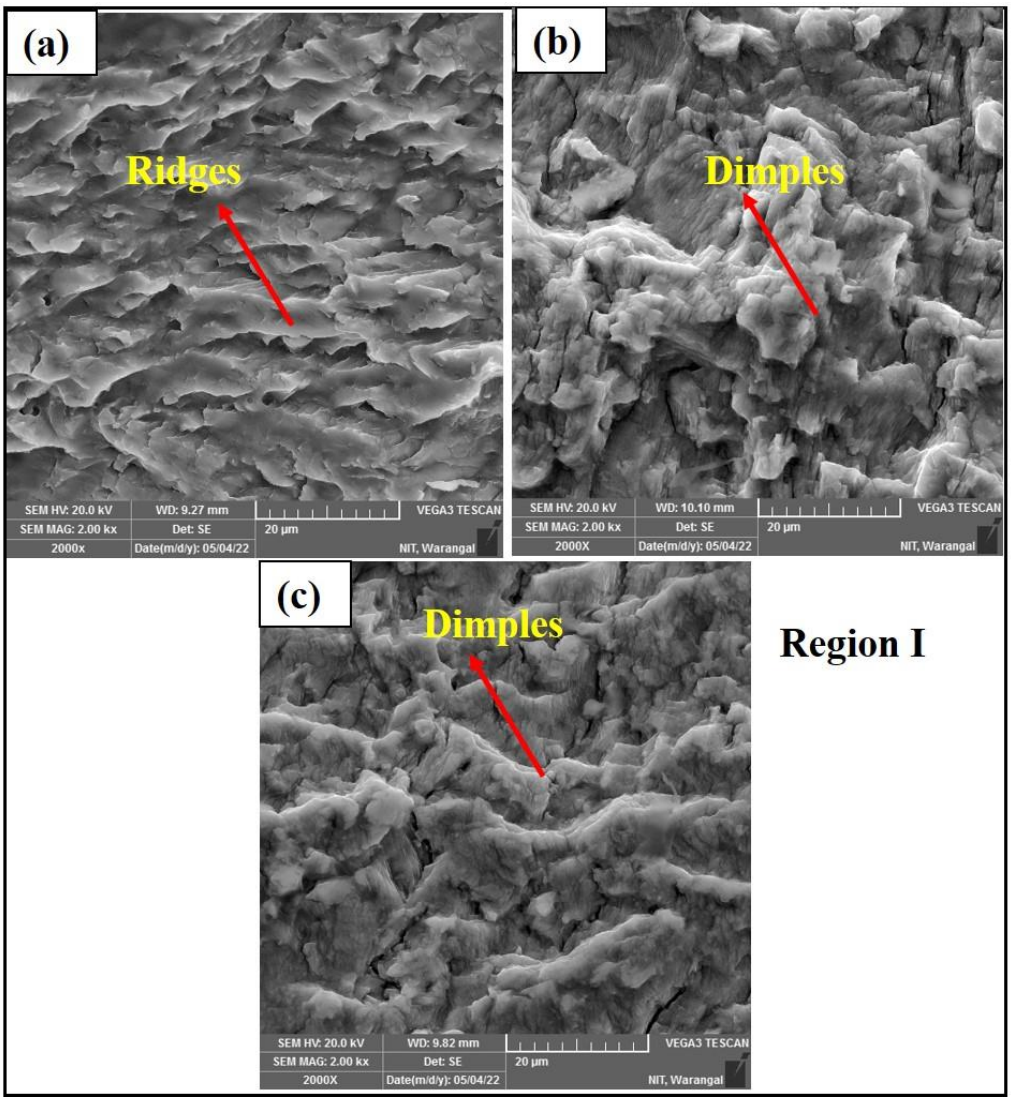

Figure 4.49 High magnification fracture surfaces of (a) BM, (b) Weld without interlayer, and (c) Weld with interlayer

4.5.2 Fatigue crack growth rate of welds under water cooling

The reduction in brittle IMCs formation for WCFSW with interlayer resulted in a strong bond between brass and Al which caused more obstacles for fatigue cracks propagation and stopped the crack from further expanding, thereby increasing the fatigue life compared to NC without interlayer (**Figure 4.50**).

Finer grains have a higher grain boundary area than coarse grains, inhibiting fracture formation and extending fatigue life. In addition to the preceding factor, the suppression of brittle IMCs reduced the stress concentration and acted as fracture propagation barriers (Zhang et al. 2020). According to a microstructural investigation, the WCFSW with interlayer sample had a higher fraction of high-angle boundaries. Based on the variables mentioned above, it was determined

that the fatigue life improved greatly following interlayer and was further enhanced by including a cooling medium. As documented in **Table 4.13**, more slope (m value) is observed for WCFSW with interlayer, which influences the da/dN value. da/dN is minimum for WCFSW with interlayer compared to without interlayer as presented in **Figure 4.51(a)**.

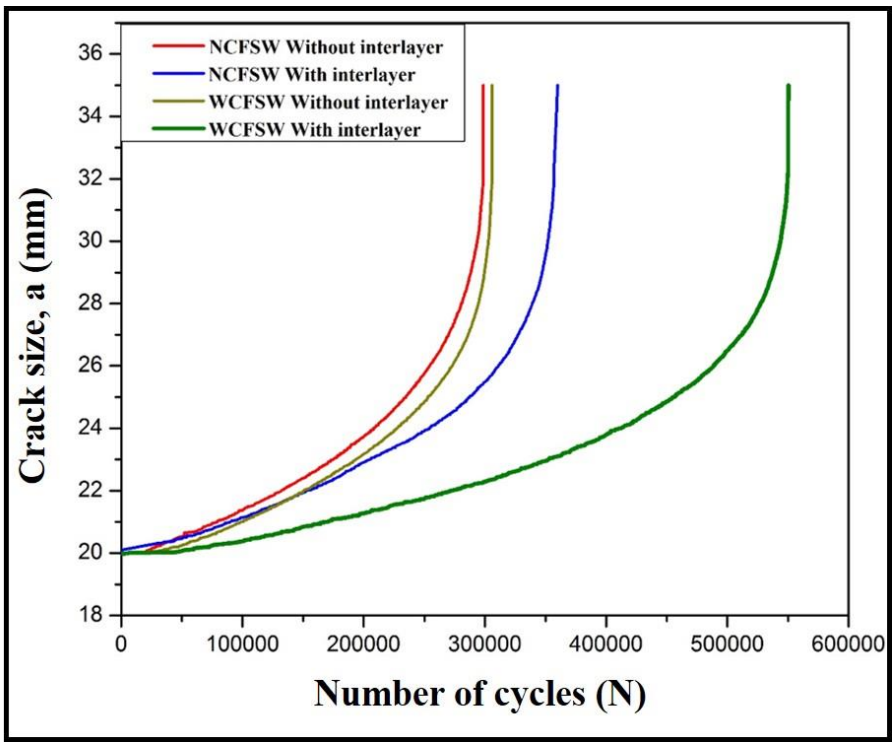

Figure 4.50 Number of cycles (N) Vs Crack size (a) curve of welds under both cooling media.

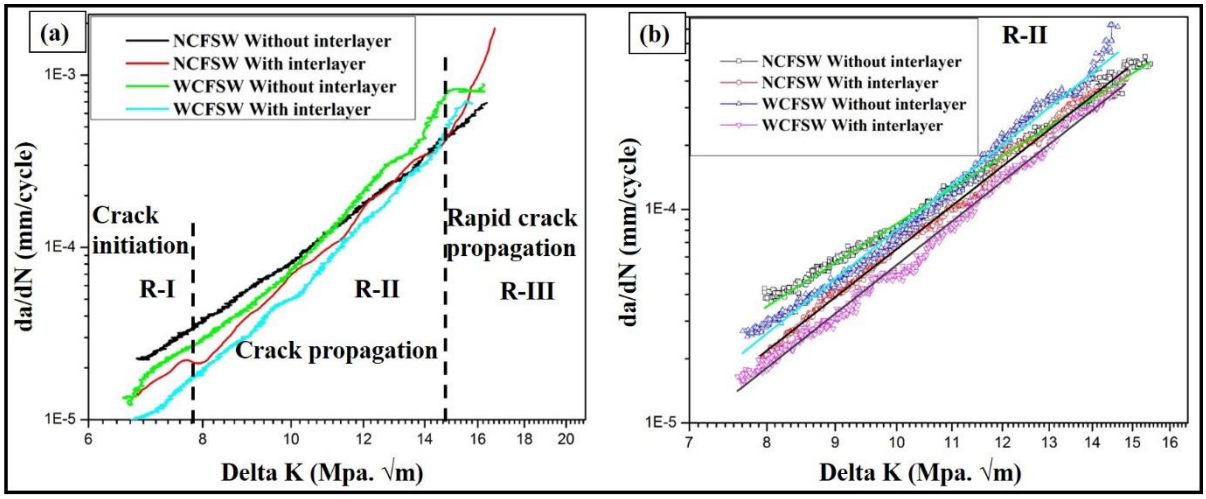

Figure 4.51 log-log plot of da/dN vs. ΔK graph and (b) log-log plot of da/dN vs. ΔK graph or Paris curve showing Region-II for evaluating Paris constants

Table 4.13 Paris constants

Sample	C	m	R^2	R
NCFSW without interlayer	7.24E-09	4.54	0.9871	0.993
NCFSW with interlayer	7.51E-10	4.94	0.9899	0.994
WCFSW without interlayer	7.64E-10	4.96	0.990	0.995
WCFSW with interlayer	5.99E-10	5.20	0.993	0.996

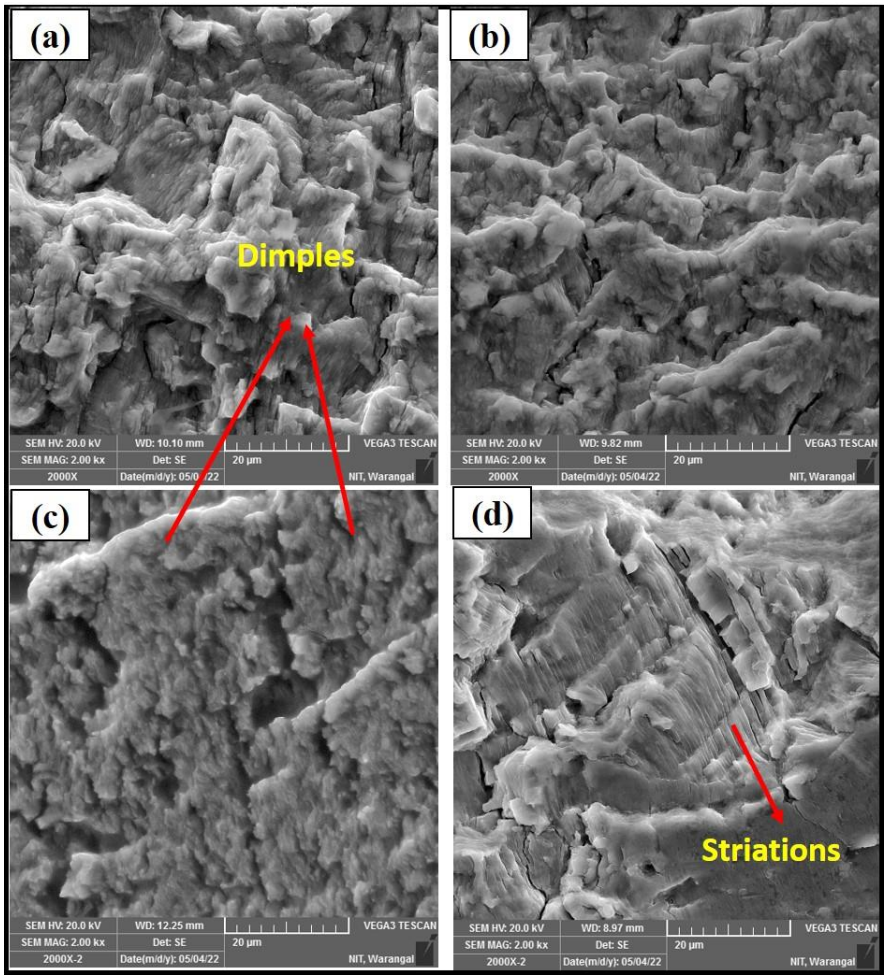

Figure 4.52 High magnification fracture surfaces of (a) NCFSW without interlayer, (b) NCFSW with interlayer, (c) WCFSW without interlayer, and (d) WCFSW with interlayer.

The striations were bent after they went through the IMCs, indicating the intermetallics in Al alloy matrix can impede the propagation of fatigue crack (**Figure 4.52(b)** and **(d)**). Water cooling can strengthen more interface bonding resulting in arresting the crack propagation. The striation space is much less in WCFSW with interlayer **(Figure 4.52(d))**, representing that the fatigue crack growth is lower than the remaining samples indicating higher fatigue life.

CHAPTER 5

CONCLUSIONS

5.1 Conclusions

In the present investigation, a new approach is introduced to reduce the thermal softening of precipitation-hardened AA6061-T6 alloy and improve mechanical properties. In order to overcome the problems with heat generation during FSW, such as the formation of brittle IMCs, water-cooling was used, and the material flow, microstructural evolution, mechanical properties and corrosion behaviour were analyzed and correlated. The wear characteristics, damping behaviour and fatigue life of welds with and without interlayer under both cooling media were also studied.

This chapter summarises the primary conclusions drawn from each research objective.

5.1.1 Selection of FSW process parameters to get defect-free joint and enhanced mechanical properties using brass interlayer

In this objective, AA6061 plates were successfully welded with and without interlayer, and the following conclusions were drawn.

1. The proper material flow and uniform composite structure were observed at the optimum tool traverse speed of 25 mm/min and tool rotational speed of 800 rpm.
2. From EBSD analysis, the grain refinement and equiaxed grain structure were observed at SZ for the welded samples. The weld with interlayer shown better grain refinement in comparison to the weld without interlayer.
3. The formation of IMCs such as Al_2Cu and Al_4Cu_9 was observed at the brass and Al matrix interface for weld with interlayer are attributed to interdiffusion reaction between brass and Al.
4. The mechanical properties of weld with interlayer are improved compared to weld without interlayer due to the formation of IMCs. The weld fracture with and without interlayer occurred on the retreating side, where the hardness is lower.
5. The better corrosion resistance was observed for weld with interlayer due to the formation of less active IMC such as Al_2Cu in SZ.

5.1.2 Effect of cooling media and interlayer on microstructure and mechanical properties of the welded joint

In this objective, the simultaneous effect of water-cooling and interlayer on FSWed AA6061 was studied, and the following conclusions were extracted.

1. The WCFSW decreased the SZ size for weld with and without interlayer compared to the NCFSW due to rapid heat extraction from the SZ. Moreover, the grains size in HAZ decreased with water-cooling.
2. It was observed from the EBSD analysis that the grain refinement with equiaxed grain structure at SZ for all the weld samples attributed to the DRX and DRV mechanisms during FSW. The WCFSW with interlayer showed better grain refinement in comparison to other welds.
3. The brittle IMCs were formed due to the high heat generation and slow cooling rate during NCFSW with interlayer, which were minimized with water cooling. Thin interface diffusion and fewer IMCs were formed for WCFSW with interlayer than NCFSW due to faster cooling rate. Fine precipitates of WCFSW without interlayer compared to NCFSW were distributed along grain boundaries.
4. The strength of WCFSW welds with and without interlayer is better than NCFSW due to fine precipitates, fewer IMCs in SZ, and a decrease in grain size of HAZ. However, higher strength was obtained for WCFSW with interlayer.
5. Superior corrosion resistance was obtained for WCFSW than NCFSW with interlayer due to the suppression in the formation of IMCs attributed to a decrease in volume fraction of IMCs. The better corrosion resistance was observed for WCFSW than the NCFSW without interlayer due to the fine and uniform distribution of Mg_2Si precipitates.

5.1.3 Damping capacity and wear characteristics of welds with and without interlayer of natural cooling and water cooling

In this objective, the effect of brass interlayer and cooling media on the damping capacity and wear rate of FSWed AA6061 was studied, and the following conclusions were drawn.

1. Due to dynamic recrystallization after FSW, the grain refinement occurred for weld samples. The WC weld with interlayer showed more grain refinement.
2. The high peaks and density of IMCs were decreased for WC weld with interlayer due to the rapid cooling rate and a short time to react brass with Al matrix.

3. The frequency-dependent damping is enhanced with brass interlayer attributed to the high inherent damping of brass. Furthermore, the WC weld with interlayer showed better damping due to the suppression of the formation of IMCs.
4. WC weld with interlayer showed the highest temperature-dependent damping due to more grain boundary area.
5. The wear rate of the weld without using interlayer is higher, and it was minimized for weld with an interlayer. Minimum wear rate for weld with brass interlayer is attributed to the better grain refinement and corresponding hardening.

5.1.4 Fatigue behaviour

In this objective, the effect of brass interlayer and cooling media on fatigue behaviour of FSWed AA6061 was studied, and the following conclusions were drawn.

1. The fatigue life of welds has shown better than base metal attributed to the grain refinement phenomenon and high angle grain boundaries of weld samples.
2. Weld with interlayer has shown better fatigue life compared to without interlayer due to the formation of strengthening IMCs.
3. The WCFSW with interlayer showed superior fatigue life due to the suppression in forming brittle IMCs. During dynamic loading, the strong metallurgical bond between Al matrix and brass particles acted as an obstacle to crack propagation**.**
4. The fewer striations gap in the fracture surface of weld with interlayer confirms the obstacle to the crack propagation and improved fatigue life.

5.2 Future Scope

In the present study, the only brass interlayer is used, and the water cooling used to reduce the brittle IMCs is water. However, the following future scope can be employed to improve the mechanical properties.

1. Different interlayer materials such as Mg, Ti can be used to enhance the mechanical properties.
2. Other cooling media (Dry ice/liquid nitrogen) can inhibit the formation of brittle intermetallics and enhance the mechanical properties.
3. The effect of multipass welding under natural cooling can be investigated for better

grain refinement and the formation of finer IMCs.

4. Heat treatment can be performed on natural cooling weld with interlayer and study the intermetallic behaviour. Compare the results of water-cooling and heat-treated welds with interlayer.
5. The same interlayer approach can study the microstructure and mechanical properties of non-heat-treatable Al alloys.

References

Abdollahzadeh, Amin, Behrouz Bagheri, Mahmoud Abassi, Amir Hossein Kokabi, and Ahmad Ostovari Moghaddam. 2021. "Comparison of the Weldability of AA6061-T6 Joint under Different Friction Stir Welding Conditions." 30(February):1110–27.

Akbari, Mostafa and Reza Abdi Behnagh. 2012. "Dissimilar Friction-Stir Lap Joining of 5083 Aluminum Alloy to CuZn34 Brass." *Metallurgical and Materials Transactions B: Process Metallurgy and Materials Processing Science* 43(5):1177–86.

Akinlabi, Esther T, Anthony Andrews, and Stephen A. Akinlabi. 2014. "Effects of Processing Parameters on Corrosion Properties of Dissimilar Friction Stir Welds of Aluminium and Copper." *Transactions of Nonferrous Metals Society of China* 24(5):1323–30.

Akinlabi, Esther T., Anthony Andrews, and Stephen A. Akinlabi. 2014. "Effects of Processing Parameters on Corrosion Properties of Dissimilar Friction Stir Welds of Aluminium and Copper." *Transactions of Nonferrous Metals Society of China (English Edition)* 24(5):1323–30.

Alishavandi, Mahdi, Mohammad Amin Razmjoo Khollari, Mahnam Ebadi, Sajjad Alishavandi, and Amir Hossein Kokabi. 2020. "Corrosion-Wear Behavior of AA1050/Mischmetal Oxides Surface Nanocomposite Fabricated by Friction Stir Processing." *Journal of Alloys and Compounds* 832.

Anvari, S. R., F. Karimzadeh, and M. H. Enayati. 2013. "Wear Characteristics of Al – Cr – O Surface Nano-Composite Layer Fabricated on Al6061 Plate by Friction Stir Processing." *Wear* 304(1–2):144–51.

Avettand-fènoël, M., T. Nagaoka, M. Marinova, and R. Taillard. 2020. "Upon the e Ff Ect of Zn during Friction Stir Welding of Aluminum-Copper and Aluminum-Brass Systems." 58(June):259–78.

Baghdadi, Amir Hossein, Armin Rajabi, Nor Fazilah, Mohamad Selamat, Zainuddin Sajuri, and Mohd Zaidi Omar. 2019. "Materials Science & Engineering A E Ff Ect of Post-Weld Heat Treatment on the Mechanical Behavior and Dislocation Density of Friction Stir Welded Al6061." 754(September 2018):728–34.

Beden, S. M., S. Abdullah, and A. K. Ariffin. 2009. *Review of Fatigue Crack Propagation Models for Metallic Components*. Vol. 28.

Biswas, Somjeet, Dong Ik Kim, and Satyam Suwas. 2012. “Asymmetric and Symmetric Rolling of Magnesium: Evolution of Microstructure, Texture and Mechanical Properties.” *Materials Science and Engineering A* 550:19–30.

Callister, W. D. 1991. “Materials Science and Engineering: An Introduction (2nd Edition).” Materials & Design 12(1):59.

Çam, G., G. İpekoğlu, and H. Tarık Serindağ. 2014. “Effects of Use of Higher Strength Interlayer and External Cooling on Properties of Friction Stir Welded AA6061-T6 Joints Effects of Use of Higher Strength Interlayer and External Cooling on Properties of Friction Stir Welded AA6061-T6 Joints.” 1718.

Chen, Chih Yuan and Weng Sing Hwang. 2007. “Effect of Annealing on the Interfacial Structure of Aluminum-Copper Joints.” *Materials Transactions* 48(7):1938–47.

Chen, Wei, Wenxian Wang, Zepeng Liu, Xin Zhai, Gongbo Bian, and Tingting Zhang. 2021. “Improvement in Tensile Strength of Mg / Al Alloy Dissimilar Friction Stir Welding Joints by Reducing Intermetallic Compounds.” *Journal of Alloys and Compounds* 861:157942.

Chen, Wei, Wenxian Wang, Zepeng Liu, Xin Zhai, Gongbo Bian, Tingting Zhang, and Peng Dong. 2021. “Improvement in Tensile Strength of Mg/Al Alloy Dissimilar Friction Stir Welding Joints by Reducing Intermetallic Compounds.” *Journal of Alloys and Compounds* 861:157942.

Choi, Kyoung Joon, Seung Chang Yoo, Seunghyun Kim, Taeho Kim, Junhyuk Ham, Jeonghyeon Lee, and Ji Hyun Kim. 2019. “Microstructural Evolution and Corrosion Behaviour of Thermally Aged Dissimilar Metal Welds of Low-Alloy Steel and Nickel-Based Alloy.” *Corrosion Science* 153(March):138–49.

Davis, J.R., 2001. Aluminium and Aluminium Alloys 351–416. https://doi.org/10.1361/autb2001p351

Dialami, Narges, Miguel Cervera, and Michele Chiumenti. 2019. “Defect Formation and Material Flow in Friction Stir Welding.” 7(November).

E., Anthony, Nick Birbilis, Johannes M.C., Santiago J., Xiaorong Zhou, and George E. 2011. “High Strength Al-Alloys: Microstructure, Corrosion and Principles of Protection.” *Recent Trends in Processing and Degradation of Aluminium Alloys*.

Esmaeili, A., M. K. Besharati Givi, and H. R. Zareie Rajani. 2011. “A Metallurgical and Mechanical Study on Dissimilar Friction Stir Welding of Aluminum 1050 to Brass (CuZn30).” 528:7093–7102.

Esmaeili, A., H. R. Zareie Rajani, M. Sharbati, M. K. Besharati Givi, and M. Shamanian. 2011. “Intermetallics The Role of Rotation Speed on Intermetallic Compounds Formation and Mechanical Behavior of Friction Stir Welded Brass / Aluminum 1050 Couple.” 19:1711–19.

Fathi, Jalal, Pejman Ebrahimzadeh, Reza Farasati, and Reza Teimouri. 2019a. “Friction Stir Welding of Aluminum 6061-T6 in Presence of Watercooling : Analyzing Mechanical Properties and Residual Stress Distribution.” *International Journal of Lightweight Materials and Manufacture* 2(2):107–15.

Fathi, Jalal, Pejman Ebrahimzadeh, Reza Farasati, and Reza Teimouri. 2019b. “Friction Stir Welding of Aluminum 6061-T6 in Presence of Watercooling : Analyzing Mechanical Properties and Residual Stress Distribution.” 2.

Fonda, R. W. 2004. “Development of Grain Structure during Friction Stir Welding.” 51:243–48.

Gharavi, Farhad, Khamirul Amin, and Robiah Yunus. 2015. “Corrosion Behavior of Al6061 Alloy Weldment.” *Integrative Medicine Research* 4(3):314–22.

Gharavi, Farhad, Khamirul A. Matori, Robiah Yunus, Norinsan K. Othman, and Firouz Fadaeifard. 2016. “Corrosion Evaluation of Friction Stir Welded Lap Joints of AA6061-T6 Aluminum Alloy.” 26:684–96.

Gomathisankar, M., M. Gangatharan, and P. Pitchipoo. 2018. “ScienceDirect A Novel Optimization of Friction Stir Welding Process Parameters on Aluminum Alloy 6061-T6.” *Materials Today: Proceedings* 5(6):14397–404.

Hanzaki, A. Zarei-. 2011. “Wear Assessment of Al / Al 2 O 3 Nano-Composite Surface Layer Produced Using Friction Stir Processing.” *Wear* 270(5–6):403–12.

Hassanifard, S., H. Alipour, and A. Ghiasvand. 2021. “Fatigue Response of Friction Stir Welded Joints of Al 6061 in the Absence and Presence of Inserted Copper Foils in the Butt Weld.” 64(January):1–9.

Huang, Guoqiang, Wentao Hou, Junping Li, and Yifu Shen. 2018. “Surface & Coatings

Technology Development of Surface Composite Based on Al-Cu System by Friction Stir Processing : Evaluation of Microstructure , Formation Mechanism and Wear Behavior." 344(October 2017):30–42.

Huang, Yongxian, Yuming Xie, Xiangchen Meng, Zongliang Lv, and Jian Cao. 2018. "Numerical Design of High Depth-to-Width Ratio Friction Stir Welding." *Journal of Materials Processing Technology* 252(September 2017):233–41.

Jaiganesh, P. Sevvel V. 2015. "Effect of Tool Shoulder Diameter to Plate Thickness Ratio on Mechanical Properties and Nugget Zone Characteristics During FSW of Dissimilar Mg Alloys." *Transactions of the Indian Institute of Metals* 68(1):41–46.

Jiang, H. J., C. Y. Liu, B. Zhang, P. Xue, Z. Y. Ma, K. Luo, M. Z. Ma, and R. P. Liu. 2017. "Simultaneously Improving Mechanical Properties and Damping Capacity of Al-Mg-Si Alloy through Friction Stir Processing." *Materials Characterization* 131:425–30.

Joon, Kyoung, Seung Chang, Seunghyun Kim, Taeho Kim, Junhyuk Ham, Jeonghyeon Lee, and Ji Hyun. 2019. "Microstructural Evolution and Corrosion Behaviour of Thermally Aged Dissimilar Metal Welds of Low-Alloy Steel and Nickel-Based Alloy." *Corrosion Science* 153(March):138–49.

Khojastehnezhad, Vahid M and Hamed H. Pourasl. 2018. "Microstructural Characterization and Mechanical Properties of Aluminum 6061-T6 Plates Welded with Copper Insert Plate (Al / Cu / Al) Using Friction Stir Welding." *Transactions of Nonferrous Metals Society of China* 28(3):415–26.

Khojastehnezhad, Vahid M. and Hamed H. Pourasl. 2018. "Microstructural Characterization and Mechanical Properties of Aluminum 6061-T6 Plates Welded with Copper Insert Plate (Al/Cu/Al) Using Friction Stir Welding." *Transactions of Nonferrous Metals Society of China (English Edition)* 28(3):415–26.

Krishna, P. Murali. 2011. "Effect of Post-Weld Heat Treatment on the Mechanical Properties of Friction Stir Welds of Dissimilar Aluminum Alloys." *International Journal of Engineering Science* 3(7):5778–85.

Kumar, Kethavath Kranthi and Adepu Kumar. 2021. "Effect of Friction Stir Welding Parameters on the Material Flow , Mechanical Properties and Corrosion Behavior of Dissimilar AA5083-AA6061 Joints."

Kumar, Kethavath Kranthi, Adepu Kumar, and M. V. N. V. Satyanarayana. 2021. “Enhancing Corrosion Resistance and Mechanical Properties of Dissimilar Friction Stir Welded 5083-6061 Aluminium Alloys Using External Cooling Environment.” *Proceedings of the Institution of Mechanical Engineers, Part L: Journal of Materials: Design and Applications*.

Mahto, Raju Prasad, Matruprasad Rout, and Surjya Kanta Pal. 2021. “Mechanism of Microstructure Evolution and Grain Growth in Friction Stir Welding of AA6061-T6 and AISI304 in Air and Water Media.” *Materials Chemistry and Physics* 273(May):125081.

Malopheyev, Sergey, Igor Vysotskiy, Vladislav Kulitskiy, and Sergey Mironov. 2016. “Materials Science & Engineering A Optimization of Processing-Microstructure-Properties Relationship in Friction-Stir Welded 6061-T6 Aluminum Alloy.” *Materials Science & Engineering A* 662:136–43.

Mcnelley, T. R., S. Swaminathan, and J. Q. Su. 2008. “Recrystallization Mechanisms during Friction Stir Welding / Processing of Aluminum Alloys.” 58:349–54.

Mehta, K. M. and V. J. Badheka. 2019. “Wear Behavior of Boron-Carbide Reinforced Aluminum Surface Composites Fabricated by Friction Stir Processing.” 427(January):975–80.

Mehta, Kush P. and Vishvesh J. Badheka. 2015. “Influence of Tool Design and Process Parameters on Dissimilar Friction Stir Welding of Copper to AA6061-T651 Joints.” 2073–82.

Mehta, Kush P. and Vishvesh J. Badheka. 2017. “Journal of Materials Processing Technology Hybrid Approaches of Assisted Heating and Cooling for Friction Stir Welding of Copper to Aluminum Joints.” 239:336–45.

Mehta, Kush P., Pierpaolo Carlone, Antonello Astarita, Fabio Scherillo, and Felice Rubino. 2019. “Materials Science & Engineering A Conventional and Cooling Assisted Friction Stir Welding of AA6061 and AZ31B Alloys.” 759(April):252–61.

Mehta, M., A. Arora, and T. Debroy. 2011. “Tool Geometry for Friction Stir Welding — Optimum Shoulder Diameter.”

Meng, Xiangchen, Yongxian Huang, Jian Cao, Junjun Shen, and Jorge F. dos Santos. 2021. “Recent Progress on Control Strategies for Inherent Issues in Friction Stir Welding.”

Progress in Materials Science 115(June 2020).

Meshram, Suresh D. and G. Madhusudhan Reddy. 2018. “Influence of Tool Tilt Angle on Material Flow and Defect Generation in Friction Stir Welding of AA2219.” 68(5):512–18.

Miller, W. S., L. Zhuang, J. Bottema, A. J. Wittebrood, P. De Smet, A. Haszler, and A. Vieregge. 2000. “Recent Development in Aluminium Alloys for the Automotive Industry.” *Materials Science and Engineering A* 280(1):37–49.

Mishra, R. S. and Z. Y. Ma. 2005. “Friction Stir Welding and Processing.” 50:1–78.

Mofid, M. A. and F. Malek Ghaini. 2012. “The Effect of Water Cooling during Dissimilar Friction Stir Welding of Al Alloy to Mg Alloy.” 36:161–67.

Mofid, Mohammad Ammar, Amir Abdollah-zadeh, Farshid Malek Ghaini, and Cemil Hakan Gu. n.d. “Submerged Friction-Stir Welding (SFSW) Underwater and Under Liquid Nitrogen : An Improved Method to Join Al Alloys to Mg Alloys.”

Mokabberi, S. R., M. Movahedi, and A. H. Kokabi. 2018. “Effect of Interlayers on Softening of Aluminum Friction Stir Welds.” *Materials Science and Engineering A* 727(March):1–10.

Mokabberi, S R, M. Movahedi, and A. H. Kokabi. 2018a. “Materials Science & Engineering A E Ff Ect of Interlayers on Softening of Aluminum Friction Stir Welds.” *Materials Science & Engineering A* 727(April):1–10.

Mokabberi, S R, M. Movahedi, and A. H. Kokabi. 2018b. “Materials Science & Engineering A E Ff Ect of Interlayers on Softening of Aluminum Friction Stir Welds.” *Materials Science & Engineering A* 727(March):1–10.

Nandan, R., T. Debroy, and H. K. D. H. Bhadeshia. 2008. “Recent Advances in Friction-Stir Welding – Process , Weldment Structure and Properties.” 53:980–1023.

Narimani, Mohammad, Behnam Lot, and Zohreh Sadeghian. 2016. “Surface & Coatings Technology Evaluation of the Microstructure and Wear Behaviour of AA6063-B 4 C / TiB 2 Mono and Hybrid Composite Layers Produced by Friction Stir Processing.” 285:1–10.

Padmanaban, G. and V. Balasubramanian. 2009. “Selection of FSW Tool Pin Profile , Shoulder

Diameter and Material for Joining AZ31B Magnesium Alloy – An Experimental Approach." *Materials and Design* 30(7):2647–56.

Palanivel, R., I. Dinaharan, R. F. Laubscher, and J. Paulo Davim. 2016. "In Fl Uence of Boron Nitride Nanoparticles on Microstructure and Wear Behavior of AA6082 / TiB 2 Hybrid Aluminum Composites Synthesized by Friction Stir Processing." *JMADE* 106:195–204.

Patel, Prins, Harikrishnasinh Rana, Vishvesh Badheka, and Vivek Patel. 2020. "Effect of Active Heating and Cooling on Microstructure and Mechanical Properties of Friction Stir – Welded Dissimilar Aluminium Alloy and Titanium Butt Joints." 365–78.

Perez, R. J., J. Zhang, M. N. Gungor, and E. J. Lavernia. 1993. "Damping Behavior of 6061Al/Gr Metal Matrix Composites." *Metallurgical Transactions A* 24(3):701–12.

Rajakumar, S., C. Muralidharan, and V. Balasubramanian. 2011. "Predicting Tensile Strength , Hardness and Corrosion Rate of Friction Stir Welded AA6061-T 6 Aluminium Alloy Joints." *Materials and Design* 32(5):2878–90.

Ramanjaneyulu, K., G. Madhusudhan Reddy, and A. Venugopal Rao. 2014. "Role of Tool Shoulder Diameter in Friction Stir Welding : An Analysis of the Temperature and Plastic Deformation of AA 2014 Aluminium Alloy." 67:769–80.

Rao, K. Prasad, G. D. Janaki Ram, and B. E. Stucker. 2010. "Effect of Friction Stir Processing on Corrosion Resistance of Aluminum – Copper Alloy Gas Tungsten Arc Welds." *Materials and Design* 31(3):1576–80.

Reads, Citations. 2021. "THE IMPORTANCE OF FRICTION STIR WELDING Ákos Meilinger , Imre Török." (January 2013).

Reddy, Koppula Venkateswara, Ramavath Bheekya Naik, Gankidi Madhusudhan Reddy, Chakravarthy Pammi, and Raju Arockia Kumar. 2022. "Damping Property of AA6061/SiCp Surface Composites Developed through Friction Stir Processing." *Journal of Materials Engineering and Performance* 31(1):75–81.

Rojas, Jose I. and Daniel Crespo. 2012. "Modeling of the Effect of Temperature, Frequency, and Phase Transformations on the Viscoelastic Properties of AA 7075-T6 and AA 2024-T3 Aluminum Alloys." *Metallurgical and Materials Transactions A: Physical Metallurgy and Materials Science* 43(12):4633–46.

Satyanarayana, Marukurti V. N. V., Adepu Kumar, and Shivraman Thapliyal. 2021. "Effect of

Microstructure and Precipitate Formation on Mechanical and Corrosion Behavior of Friction Stir Processed AA6061 Alloy Using Different Cooling Media." *Proceedings of the Institution of Mechanical Engineers, Part L: Journal of Materials: Design and Applications* 235(11):2454–69.

Satyanarayana, Marukurti V. N. V and Adepu Kumar. 2021. "Effect of Microstructure and Precipitate Formation on Mechanical and Corrosion Behavior of Friction Stir Processed AA6061 Alloy Using Different Cooling Media."

Shamsipur, Ali, Amir Anvari, and Ahmad Keyvani. 2018. "Improvement of Microstructure and Corrosion Properties of Friction Stir Welded AA5754 by Adding Zn Interlayer." 25(8):967–73.

Singh, Subhash and Kaushik Pal. 2017. "Influence of Surface Morphology and UFG on Damping and Mechanical Properties of Composite Reinforced with Spinel MgAl2O4-SiC Core-Shell Microcomposites." *Materials Characterization* 123:244–55.

Sinhmar, S. and D. K. Dwivedi. 2017a. "Materials Science & Engineering A Enhancement of Mechanical Properties and Corrosion Resistance of Friction Stir Welded Joint of AA2014 Using Water Cooling." 684(December 2016):413–22.

Sinhmar, S. and D. K. Dwivedi. 2017b. "Materials Science & Engineering A Enhancement of Mechanical Properties and Corrosion Resistance of Friction Stir Welded Joint of AA2014 Using Water Cooling." 684(September 2016):413–22.

Siva Prasad, Dora and Chintada Shoba. 2015. "Damping Behavior of Metal Matrix Composites." *Transactions of the Indian Institute of Metals* 68(2):161–67.

Sravanthi, S. S. and Swati Ghosh Acharyya. 2018. "Effect of Welding Parameters on the Corrosion Behavior of Dissimilar Alloy Welds of T6 AA6061 Al-Galvanized Mild Steel." *Journal of Materials Engineering and Performance* 27(10):5518–31.

Srirangarajalu, N. and A. Rajadurai. 2016. "Microstructure and Mechanical Behaviour of Friction Stir Welded ETP Copper." *Metallurgia Italiana* 108(2):13–20.

Strass, Benjamin, Guntram Wagner, Christian Conrad, Bernd Wolter, Sigrid Benfer, and Wolfram Fuerbeth. 2014. "Realization of Al/Mg-Hybrid-Joints by Ultrasound Supported Friction Stir Welding - Mechanical Properties, Microstructure and Corrosion Behavior." *Advanced Materials Research* 966–967(June):521–35.

Su, Jian-qing, Tracy W. Nelson, and Colin J. Sterling. 2005. “Microstructure Evolution during FSW / FSP of High Strength Aluminum Alloys.” 405:277–86.

Su, Yang, Hossein Asadi, and Hamid Nikraz. 2020. “Comparison of Varied Specimen Geometry for Simplified VECD Test with Pulse-Rest Period.” *International Journal of Pavement Research and Technology* 13(4):392–401.

Taillard, R., G. Ji, and D. Goran. 2012. “Multiscale Study of Interfacial Intermetallic Compounds in a Dissimilar Al 6082-T6 / Cu Friction-Stir Weld.” 43(December):4655–66.

Threadgill, P. L., A. J. Leonard, H. R. Shercliff, P. J. Withers, P. L. Threadgill, A. J. Leonard, H. R. Shercliff, and P. J. Withers. 2013. “Friction Stir Welding of Aluminium Alloys Friction Stir Welding of Aluminium Alloys.” 6608(2009).

Venkateswara Reddy, K., R. Bheekya Naik, Golla Rama Rao, G. Madhusudhan Reddy, and R. Arockia Kumar. 2020. “Microstructure and Damping Capacity of AA6061/Graphite Surface Composites Produced through Friction Stir Processing.” *Composites Communications* 20(March).

Vysotskiy, Igor, Sergey Malopheyev, Salaheddin Rahimi, and Sergey Mironov. 2019. “Materials Science & Engineering A Unusual Fatigue Behavior of Friction-Stir Welded Al – Mg – Si Alloy.” 760(May):277–86.

Wahid, Mohd Atif, Zahid A. Khan, and Arshad Noor Siddiquee. 2019. “Analysis of Process Parameters Effects on Underwater Friction Stir Welding of Aluminum Alloy 6082-T6.” 233(6):1700–1710.

Wang, Qingzhao, Yong Zhao, Keng Yan, and Sheng Lu. 2015. “Corrosion Behavior of Spray Formed 7055 Aluminum Alloy Joint Welded by Underwater Friction Stir Welding.” 68:97–103.

Wang, Tao, Yong Zou, and Kenji Matsuda. 2016. “Micro-Structure and Micro-Textural Studies of Friction Stir Welded AA6061-T6 Subjected to Different Rotation Speeds.” 90:13–21.

Wilson, Anselm, Annammal Lenin, Nagaraj Periyasamy, and Lincy George. 2016. “Influence of Interlayer Thickness (Zn) on the Properties of Al 7020 FSW Joints.” 19(4):817–23.

Xie, Yuming, Xiangchen Meng, Feifan Wang, Yimeng Jiang, Xiaotian Ma, Long Wan, and

Yongxian Huang. 2021a. “Insight on Corrosion Behavior of Friction Stir Welded AA2219/AA2195 Joints in Astronautical Engineering.” *Corrosion Science* 192(February).

Xie, Yuming, Xiangchen Meng, Feifan Wang, Yimeng Jiang, Xiaotian Ma, Long Wan, and Yongxian Huang. 2021b. “Insight on Corrosion Behavior of Friction Stir Welded AA2219/AA2195 Joints in Astronautical Engineering.” *Corrosion Science* 192(August).

Xu, Wei-feng, Jun Ma, Miao Wang, Hong-jian Lu, and Yu-xuan Luo. 2020a. “Effect of Cooling Conditions on Corrosion Resistance of Friction Stir Welded 2219-T62 Aluminum Alloy Thick Plate Joint.” 30:1491–99.

Xu, Wei-feng, Jun Ma, Miao Wang, Hong-jian Lu, and Yu-xuan Luo. 2020b. “Effect of Cooling Conditions on Corrosion Resistance of Friction Stir Welded 2219-T62 Aluminum Alloy Thick Plate Joint.” *Transactions of Nonferrous Metals Society of China* 30(6):1491–99.

Xue, P., D. R. Ni, D. Wang, B. L. Xiao, and Z. Y. Ma. 2011. “Effect of Friction Stir Welding Parameters on the Microstructure and Mechanical Properties of the Dissimilar Al – Cu Joints.” 528:4683–89.

Yang, Min, Rui-jun Bao, Xiu-zhong Liu, and Chao-qun Song. 2019. “Thermo-Mechanical Interaction between Aluminum Alloy and Tools with Different Profiles during Friction Stir Welding.” 29.

Yu, Pengfei, Chuan Song Wu, and Lei Shi. 2021. “Analysis and Characterization of Dynamic Recrystallization and Grain Structure Evolution in Friction Stir Welding of Aluminum Plates.” *Acta Materialia* 207.

Yu, Pengfei, Chuansong Wu, and Lei Shi. 2021. “Acta Materialia Analysis and Characterization of Dynamic Recrystallization and Grain Structure Evolution in Friction Stir Welding of Aluminum Plates.” 207.

Zhang, Chenghang, Yu Cao, Guangjie Huang, Qinghui Zeng, and Yulong Zhu. 2020. “In Fl Uence of Tool Rotational Speed on Local Microstructure , Mechanical and Corrosion Behavior of Dissimilar AA2024 / 7075 Joints Fabricated by Friction Stir Welding.” 49(December 2019):214–26.

Zhang, H. J., H. J. Liu, and L. Yu. 2012. “Effect of Water Cooling on the Performances of

Friction Stir Welding Heat-Affected Zone.” 21(July):1182–87.

Zhang, J., R. J. Perez, and E. J. Lavernia. 1993. “Documentation of Damping Capacity of Metallic, Ceramic and Metal-Matrix Composite Materials.” *Journal of Materials Science* 28(9):2395–2404.

Zhang, Jingqing, Yifu Shen, Xin Yao, Haisheng Xu, and Bo Li. 2014a. “Investigation on Dissimilar Underwater Friction Stir Lap Welding of 6061-T6 Aluminum Alloy to Pure Copper.” 64:74–80.

Zhang, Jingqing, Yifu Shen, Xin Yao, Haisheng Xu, and Bo Li. 2014b. “Investigation on Dissimilar Underwater Friction Stir Lap Welding of 6061-T6 Aluminum Alloy to Pure Copper.” 64:74–80.

Zhang, Lan, Huilong Zhong, Shengci Li, Hongjin Zhao, Jiqiang Chen, and Liang Qi. 2020. “Microstructure , Mechanical Properties and Fatigue Crack Growth Behavior of Friction Stir Welded Joint of 6061-T6 Aluminum Alloy.” 135(October 2019).

Zhao, Y., S. Lin, F. Qu, L. Wu, Y. Zhao, S. Lin, F. Qu, and L. Wu. 2013. “Influence of Pin Geometry on Material Flow in Friction Stir Welding Process Influence of Pin Geometry on Material Flow in Friction Stir Welding Process.” 0836.

Zhou, L., G. H. Li, R. X. Zhang, W. L. Zhou, W. X. He, Y. X. Huang, and X. G. Song. 2019. “Microstructure Evolution and Mechanical Properties of Friction Stir Spot Welded Dissimilar Aluminum-Copper Joint.” 775:372–82.

Zohoor, Mehdi, M. K. Besharati Givi, and P. Salami. 2012. “Effect of Processing Parameters on Fabrication of Al – Mg / Cu Composites via Friction Stir Processing.” 39:358–65.

Publications

1. **Korra Nagu** and Adepu Kumar, Effect of tool rotational speed on microstructure and mechanical properties of friction stir welded AA6061-T6 alloy using brass interlayer. *Materials Today, Proceedings.* 33 (2020) 5486–5491- ***(Scopus)*** **Published**. https://doi.org/10.1016/j.matpr.2020.03.308
2. **Korra Nagu** and Adepu Kumar, Effect of brass interlayer on microstructure, mechanical and corrosion behaviour of friction stir welded AA6061-T6 alloy. *Part C: Journal of Mechanical Engineering Science* (2021*)* ***(SCI)*****- Published.** https://doi.org/10.1177/09544062211061480
3. **Korra Nagu** and Adepu Kumar, Influence of brass interlayer and water cooling on microstructure, mechanical and corrosion behaviour of friction stir welded AA6061-T6 alloy. *Part L: Journal of Materials: Design and Applications* (2022**) *(SCI)*- Published**. https://doi.org/10.1177/14644207221095137
4. **Korra Nagu**, Adepu Kumar, MVNV Satyanarayana, Kethavath Kranthi Kumar, V Uday Kumar, Damping behaviour of submerged friction stir welded AA6061-T6 alloy with addition of brass interlayer, *Materials Letters* (2022) ***(SCI)*****- Published.** https://doi.org/10.1016/j.matlet.2022.132695
5. **Korra Nagu**, K. Hari krishna and Adepu Kumar, Influence of interlayer material on softening and wear behaviour of friction stir welded AA6061-T6 alloy, *Transactions of the Indian Institute of Metals* ***(SCI)*****- Under Review**.